Engineering of Integrated Devices on Electro-Optical Chip: Grating Couplers, Algorithms, and Switches

by

Stevan Lj. Urošević

M.Eng. Electrical and Computer Engineering,
University of Novi Sad, Faculty of Technical Sciences, 2009
B.Eng. Electrical Engineering for Telecommunications,
Information and Communication Technologies College in Belgrade, 2007

Submitted to the Department of Electrical Engineering and Computer Science
in partial fulfillment of the requirements for the degree of

Doctor of Philosophy

at the

MASSACHUSETTS INSTITUTE OF TECHNOLOGY

February 2015

Signature of Author_____
Department of Electrical Engineering and Computer Science
November 4, 2014

Certified by_____
Peter L. Hagelstein
Associate Professor of Electrical Engineering
Thesis Supervisor

Accepted by_____
Leslie A. Kolodziejski
Professor of Electrical Engineering
Chair, Department Committee on Graduate Students

Engineering of Integrated Devices on Electro-Optical Chip: Grating Couplers, Algorithms, and Switches

by

Stevan Lj. Urošević

Submitted to the Department of Electrical Engineering and Computer Science on November 4, 2014 in Partial Fulfillment of the Requirements for the Degree of Doctor of Philosophy in Electrical Engineering and Computer Science

ABSTRACT

The technology of modern purely electrical computers requires more electrical wiring for intra-chip and inter-chip communications as the number of cores increases. Consequently, energy consumption increases due to heat dissipation from low bandwidth electric wires. The conversion of electrical signals to optical signals has been proposed in the future electro-optical computers as a way of addressing this issue. Much work has gone into the design, fabrication, and testing of components of new optical elements that can be implemented in chips fabricated in unmodified CMOS processes.

In this Ph.D. thesis advances are achieved through engineering of various integrated optical and electro-optical devices on the chip, algorithms for automatic engineering of integrated optical devices, and measurement methods that enable understanding of integrated device behavior. The highly unidirectional uniform optical grating couplers are simulated, and compared experimentally with typical uniform gratings on the same chip. Here, the method of comparison of devices in symmetrical structures is presented. An algorithm for the design of a grating that launches a beam with an arbitrary magnitude and flat phase front is described. As an extension of this, the second algorithm for the design of a grating that launches a beam (here, focusing) with an arbitrary magnitude and phase front is presented. An automatic algorithm which, from the 2D device contour file after optical proximity correction, builds up any 3D optical device further simulated in 3D-FDTD is described. The obtained device can be compared with the designed device before fabrication occurs. An electronically-controlled optical switch with free-carrier injection, which can switch digital optical signals from one waveguide into other, is described. This switch is many times smaller, faster and more energy efficient than a recent optical switch based on a traditional Mach-Zehnder interferometer. Next, three different measurement methods are presented and experimentally confirmed. The first method enables measurement of current through the heater in the complex diode topology on the chip. The second method is for measuring the desired temperature on the chip for tests of integrated devices. The third method is for automated measurement of angles of optical fibers for the coupling with the gratings.

Thesis Supervisor: Peter L. Hagelstein
Title: Associate Professor of Electrical Engineering

To my father,
Ljubiša Urošević,
in gratitude.

Acknowledgements and Work Origins

I (the author, Stevan Lj. Urošević) am the most thankful to my father, Ljubiša Urošević, to whom I dedicate this Ph.D. thesis. He brought me up, has taken care a lot about me, and taught me about being honest man and fair with people and environment. He was directing my thoughts on the importance of education and the importance of doing sport.

After my father, the most I am thankful to my grandmother, Radmila Urošević, to my grandfather, Stevan Urošević, and to my great-grandfather, Đurđe Urošević, for taking care a lot about me in many good ways and for many good advices while I was a kid before their death.

Besides my family, I am also the most thankful is my aunt, Nada. She was taking care a lot about me in many good ways while I was a kid, although she has two children who are older than me and husband.

In academia, the most I am thankful to my thesis supervisor (advisor), Professor Peter L. Hagelstein, for the following. He agreed to be my advisor, and he accepted my previous work to be included in the thesis. He provided many highly reasonable, intuitive and logical comments on significantly expanding the previous work from this thesis and also on making a new work that is a novel optical switch from Chapter 6 and Appendix A. He allowed for me to work on what I choose, and he clearly understands that this is the highest productivity for the student and the advisor. This is what I think as well. We both think the previous with understanding that the student is mature enough so can make good choices in the research and be an independent researcher. Also, I am very thankful to him for his commitments that I fairly complete the Ph.D., and for many useful discussions, advice and clarifications. I learned through his unique point of view and so his unique personality.

I am thankful to my previous Massachusetts Institute of Technology (MIT) advisor, Professor Vladimir Stojanović (while he was at MIT, currently he is a Professor at University of California, Berkeley), for giving me the Research Assistant position in his group. While he was at MIT and while I was in his group, I am also thankful to him about the following. He gave me the research problems to work on and discussed them with me, allowed me to use supercomputers for simulations and allowed me to use his lab. I did most of the work from Chapter 2 by using supercomputers and performing simulations, and also in his lab I performed measurements. Work from Chapter 2 is initiated at the University of Colorado Boulder (CU-Boulder) in the Professor Miloš Popović group; most of the work is done at MIT and it is completely written at MIT. At CU-Boulder with the advisor Professor Popović, I worked on the same project as the project in Stojanović group at MIT on which I worked on. At CU-Boulder I had worked before I came to MIT in Stojanović group. I did additional work from Chapter 2

while my advisor has been Professor Peter Hagelstein. Professor Stojanović allowed me that I do additional work for Chapter 3 and to write it in a form of the paper and that Professor Miloš Popović from CU-Boulder advise me about this while I was in Stojanović group. Focusing grating coupler from subsection 4.3.2 I completely designed at MIT by using the Direct Method from Chapter 4, which I realized at CU-Boulder in Professor Popović group, and I found and corrected the mistake in that method at MIT while I was in Stojanović group. Professor Stojanović gave me a task to realize the algorithm from Chapter 5, and I did realize it while I was in his group. I wrote about Chapter 5 while my advisor has been Professor Peter Hagelstein. Professor Stojanović said to me about the problem that an optical switch – electronically controlled needs to be designed instead of just using a switch based on a very large MZI (Mach-Zehnder Interferometer) and needs to be used for switching towards electronic memories. I discovered all three measurement methods from Appendix B and proved them experimentally in Stojanović lab. I partly wrote about section B.2 in Professor Stojanović group and partly while my advisor has been Professor Peter Hagelstein. Everything else from Appendix B, I wrote while my advisor has been Professor Peter Hagelstein.

I am thankful to my previous advisor Professor Miloš Popović for giving me a position on six months as a Research Scholar in his group at the CU-Boulder in the year 2010. There he gave me tasks to work on the optical grating couplers from Chapters 2, 3, and 4, which are from the same MIT project on which I continued to work at MIT in Professor Stojanović group while I was in Stojanović group; and partly I worked on these chapters while my advisor has been Professor Peter Hagelstein. While I was at CU-Boulder, Professor Popović and I had a Skype conference once per week with two MIT groups, Professor Stojanović group and Professor Rajeev Ram group about discussions on the project. I am thankful to Professor Popović for the following. He was showing me how to work in a two-dimensional finite-difference time-domain (2D-FDTD) numerical simulation method, mathematically and with drawings he explained to me optical concepts from the project. Professor Popović gave me his Matlab file for plotting pictures with various features of optical grating couplers after the 2D-FDTD simulation was completed, while I was a Research Scholar at CU-Boulder. Professor Popović mostly wrote this code, and I wrote some of it. For Chapter 6 and Appendix A, I deleted around 85% of this Matlab code because it is not needed for plotting the features of the switch designs, and I modified around 4% of remainder for plotting features of the switch designs. Professor Popović as my previous advisor contributed to the Chapters 2, 3, and 4 in the following way.

Chapter 2:

In the year 2010 Professor Popović gave me a task, while I was a Research Scholar at CU-Boulder, to design the unidirectional grating structure presented in Chapter 2; Professor Popović said to me that unidirectional gratings work based

on a relative shift of two core layers, body-Si (bottom core layer) and poly-Si (top core layer), with the constructive interference in one direction and destructive interference in other direction. Professor Popović had discussions with me about unidirectional gratings. I designed such unidirectional grating structure (besides other unidirectional gratings which I designed) which has 98% of unidirectivity, all within the constraints of the unmodified 45 nm SOI-CMOS foundry process in the year 2010 at CU-Boulder. In the same year 2010, my designs of unidirectional gratings were sent to fabrication in the mentioned foundry process. All measurements of fabricated gratings presented in Chapter 2 were performed in the first half of 2012 at MIT in Stojanović lab. The initial results for the work in Chapter 2 are obtained using computers from Popović group at CU-Boulder, and then at MIT I repeated these initial results which are in Chapter 2. Professor Popović defined mentioned four unidirectional grating parameters (I simplified his definition of parameters, which are in Chapter 2, while my advisor has been Professor Peter Hagelstein), without finding their numerical values. I wrote the code for design of these unidirectional gratings, and I designed them by finding numerical values of four unidirectional grating parameters. Professor Popović designed tapers. I discovered the new method of comparison of symmetrical structures, given in section 2.5.

Note that Professor Popović used draft of the most of Chapter 2, which was then in the form of the paper (which I wrote alone at MIT and sent to Professor Popović), as a part of the filed patent application CU3255B.

Chapter 3:

Professor Popović provided me detailed explanations, detailed corrections in writing and debugging the code, and I acknowledge many discussions while I was making the direct synthesis method from the Chapter 3. I developed this method in Professor Popović lab while I was a Research Scholar at the CU-Boulder in the year 2010, based on ideas of Professor Popović which Professor Popović asked to me to realize. Afterwards, I did more detail research of the work from the Chapter 3 at MIT in Stojanović lab and also I was writing that chapter in a form of the paper draft at MIT based on detailed explanations and detailed feedback of Professor Popović from CU-Boulder. Professor Popović made and gave me Figure 3.1(a,b), I converted this figure in the PNG format. I made Figures 3.2(a,b), 3.3(a,b) and 3.4, as Professor Popović said to me. Professor Popović processed Figure 3.4. All other figures are made and plotted after 2D-FDTD simulation is completed using a code that Professor Popović mostly wrote, and I wrote some of it. And, all these figures I made and processed in the current form as Professor Popović told me.

Note that Professor Popović used draft of Chapter 3 in the form of the paper, which I sent to him, as a part of the filed patent application CU3255B.

At MIT, I am very thankful to my advisor Professor Peter Hagelstein for discussions and his useful comments on the Chapter 3.

Chapter 4:

Professor Popović gave me a task to realize the direct method from the Chapter 4 while I was a Research Scholar at CU-Boulder in the year 2010. I realized that direct method in the year 2010 at CU-Boulder. Professor Popović explained me the operational principle of non-uniform focusing grating coupler and had many discussions with me. In section 4.2, I understood that the principle of direct method is the same as in the method from section 3.2; I also understood that to get an arbitrary phase front, the method from section 3.2 needed to be extended in the third dimension for the range of angles which form a desired arbitrary phase front (this is the parabolic phase front in the case of the focusing grating), and this is how I realized that direct method. In step 4, in the derivation of the Equation (4.12) for $\theta(x)$, Professor Popović pointed out some equations in the book "Waves and Fields in Optoelectronics" by H. A. Haus, and also wrote them on the paper by showing how I need to do the derivation, and from those equations I did the derivation of Equation (4.12). In that step 4, Professor Popović told me which interpolation function to use in the Matlab. The derivation in the Step 1 in section 4.2, Professor Popović did in discussion with me at the CU-Boulder in the year 2010. This derivation had the mistake. At MIT in Stojanović group in the year 2011 I found the mistake in the derivation and I corrected the derivation, and then double checked it in FDTD simulation, and it resulted in the correct work. The focusing gratings from subsection 4.3.1 I designed at CU-Boulder in Professor Popović group. I was writing the Chapter 4 in Professor Stojanović group at MIT. I made changes, clarified it and expanded it while my advisor has been Professor Peter Hagelstein at MIT.

I am thankful to everyone from EECS (Electrical Engineering and Computer Science) Department at MIT who influenced constructively that I receive the funding for the continuation of my Ph.D. after Professor Stojanović left the MIT.

I am thankful to the Dean for Graduate Education at MIT, Professor Christine Ortiz, and to the Senior Associate Dean for Graduate Education, Blanche Staton, for giving me the ODGE (Office of the Dean for Graduate Education) fellowships.

I am thankful to my graduate counselor from EECS at MIT, Professor Jeffrey Lang, for many discussions, and many highly reasonable and clear advices.

I am thankful to my Ph.D. Committee Members, Professor Cardinal Warde and Professor Mildred Dresselhaus for their commitments and advice, and also for the detailed comments on writing this thesis. I learned from both of them because they are both very experienced Professors, and each of them has his/her unique point of view.

TABLE OF CONTENTS

Chapter 1

_____

Introduction

_____

The technology of today's purely electrical computers requires more and more electrical wiring as the number of cores increases [see Figure 1.1]. In addition, Figure 1.1 shows many electrical wires as the consequence of many electrical wires on the chips, on the chip boards, and between the boards. This comes with increased energy consumption due to heat dissipation from low bandwidth intra-chip and inter-chip electric wires inside the computer, additional energy consumption for cooling, and unnecessary usage of the electrical wire itself in large quantities. This has provided motivation for considering an optical solution, in which the electronic digital signals are converted to optical digital signals that can take advantage of high-bandwidth optical fibers for communication between the different parts of a computer system. The lower power dissipation of the optical signals, both on chip and in fiber connectors, can increase the energy efficiency and make more efficient usage of resources.

Figure 1.1: Example of electrical wiring in the supercomputer at Goddard in the year 2014. From [http://geeked.gsfc.nasa.gov/?p=3601].

The technology of these future combined electrical and optical computers is approaching; it will be based on integrated electro-optics on a chip, fabricated in the standard (unmodified) CMOS fabrication processes [1-5], so that they can be made in the existing fabrication infrastructure. The technology uses photonic links for intra-chip and inter-chip communications, where electronic signals are imprinted (modulated) onto optical signals [2]. The number of electrical links is decreased, energy efficiency is increased, and the signal bandwidth is greatly increased. The global on-chip photonic link has an energy consumption of 0.25 pJ/b (where a bit is high intensity for binary "1" or low intensity for binary "0" at the wavelength λ_i of the i*th* channel) and bandwidth density of 160 – 320 Gb/s/μm [6]. In comparison, the global on-chip optimally repeated electrical link has energy consumption of 1 pJ/b and bandwidth density of 5 Gb/s/μm [6].

Consequently, these electro-optical computers will be more energy efficient and have larger bandwidth than purely electrical computers, so they can efficiently provide for the increased demands of multi-core computers [2].

The basic idea is that electrical signals are first converted into optical signals. Then they can be switched into an optical fiber for communication between chips, and then finally converted back to electrical signals. An example of this is illustrated in Figure 1.2, which depicts the basic components of photonic technology using a simple wavelength division multiplexing (WDM) link [2]. Light from an external (off-chip) two-wavelength continuous-wave (CW) laser source is carried by an optical fiber and arrives perpendicular to the surface of chip A, where a vertical coupler steers the light into an on-chip waveguide. This waveguide carries the light past a series of driver circuits [7] that imprint the electrical signal onto the optical carrier. Each driver circuit takes as input an electrical signal in terms of voltage, and uses a resonant ring modulator [5] tuned to a different wavelength to modulate the field amplitude (into binary "1" and "0") of the light passing by at that wavelength. The modulated optical signal continues through the waveguide, exits chip A through a vertical coupler into another fiber, and is then coupled into a waveguide on chip B. Then on chip B, each of the two receivers use a tuned resonant ring filter [5] to "drop" the corresponding wavelength from the waveguide into a local photodetector [8]. The light at the different wavelengths is sensed by photodetectors, which convert the

absorbed modulated light into modulated current in the different channels, which is further sensed by electrical receivers.
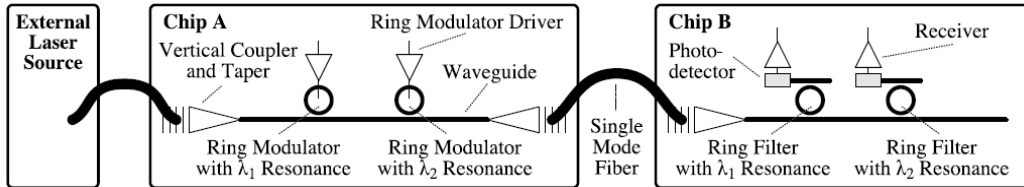
Figure 1.2: Photonic link with two point-to-point channels implemented with wavelength division multiplexing. From [2].

In order to make clear how this modulation works in the time domain, a set of the different electrical and optical signals is illustrated in Figure 1.3. The initial intensity at the carrier wavelength λ_1 from the external laser is approximately constant [see Figure 1.3(a)]; and the electronic digital signal is carried on the voltage input of the driver circuit of the ring resonator modulator which operates on λ_1 on chip A [see Figure 1.3(b)]. Following modulation, the optical intensity at λ_1 is modulated to carry the digital signal [see Figure 1.3(c)]. This modulated optical signal is communicated to chip B, where the signal at λ_1 is pulled out by ring resonator which operates on λ_1 (recall that many wavelengths are utilized in this wavelength multiplexing scheme) and converted to electrical current by the photodetector [shown in Figure 1.3(d)].

16
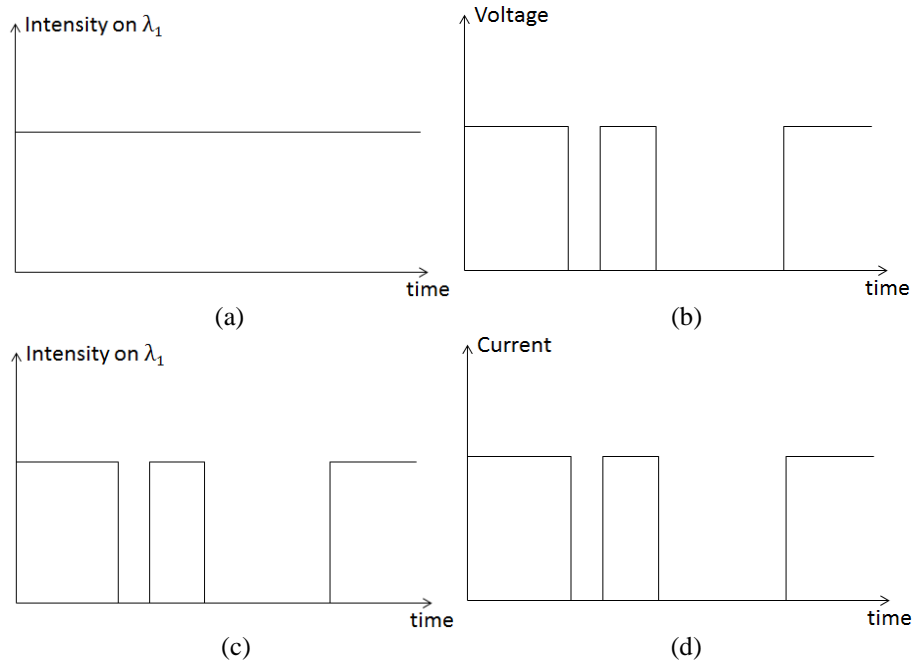
Figure 1.3: Illustration of the time domain signals from Figure 1.2 carried out on λ_1: (a) CW laser intensity of light on λ_1 vs. time; (b) voltage of driver circuit which controls a PIN diode for free-carrier injection in the ring resonator modulator which operates on λ_1, vs. time; (c) the voltage signal is imprinted on the intensity of light in channel 1 from (a), which means that light in this channel is modulated by intensity and consists of binary "ones" and "zeros"; (d) the modulated optical signal from (c) is converted by the photodetector into electrical current.

In this Ph.D. thesis, advances are achieved in various parts of the previously briefly described technology of the future electro-optical computers. These computers are currently in development. These advances are accomplished through the FDTD (finite-difference time-domain) simulations, algorithms, optical and electro-optical device designs, measurement methods and laboratory experiments.

17

Chapters 2, 3 and 4 are about advanced optical grating couplers for fiber-to-chip and chip-to-chip coupling. In Chapter 2 highly unidirectional uniform gratings, fabricated in the unmodified 45 nm SOI-CMOS foundry process, are presented. In addition, the unidirectional uniform grating is experimentally compared with the bidirectional (typical) uniform grating, fabricated in the same foundry process and on the same chip. Here, a method of comparison is presented that clearly demonstrates the efficiency of fabricated unidirectional grating relative to bidirectional when each is in a symmetrical structure with two the same kind of gratings. Then in Chapters 3 and 4 are discussed two methods for the design of the desired grating coupler. The first method from Chapter 3 is about the design of a grating which launches a beam with arbitrary magnitude (in the case of our demonstration, magnitude is Gaussian) and the flat phase front. The second method from Chapter 4 is the extension of the first method to the design of the grating that launches a beam with arbitrary magnitude and arbitrary phase front. Moreover, in the case of our demonstration, the magnitude is Gaussian, and the phase front is parabolic, so that the resulting beam is focusing.

Chapter 5 describes a fully automatic algorithm which extracts the device contour coordinates from the contour file for the arbitrary device geometry, after optical proximity correction (OPC). Then, the algorithm builds up any 3D optical device which is further simulated in 3D-FDTD, which can be compared with the

designed device before fabrication occurs. The device contour coordinates are the x and y coordinates for the points of the device contour on the chip.

Chapter 6 is devoted to designs of an electronically-controlled optical switch. In this Chapter 6 and Appendix A is shown that these switches have hundreds of times smaller area footprint, they are several times faster and several times more energy efficient, than switches based on traditionally used Mach-Zehnder interferometers.

At the end of each chapter and Appendix B, conclusions are provided. In Chapter 7, conclusions of the thesis are given.

Appendix B contains three different measurement methods related to devices that can be found on the electro-optical chip. The first method can enable measurement of current through the heater (resistor) in the complex diode circuits topology on the chip. The second method is for measuring the desired temperature on the chip for tests of devices on the same chip, which are exposed to temperature variations while electro-optical computer operates. The third method (algorithm) is for the automated measurement of angles of two optical fibers for the coupling with the two gratings, for the lab testing of devices on the chip. All these three measurement methods are experimentally confirmed.

Chapter 2

_____

Highly Unidirectional Uniform Optical Grating Couplers, Fabricated in Standard 45 nm SOI-CMOS Foundry Process

_____

In this chapter, and in Chapters 3 and 4, we consider the design of advanced optical grating couplers. A grating coupler is a periodic structure, which is the diffraction grating, and operates based on the splitting and diffracting the light into beams travelling in a certain direction [9]. The grating coupler is integrated on the electro-optical chip and consists of teeth (material of the waveguide – core) and gaps (material around the waveguide – cladding) [see Figure 2.1]. The purpose of the grating coupler is to bring the light on the chip from the external optical source (laser) through the input fiber (Figure 2.1). Or in other words, to couple the light from the input optical fiber into the waveguide on the chip. Also, to bring the light out of this chip to the second chip. Coupling the light to the second chip can be realized through the grating-to-fiber-to-grating coupling or grating-to-grating (chip-to-chip) coupling. In the latter case, the coupling is

realized through the focusing beam which the grating from the first chip radiates and the grating from the second chip receives (which constitutes a wireless connection between the two chips). On the second chip can be an integrated photodetector [8] that does an opto-electrical conversion, and afterwards, the electrical current is processed. More than two chips can be coupled.
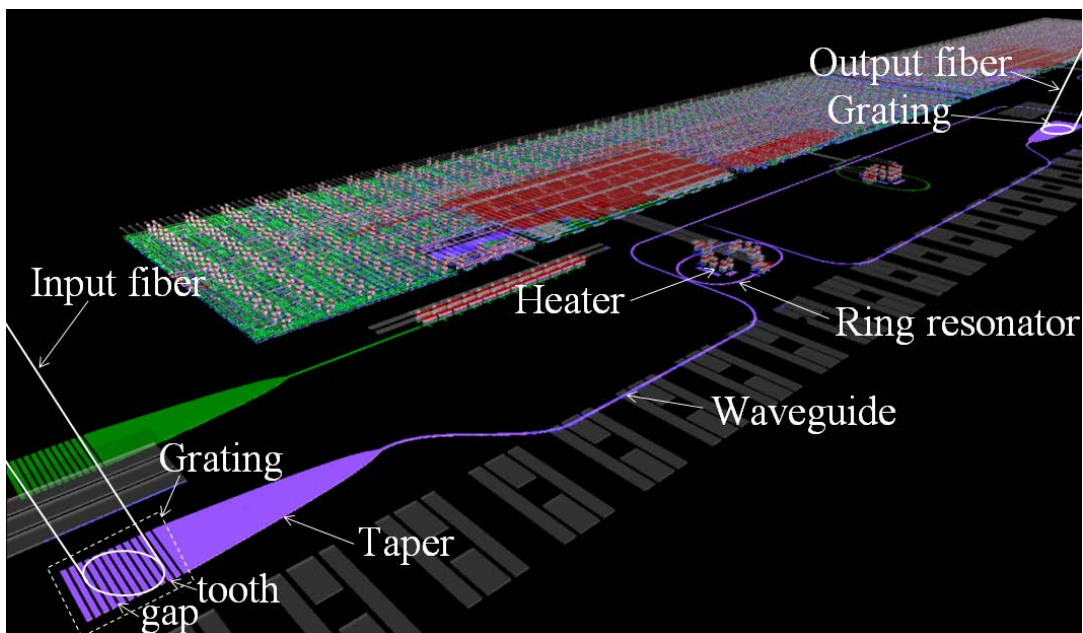
Figure 2.1: Optical grating couplers integrated on the electro-optical chip [Benjamin Moss made this figure, and author added fibers, arrows and words].

In Figure 2.1 is a ring resonator thermally controlled with a heater [10] which uses the light brought by the grating coupler in its operation. Consequently, the grating coupler, as a component through which the light is brought on the

chip, has fundamental importance for the energy efficiency on the chip(s), and also in total of future electro-optical computers.

For testing purposes of the gratings and other electro-optical devices on the chip, members of the Stojanović research group (while he was a Professor at MIT) usually used an external photodetector (optical power meter) connected with the other end of the output fiber [see Figure 2.1 for this fiber]. Also, there is the existing design of the integrated photodetector on the chip [8].

2.1 Introduction

In the development of future electro-optical computers [2] there is a need to bring the light in and out of their chips with the highest possible efficiency. The interface between devices outside the chip (for example, laser and photodetector) and on the chip (electro-optical devices) for coupling in both directions, is the optical grating coupler integrated on the chip.

One of the major problems of grating couplers (in terms of efficient chip-to-fiber and chip-to-chip coupling) is that they radiate power approximately equally in the up (P_{up}) and down (P_{down}) directions, above and below the grating, respectively, which are the bidirectional gratings [11-20] [see Figure 2.1 for illustration]; see Figure 2.2(a) only for directions of these two powers on the illustration of the unidirectional grating and not the bidirectional, because the illustration of these two powers would be the same in both kinds of the gratings.

Several theoretical approaches have been proposed previously for breaking this symmetry by designing unidirectional grating couplers based on antenna theory [21-24]. Reference [24] provides an experimental demonstration as well. With constructive interference in one direction unidirectional grating will radiate more power in that direction than with destructive interference in other direction. Also, unidirectional gratings [25, 26] as slanted gratings [27-35] and blazed gratings [36-44] are designed and some experimentally demonstrated. In all previous advances (none of which are within the constraints of the standard 45 nm SOI-CMOS foundry process [5]) the achieved unidirectivities are lower than those of the new structures which are discussed below. The term "unidirectivity" refers to larger power in percentage radiated in one direction (for example P_{up}, only if $P_{up} > P_{down}$ [for marked P_{up} and P_{down} see Figure 2.2(a)]), than in other direction.

(a)   (b)
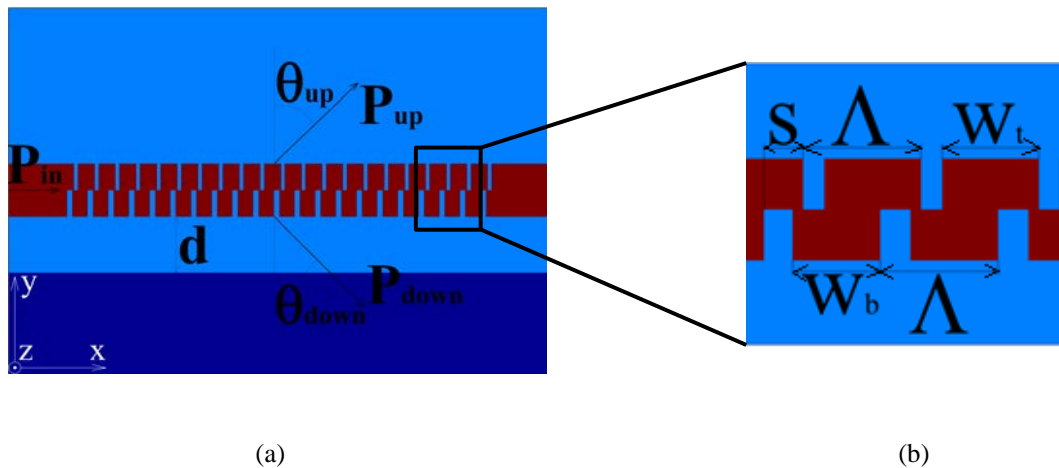
Figure 2.2: (a) Illustration of uniform unidirectional grating geometry under consideration; (b) unidirectional grating parameters.

The constructive interference mentioned above occurs in one direction because the diffracted (light) waves from two teeth has total phase difference zero, so there is adding of two waves in that direction. In addition, one tooth is in the bottom core and the other in the top core, with widths w_b and w_t, respectively [see Figure 2.2(a,b) for these two cores which are relatively shifted for s]. This total phase difference is the sum of the two phase differences, first in the horizontal direction (horizontal distance between two teeth) and second in the vertical direction (vertical distance between two teeth). The destructive interference in the other direction has total phase difference π, so there is cancelation of two waves in that direction. The operation principle is given in more detail in [21].

In this chapter our focus is on a new kind of grating coupler which makes use of an antisymmetric grating profile as illustrated in Figure 2.2(a) above. The basic idea is that a wave traveling along this coupler will see modulation from two different grating structures that can be designed and controlled independently, allowing for improved control of the field radiated out of the plane. The advantages of this approach are that it consistent with the constraints of the standard 45 nm SOI-CMOS foundry process [5]; and that by construction we minimize the number of degrees of freedom in the basic design, allowing for a convenient optimization.

2.2 General approach

To break the symmetry we designed gratings with two core layers by adjusting four parameters Λ, δ_b, δ_t, and s. Parameters δ_b and δ_t depend on w_b and w_t, respectively, and also on Λ. The parameters Λ, w_b, w_t, and s are indicated in Figure 2.2(b). The parameter Λ is the grating period of (both) the top and bottom core layer; $\delta_b = w_b / \Lambda$ is the fill factor of bottom teeth with widths w_b; $\delta_t = w_t / \Lambda$ is the fill factor of top teeth with widths w_t; and s is the shift of bottom core layer relative to the top core layer. The first three design parameters Λ, δ_b, δ_t are positive real nonzero numbers, and the last s can be either positive or negative. In Figure 2.2, s is negative (bottom core layer is shifted to the left relative to the top core layer).

In the design optimization, we manually adjusted the four parameters for each unidirectional grating design, while monitoring the FDTD [45] simulated gratings features, until high unidirectivities were obtained. In this, initial values of four unidirectional grating parameters are estimated by the following. Initial values for Λ is guessed based on typical values of grating periods for uniform gratings on central wavelength of 1550 nm, which are within constraints of CMOS, for example 800 nm. Initial values of fill factors δ_b and δ_t are guessed based on fill factor larger than 0.6, for example 0.7. The reason for this larger δ case (teeth widths w_b and w_t are larger and gaps are smaller in both cores) has a higher "effective" propagation constant of the guided light in the grating, which is

25

further from the radiation spectrum, and thus scattering to many radiation modes is less likely from perturbations [9]. Thus, interference of waves from bottom and top teeth is more efficient. For s initial value is chosen to be ±200 nm (we tried with both signs, first with - sign for unidirectional grating design with power radiation in up direction, and then with + sign for unidirectional grating design with power radiation in down direction). After we found final four values of parameters for each unidirectional grating design, these are presented in this chapter. These parameters also can be found using optimization algorithms, what we have not done in this chapter.

Since in this chapter there are already given final values of all four unidirectional grating parameters, further unidirectional grating design can be done with initial values equal to given final parameter values in this chapter.

Note that in this chapter the optical power P_{in} [see Figure 2.2(a)] at central wavelength λ=1550 nm (all gratings are designed for this wavelength) from the source propagates along the x axes in all simulations, using a two-dimensional finite-difference time-domain (2D FDTD) method [45]. In all simulations the given grating-to-fiber coupling efficiencies are relative to the total input power P_{in} in the grating from the source. Furthermore, by the reciprocity theorem [46], the fiber-to-grating coupling efficiency is the same in opposite direction as well.

In all FDTD simulations our measure of how good grating design is, is in terms of coupling efficiency with correspondent fiber mode field diameter (MFD)

and unidirectivity. In these simulations the mode overlap is used to obtain coupling efficiencies between the launched field from the grating $f_1(x)$ and Gaussian mode $f_2(x)$ of the fiber, in a range of x_1 and x_2, between which is the full width of each function $f(x)$. Equation (2.1)

$$O_{int} = \frac{\left|\int_{x_1}^{x_2} f_1(x)f_2(x)dx\right|^2}{\int_{x_1}^{x_2}|f_1(x)|^2 dx \ \int_{x_1}^{x_2}|f_2(x)|^2 dx} \qquad (2.1)$$

is used for the computation of the overlap. The correctness of this equation in a code is confirmed with overlap of two Gaussian functions which are "perfectly" aligned, which gave the result 100% (for complete overlap). Here, we need to keep in mind that this is done for steps along x axes of 10 nm; if the functions are not perfectly aligned there is error in range of this step. As we are computing overlap on the scale of μm along the x axis, this error is insignificant. Also, mode overlap with the input power P_{in} and each of the four following magnitudes is used to obtain: the optical power radiated in the up (total power radiated up) and down directions; and reflected (guided) power and transmitted (guided) power as well. This can be verified for each grating by summing all four mentioned magnitudes and for each grating result will be 1.

The MFD mentioned above for the single-mode fiber (Gaussian field or power distribution) is roughly its diameter; there is also the MFD of the Gaussian

beam which the grating radiates. If the beam does not have a Gaussian shape (for example, in the cases of the uniform grating), then the radiated field or the power spatial distribution is fitted with a Gaussian function. The MFD is the full width at $1/e$ of the maximum value of a field, for the field spatial distribution; where e is Euler's number. Otherwise, the MFD is the full width at $1/e^2$ of the maximum value of the optical power, for the power spatial distribution.

The goal of this chapter is to demonstrate through 2D-FDTD (2D is two-dimensional) simulations [45] and experiments, highly unidirectional uniform grating coupler designs that can be coupled efficiently with a standard single-mode fiber. In FDTD simulations, all designs are within constraints of the standard 45 nm SOI-CMOS foundry process [5]; and their features are simulated, where each design is aimed specifically at addressing a single problem that affects coupling efficiency in terms of unidirectivity. Long grating examples are explored first, and then short grating examples, with the corresponding values of MFD. The long gratings radiate optical power with the MFD few times larger than the MFD of power of single-mode fiber, while the short gratings radiate power with the MFD similar to the MFD of power of single-mode fiber. The fabricated final design was compared experimentally in terms of unidirectivity through the coupling efficiency with a bidirectional (typical) uniform grating coupler fabricated in the same process.

2.3 Simulation results of long unidirectional gratings

The purpose of presenting long unidirectional gratings (which are allowed within the SOI-CMOS foundry process constraints) is to show that almost all optical power P_{in} which comes in grating [see Figure 2.2(a)] can be successfully radiated in one direction; because in this case almost all optical power is radiated, then the reflected and transmitted guided powers are both close to 0%. These gratings should not be coupled (although they could) with a standard single-mode fiber due to their few times larger MFD than the fiber, which would result in significant power loss. But there are other advantages in terms of radiating almost all of the optical power in one direction, and possibilities to collect it. These advantages are in applications in which more optical power can be collected with an appropriate multimode fiber MFD than with single-mode fiber. In a multimode fiber the radiated optical power from grating will excite several modes, and all this optical power will not be guided through the fiber because of non-efficient overlap between grating radiated beam shape and different modes of fiber. In another case the surface of a phototedetector can be placed just above the unidirectional grating, then almost all of the optical power P_{in} which comes into the grating may be detected; by itself this may have applications.

We have designed a grating with unidirectivity in the up direction with parameter values: $\Lambda = 779$ nm, $\delta_b = 0.75$, $\delta_t = 0.83$, s = -266 nm, and with length along the x axes of 76.16 μm (the shortest length which gives $P_{up} = 96\%$) [see

Figure 2.2(a,b)]. Also, we have designed a grating with unidirectivity in the down direction with parameter values: Λ = 779 nm, δ_b = 0.86, δ_t = 0.65, s = +282 nm, and with length along the x axes of 47.55 μm (the shortest length which gives P_{down} = 98%).

Some FDTD simulation results for unidirectional gratings with up and down radiation directions are depicted in Figure 2.3.

The grating with up radiation direction has P_{up} = 96% radiated power in the up direction at λ=1550 nm [Figure 2.3(a)], P_{down} = 3% radiated power in the down direction, and the reflected and transmitted (guided) powers are both 0.5%. It has the most efficient coupling of 76.78% at λ=1550 nm with the fiber: the MFD = 38.73 μm and the radiation angle θ_{up} = 12.6° [see Figure 2.2(a)]. Figure 2.3(c) depicts the radiation pattern cross section in the x-y plane, in dB scale, and also here, the radiation angle θ_{up} = 12.6° for up radiation. In this Figure the field intensity is normalized with maximum of itself and represented on dB scale; therefore, we can see how maximum intensity level at 0 dB is radiated at angle of θ_{up} = 12.6° in up direction.

The grating with the down radiation direction has P_{down} = 98% radiated power in down direction at λ=1550 nm [Figure 2.3(b)], P_{up} = 2% radiated power in the up direction, and the reflected and transmitted (guided) powers are both 0%. It has the most efficient coupling of 83% with the fiber at λ = 1550 nm: the MFD = 21.37 μm and the radiation angle θ_{down} = 10.4° [see Figure 2.3(d)].
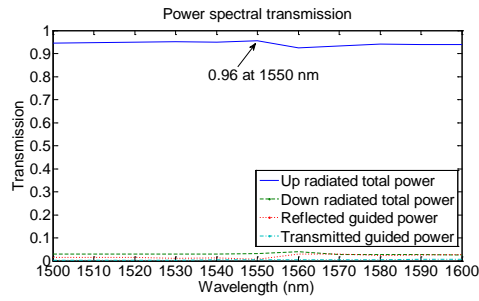
(a)
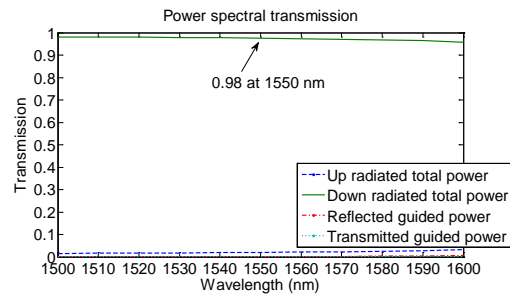
(b)
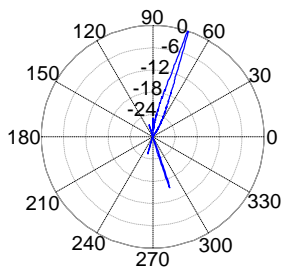
(c)
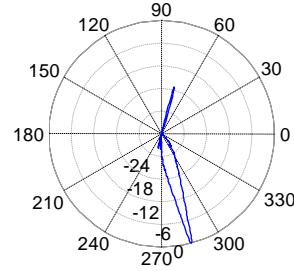
(d)
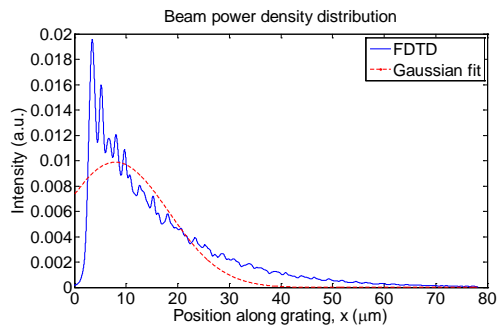
(e)
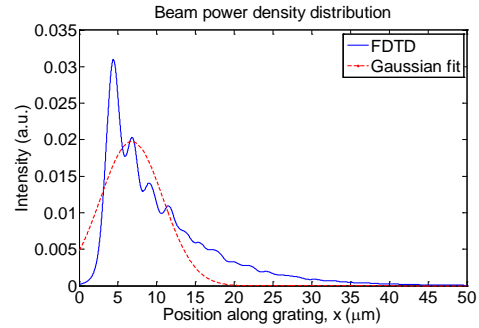
(f)

Figure 2.3: Some FDTD simulation results. Left hand side column (a, c, e) corresponds to the long unidirectional grating with up radiation direction and right hand side column (b, d, f) corresponds to the unidirectional grating with down radiation direction. (a,b) Power distribution. (c,d) Grating radiation polar plot in dB scale. (e,f) Intensity distribution along grating length.

Because of the long length of both gratings, with up and down radiation, the MFDs are too large for coupling with standard single-mode fibers.

In Figure 2.3(e) for grating with up radiation, a Gaussian fit (the fundamental mode of optical fiber) of intensity distribution along grating length shows that Gaussian reaches a very small value at x = 40 μm. For a chopped off grating with up radiation at x = 40 μm the up radiation decreases to a value of P_{up} = 89% at λ = 1550 nm, and for approximately the same amount of decrease of P_{up}, the transmission increases to a value of 7% (the down radiated power remained P_{down} = 3%, and the reflection is now 1%). Here, the decrease of the power P_{up} is approximately on account of increased power transmitted. For difference in lengths between two gratings of 38.2 μm, the difference in radiated power directivities of 7% is non-negligible. Also, in Figure 2.3(f) the Gaussian fit reaches a very small value at x = 20 μm. For chopped off grating with down radiation at this x = 20 μm the down radiation decreases to a value of P_{down} = 87% at λ = 1550 nm, again on account of the power transmitted which is increased to a value of 11%. Thus, in order to make highly unidirectional grating couplers close to 100% unidirectivity in the standard 45 nm SOI-CMOS foundry process in this chapter, we need to have long gratings to radiate all energy efficiently. But, there is also a tradeoff between grating length (in this case unidirectivity) and efficient coupling with single-mode fiber; because for a greater length, and therefore greater radiated beam MFD, the result is a smaller beam overlap with the power

distribution with the smaller MFD in single-mode fiber (a single-mode fiber has a smaller MFD than the grating beam MFD). Therefore, a smaller coupling efficiency results. Moreover, within the used foundry process constraints, gratings with down radiations are less sensitive to smaller grating lengths in terms of unidirectivity and therefore coupling efficiency with standard single-mode fiber.

2.4 Simulation results of short unidirectional gratings for coupling with standard single-mode fibers

In this section both gratings with up and down radiations are chopped off along the x axis at 16 μm, which make them short gratings. In chopping off these gratings, our goal was to find the best possible balance between high unidirectivity and high coupling efficiency with a standard single-mode fiber. This goal is achieved through grating with down radiation at the exactly this length, because if only one grating period shorter grating is chosen, this would decrease unidirectivity on account of increased (guided) transmission, as discussed in the previous section. Another grating length with up radiation is chosen to be the same length as grating with down radiation in order to be compared. Within used foundry process constraints, a chopped grating design was our only possibility to achieve our goal.

The short grating design with up radiation has P_{up} = 65.4% radiated power in up direction at λ = 1550 nm, P_{down} = 2.3% radiated power in down direction, and the reflected and transmitted guided powers are 1% and 31.3%, respectively. It has the most efficient coupling of 58% with the fiber at λ = 1550 nm: MFD = 16.1 μm and radiation angle θ_{up} = 12.6°. A large portion of the incident power in this case has gone into transmission. Because the up radiated power has drastically decreased, this grating is no longer highly unidirectional. However, if in this grating design we change the fill factors of both, bottom and top teeth, to new values of δ_b = 0.65 and δ_t = 0.72 (instead of the previously used δ_b = 0.75 and δ_t = 0.83, respectively), and keep the other two grating parameters and length intact, then P_{up} = 80% for this short grating then at λ = 1550 nm. This happens because smaller δ case (teeth widths w_t and w_b are smaller and gaps are bigger in both cores) has a lower "effective" propagation constant of the guided light in the grating, which is closer to the radiation spectrum, and thus scattering to many radiation modes is more likely from perturbations [9]. Therefore, power is radiated faster for the same short grating. Here, P_{down} = 8.7%, and the reflected and transmitted guided powers are 2.6% and 8.7%, respectively. In this case, as transmission is smaller it has greater unidirectivity. This grating has the most efficient coupling of 68.2% with the fiber at λ = 1550 nm: MFD = 14.29 μm and radiation angle θ_{up} = 7.3° (angle is changed because of change of grating parameter δ_b).

Some of the FDTD simulation results of short grating with down radiation are depicted in Figure 2.4. Figure 2.4(a) shows that $P_{down} = 86\%$ of the incident power is radiated in down direction; in up direction $P_{up} = 1.7\%$, and the reflected and transmitted (guided) powers are 0% and 12.3%, respectively. The radiated power in the down direction that is in the desired Gaussian beam mode of fiber is depicted in Figure 2.4(b). Here, radiation angle is $\theta_{down} = 10.4°$. Figure 2.4(c) gives the most efficient coupling with the fiber MFD = 15.1 μm and position x = 8.7 μm, for $\theta_{down} = 10.4°$ and $\lambda = 1550$ nm. For these values, maximum coupling efficiency is 78% [Figure 2.4(d)].

Because of the best possible features within the fabrication process constraints, the latest unidirectional grating with down radiation direction was fabricated in this standard 45 nm SOI-CMOS foundry process (reference [5] explains the used foundry process), and in next section an experimental demonstration is discussed. The radiation in down direction is not a problem, because the chip can be either coupled from down direction or turned upside down and then coupled from above.

The radiation angle θ depends from all four unidirectional grating parameters Λ, δ_b, δ_t, and s. Since these parameters are unchanged after chopping off the longer gratings, the short gratings have the same θ.

(a)

(b)

(c)

(d)
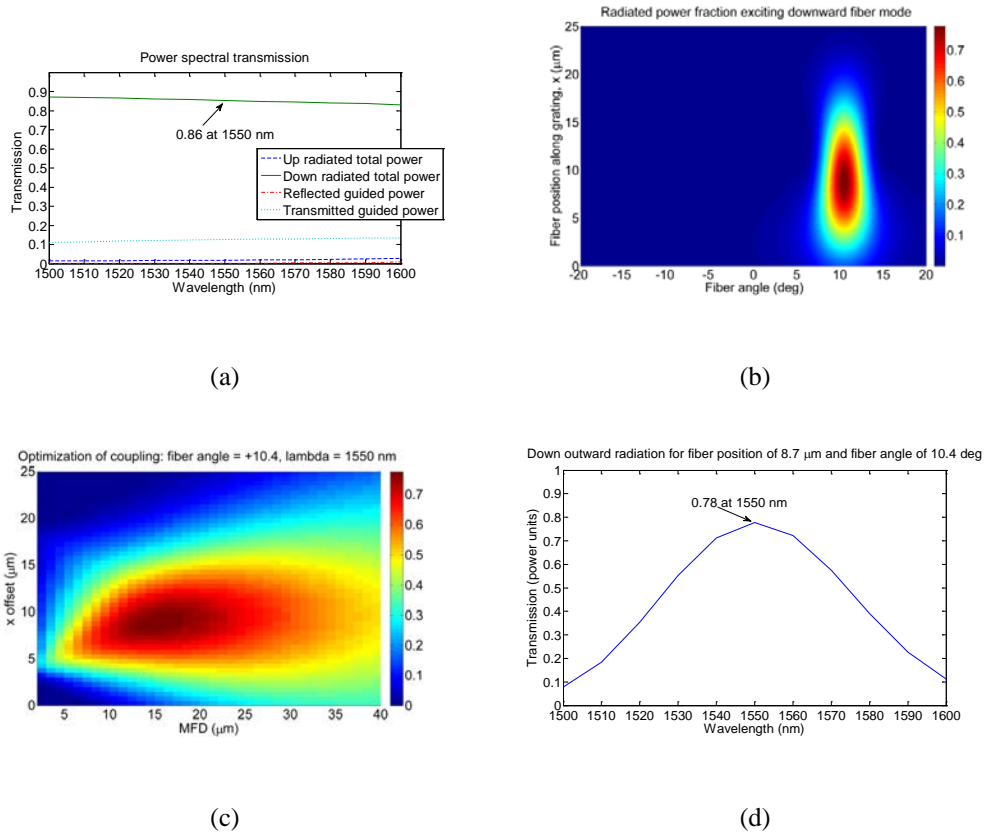
Figure 2.4: Some of FDTD simulation results of fabricated unidirectional grating with down direction of radiation and length of 16 μm. (a) Power distribution. (b) Input fiber power like third dimension (color scale) vs. fiber position and fiber (off-normal) angle. (c,d) Input-to-downward power fraction: (c) vs. collecting fiber position and MFD; (d) for optimum MFD = 15.1 μm, optimum fiber position of x = 8.7 μm and fiber (off-normal) angle of θ_{down} = 10.4˚ vs. wavelength (vertical axes is transmission into the fiber Gaussian mode).

Constraints of the standard 45 nm SOI-CMOS foundry process are more suitable in terms of unidirectivity for designing short unidirectional grating with down radiation than unidirectional short grating with up radiation. Here, the obstacle to design short gratings with up radiation with even higher unidirectivity

are resonances in buried oxide (BOX) layer with thickness d just below the grating bottom core [see Figure 2.2(a)], and at the same time, this gives advantage to grating with down radiation. To make even higher unidirectional short gratings, we have three following options in the foundry process which provide additional freedom relative to the process used in this chapter:

1) To adjust BOX thickness d (done elsewhere [20]);

2) To design stronger (greater power scattering per tooth) grating by using a foundry process with high index contrast between the grating two cores (teeth) and background (cladding) or/and using deeper (thicker) two core layers [20-22];

3) Combination of the first and second cases, which presents the best possible solution in terms of high unidirectivity.

In case 2) above, there is a disturbance (scattering) of the field at the boundary core-cladding, and again at the boundary cladding-core; so as the index contrast increases, this disturbance (scattering) will be greater as light propagates through the grating. Also, for a thicker grating core there is larger boundary surface which means that more field will be disturbed (scattered) on each boundary as light propagates through the grating. As a result, more power will be radiated, so that the transmitted (guided) power will be less. If in some cases reflected (guided) power appears, it can be shifted out of the desired wavelength range by increasing the angle of radiation.

All three cases above require finding new values of grating parameters for designing grating with even higher unidirectivity.

Using the explained uniform unidirectional grating geometry [Figure 2.2(a)] and its defined four parameters [Figure 2.2(b)], unidirectional grating can be designed in any appropriate foundry process with two core layers.

2.5 Experimental results

A fabricated unidirectional uniform grating [features in Figure 2.4] is compared with a typical bidirectional uniform grating with MFD = 10.47 μm and θ_{up} = 10.4˚ (also fabricated in the same standard 45 nm SOI-CMOS foundry process) in order to demonstrate which has better coupling efficiency with a standard single-mode fiber in terms of unidirectivity. Both types of gratings are fabricated on the same chip with other devices which are presented in reference [5] (which also explains foundry process that was used). The bidirectional grating has a FDTD simulated power radiation (in a direction towards fiber) of P_{up} = 38.14% and coupling efficiency of 30%.

Measurements are performed on two symmetrical test structures on the chip. The symmetrical structure is a grating-taper-waveguide-taper-grating [see Figure 2.5]. One symmetrical structure at both ends has unidirectional grating and another symmetrical structure at both ends has bidirectional grating. A diagram of the measurement setup is depicted in Figure 2.6. A laser with a single wavelength
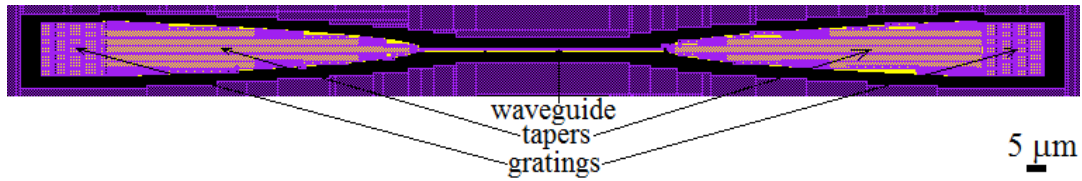
Figure 2.5: Symmetrical structure on the chip. Here, at both ends are unidirectional gratings.

$\lambda = 1550$ nm (both types of gratings are designed for exactly this wavelength) is connected with fiber polarization controller with three paddles (used to manually adjust the best possible coupling), which is connected with input optical fiber which is then vertically coupled (on correspondent (off-normal) angle θ) with input grating on one end of symmetrical structure. The grating on the other end is vertically coupled (at the corresponding (off-normal) angle θ) with the output fiber, which is connected to photodetector (optical power meter). The fibers used are standard single-mode fibers with MFD = 10.4 µm, and are positioned for coupling with the gratings using manual fiber positioners. The radiation angle θ is the same for both, unidirectional and bidirectional gratings, and also represents (off-normal) angle of the input and the output fibers used in the measurements. The input fiber has only a connector on one end, which is connected with three polarizers, while on the other end is lensed and coupled with the input grating of symmetrical structure. The output fiber is the same type as input fiber, so one lensed end is coupled with the output grating, and another end is input to a photodetector via connector. A visible microscope from the side is used to
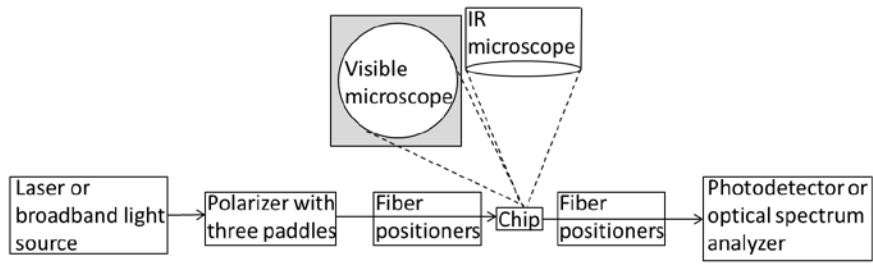
(a)
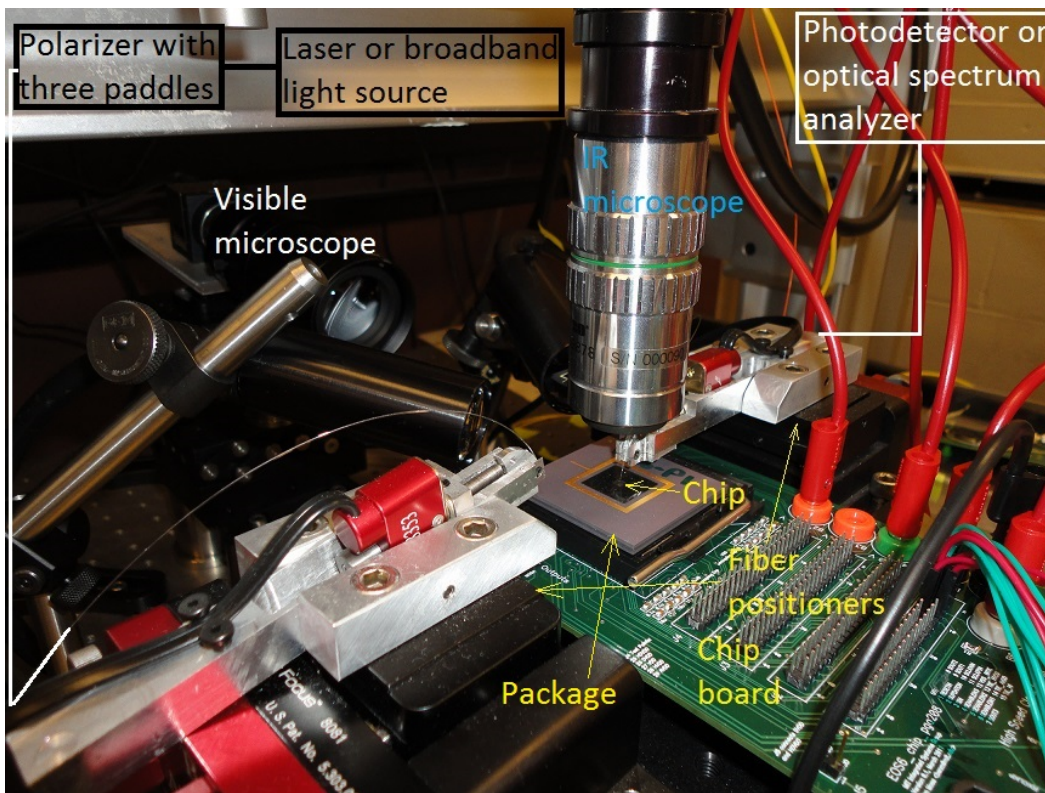
(b)

Figure 2.6: Measurement setup: (a) Diagram - solid lines with arrow present standard single-mode fibers with MFD = 10.4 μm, which are vertically coupled with gratings on the chip; (b) In the lab.

monitor the fibers so they do not touch the chip. And, an IR microscope above the chip is used to monitor the chip and the fibers from the top when the laser is ON (light from laser on 1550 nm can be seen with this microscope).

The equivalent in terms of connector attenuations (attenuation in used fiber lengths of 2 m is negligible) of input and output fibers in total, is one optical fiber of the same type with two the same type connectors on both ends. The measured attenuation of such a fiber with two the same type connectors on both ends is 0.38dB, which is taken into account below in the results of grating attenuation, instead of input and output fiber attenuation in total. For the fibers used the simulated coupling efficiency of the unidirectional grating is 73%, and for the bidirectional grating remains approximately the same (30%) as mentioned above. The measurement and setup is explained in more detail in [10].

The measurement results showed that total attenuation of the unidirectional grating and taper is 10.29dB, and for the bidirectional grating and taper is 14.68dB. This is for waveguide attenuation of less than 0.03dB and also for poly-Si loss of ~100dB/cm, which for this waveguide is ~0.65dB [5]. Only taper loss cannot be measured, therefore this is why the total attenuation of grating and taper are given, which are what people typically measure.

Another new method to present these measurement results is to use the concept of symmetrical structures. This method gives a more precise, simple and obvious to the reader comparison of unidirectional grating efficiency versus

bidirectional grating efficiency, without including taper attenuations. Equations (2.2) and (2.3) (the sequence of parameters is given in the direction of light propagation)

$$P_{in} f_f \, \eta_u \, f_t \, f_w \, f_t \, \eta_u \, f_f = P_{out,u} = 113 \ \mu W, \qquad (2.2)$$

$$P_{in} f_f \, \eta_b \, f_t \, f_w \, f_t \, \eta_b \, f_f = P_{out,b} = 15 \ \mu W, \qquad (2.3)$$

contain all parameters, which total influence is measured through photodetector as output optical power $P_{out,u}$ and $P_{out,b}$ for symmetrical structure with unidirectional gratings and for symmetrical structure with bidirectional gratings respectively, for the same input optical power $P_{in} = 19.2$ mW in the input fiber. In these equations f_f is a fraction of power from the previous power which is transmitted through the input fiber and approximately the same value for the output fiber; η_u and η_b are a coupling efficiencies of input and output unidirectional (subscript u) and bidirectional (subscript b) gratings, which are the fraction of power from the previous; f_t is a fraction of power from the previous, which is input and output taper transmission; and f_w is a fraction of power from the previous and it presents waveguide transmission. Because the taper-waveguide-taper transmission is approximately the same for both symmetrical structures, this gives fair

comparison of grating coupling efficiencies after equation (2.2) is divided by (2.3).

$$\left(\frac{\eta_u}{\eta_b}\right)^2 = \frac{P_{out,u}}{P_{out,b}} = 7.53. \qquad (2.4)$$

The measurement results show that detected optical power from symmetrical structure with unidirectional uniform gratings is ~7.53 times greater than the detected optical power from symmetrical structure with bidirectional uniform gratings. From Equation (2.4) the ratio of coupling efficiencies of single gratings is η_u / η_b = 2.74 and from FDTD simulation is η_u / η_b = 0.73/0.3 = 2.43, which shows that measured and simulated values are close for both types of gratings. Due to estimated fabrication error of ±10 nm around each grating tooth, the coupling efficiencies are slightly changed. This comparison method of measurement results is given with the intention that reader can see the improved efficiency of the unidirectional grating versus the bidirectional grating. This method can be used in other similar applications as well.

The designed MFD = 10.47 μm of the bidirectional grating is closer to MFD = 10.4 μm of the fiber than the MFD = 15.1 μm of the designed unidirectional grating. Therefore, if the measurements are performed with the fibers where the MFD is between two MFDs of unidirectional and bidirectional gratings, then the detected optical power ratio would be even greater, with the

condition that actual MFDs of gratings and fibers are close enough to the designed values. Although the measured unidirectional grating is designed with not exactly the same MFD as the single-mode fiber used in measurements (for reasons explained in the previous section); still, the MFD of the designed grating is seen to be highly efficient in coupling with the fiber used.

Figure 2.7 shows the normalized measured optical powers with the optical spectrum analyzer; the purpose of this figure is to check that these gratings are broadband in the wavelength range of the broadband light source used. For presentation of this measurement normalized optical powers are chosen due to the very large difference in values of broadband light source and both symmetrical structures, and also for a more obvious comparison of the three functions. A very large difference can be seen in the values of P_{in} from the laser and P_{out} from both symmetrical structures as mentioned above.

First, the measurement of the broadband light source with a central wavelength of 1550 nm is performed with optical spectrum analyzer. Then, measurements of two symmetrical structures (one with bidirectional and another with unidirectional gratings) are performed with the broadband light source and optical spectrum analyzer, instead of the setup with the laser and photodetector mentioned above. In Figure 2.7, we see that the normalized powers of both symmetrical structures, bidirectional and unidirectional, roughly follow the shape of broadband light source. This means that both types of gratings, bidirectional

and unidirectional, do not have significant attenuations in the wavelength band shown; therefore they are both broadband and can be used for the coupling of multiplexed (DWDM) light signals, in and out of the chip, in the experimentally demonstrated wavelength band.
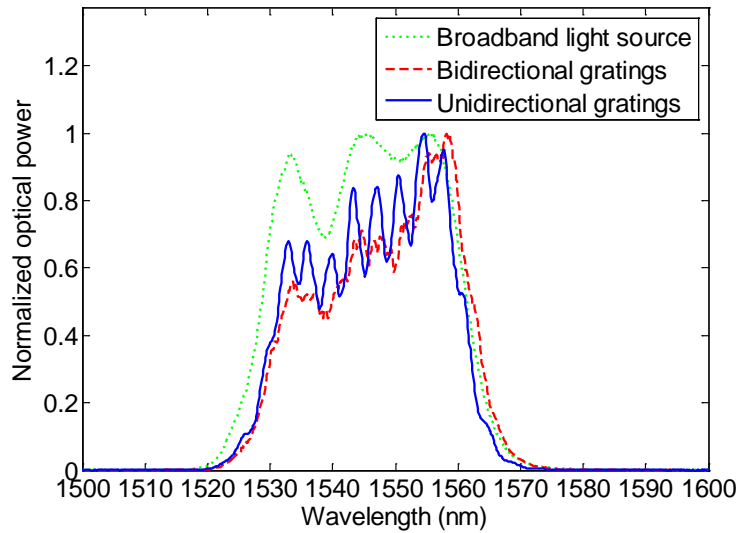
Figure 2.7: Normalized measured optical powers with optical spectrum analyzer of: broadband light source with central wavelength of 1550 nm as input light, output of symmetrical structure with two bidirectional gratings, and output of symmetrical structure with two unidirectional gratings.

2.6 Conclusions

New structures of highly directional unidirectional uniform gratings, all within the constraints of the standard 45 nm SOI-CMOS foundry process, are specified. In

addition, guidance is provided for further work on grating design. Suggestions are given as to how to obtain even higher unidirectivities of short unidirectional gratings in other foundry processes, which have additional freedom, relative to process used in this chapter.

The maximum achieved power unidirectivity is 98% for a unidirectional grating in simulation. A design with simulated power unidirectivity of 86% was fabricated for coupling with a standard single-mode fiber, and experimentally compared in terms of unidirectivity through a comparison with a uniform bidirectional grating fabricated in the same process. Measurements showed that the detected optical power from symmetrical structure with unidirectional uniform gratings is ~7.53 times greater than detected optical power from symmetrical structure with bidirectional uniform gratings. This was done using a new method of comparison based on the ratio of the efficiency of the fabricated unidirectional grating relative to the bidirectional grating. This method can be used for analogous symmetrical structures in other fields. Also, both types of gratings are broadband, which is proven with optical spectral analyzer; and they can be used for coupling of DWDM light signals, in and out of the chip.

As the grating unidirectivity is greater towards a fiber or a grating on another chip, there is higher probability of detecting greater optical power, which presents greater coupling efficiency. This new design can be incorporated with the non-uniform grating from the next chapter, which radiates a Gaussian beam for

the overlap with the fundamental Gaussian mode of optical fiber and as such can achieve coupling efficiencies close to 100%.

Chapter 3

_____

Direct synthesis of strong grating couplers for efficient integrated optical beam forming

_____

3.1 Introduction

In the last few years there has been interest in the problem of how to design highly energy efficient non-uniform gratings which synthesize a Gaussian beam without optimization, and which are also consistent with modern foundry processes. In earlier work [9,11-20,29,31,47-61] some papers describe only a theoretical approach for designing gratings which are not possible to fabricate with modern and existing fabrication processes, while other previously fabricated gratings have been designed with optimization. Moreover, proposed gratings which are consistent with modern foundry processes and which also generate a Gaussian beam, produce beams with theoretical mode overlap efficiencies (with the Gaussian shape of the fundamental mode of an optical fiber, or Gaussian beam

shape of a grating on another chip) no higher than 80%. As a general solution for this problem we propose a direct synthesis method.

In this chapter, we describe a method for the direct synthesis of non-uniform grating coupler designs which launch a beam with a Gaussian shape magnitude and flat phase front for efficient chip-to-fiber and chip-to-chip coupling over small distances (several microns). Due to its initial flat phase front a Gaussian beam [62] becomes wider at larger distances from the grating which disables coupling at these distances. The study has investigated different designs of gratings and with different MFDs (Mode Field Diameters), each aimed specifically at addressing a single problem that affects coupling efficiency in terms of mode overlap. (not obvious what this sentence is trying to say)

A grating that launches a beam with a certain magnitude and a certain phase front can also efficiently receive the same beam because of the reciprocity theorem [46].

In Section 3.2, we first describe in detail a direct synthesis method for a highly efficient non-uniform grating which launches beam with a Gaussian magnitude and flat phase front on a theoretical weak (small scattering power per tooth) grating example. Section 3.3 discusses an applied method to design a strong grating which is within constraints of standard 45 nm SOI-CMOS foundry process. Section 3.4 is devoted to discussion of our direct synthesis method and future improvements. In section 3.5 conclusions are given.

3.2 Outline of the direct synthesis method

In this section, we describe our direct synthesis method, and illustrate it step-by-step by applying it to a weak grating design first, designed to form a beam with 33.5 μm MFD. The geometry of a typical grating structure under consideration is illustrated in Figure 3.1.
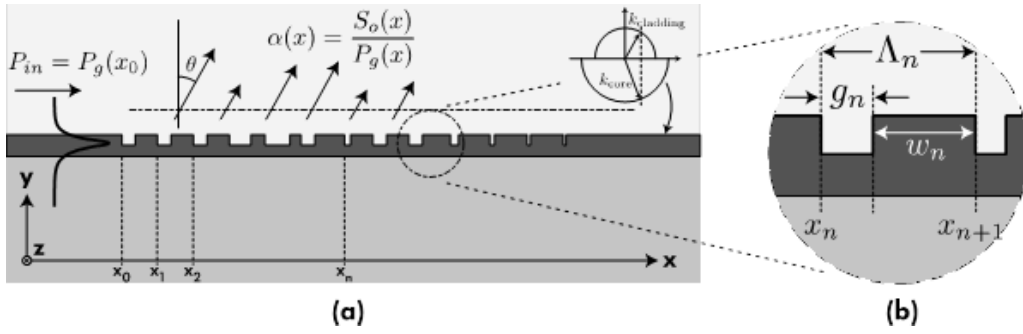
Figure 3.1: (a) Illustration of non-uniform grating geometry under consideration; (b) single, n-th gap/tooth element, with relevant parameters [Professor Miloš Popović from University of Colorado Boulder made this Figure, and the author converted it in PNG format that is more suitable for conversion to PDF format].

This and previous approaches [14,20] to synthesizing a grating to produce a desired output beam are based on engineering the profile of scattering strength of the structure along its length, which determines the radiated power along the structure (hence, the beam shape), and also the grating periodicity, which determines the direction of emitted radiation. This approach works well for low-index contrast weak gratings, where the modulation of the index does not perturb

significantly the waveguided incident field. In high index contrast gratings which can provide sufficient scattering strength to produce beams only a few microns in diameter, such as those used in silicon microphotonics, the effective propagation constant is modified from that in the unpatterned silicon slab. Furthermore, this perturbation depends on the tooth design, in terms of the fill factor, $\delta_n = w_n/\Lambda_n$ (Figure 3.1). Hence, the angle of emitted radiation depends not only on the period but also details of the tooth design. In particular, a grating with a constant period, but varied fill factor (duty cycle) along the length will have a radiation angle that varies with the position along the length. Another consequence of strong coupling in high contrast gratings is substantial reflection per tooth, where perturbative approaches to model the grating begin to fail.

To illustrate the method, which can produce a structure to form an arbitrary beam, we describe the design of a grating coupler that produces a Gaussian beam with the initial flat phase front, which has typically been the objective of previous work in silicon photonics [14-17,19,20,47-50,53]. We propose a direct synthesis method which takes as inputs the desired MFD and radiated beam angle, and produces the structure that launches this beam from a waveguide. The method comprises the following steps in general:

1) from the desired output beam field distribution, determine the grating strength (that is scattering strength) versus position [Figure 3.2(a)] [14,20];

2) from rigorous simulation, find the grating strength (radiation efficiency) and radiation output angle for a uniform grating versus the parameters of the grating, fill factor δ (and period Λ) [see Figure 3.1(b)];

3) numerically isolate the contour in Λ–δ parameter space which represents constant output radiation angle to obtain grating strength versus δ [Figure 3.2(b)] (and corresponding Λ [Figure 3.3(a)]) at constant output angle;

4) invert this data to map grating strength versus position to non-uniform δ(x) and Λ(x) vs. position (Figure 3.4); and,

5) apply a "discretization" strategy to approximately implement the continuous target δ(x) and Λ(x) distributions as a grating with a finite number of cascaded tooth elements.

This design strategy is completely deterministic, unlike the use of global optimization algorithms, always producing the same resulting structure for a given set of input parameters.

The remainder of the chapter will describe how we accomplish these steps, and will illustrate how well this can work through a few examples. In this chapter, we do not explicitly consider strong reflections per tooth in the synthesis (done elsewhere [20]), nor do we synthesize the grating exactly from the data, but instead use an approximate inversion. Nevertheless, the results show that an efficient design can be obtained by defining a continuous δ(x) and Λ(x) based on simulations, and then approximately constructing the discrete structure.

We illustrate the method first with an example structure targeted to launch a Gaussian beam with 33.5 μm MFD, at an output radiation angle of +8° (off-normal to avoid reflections from both sides [9,14]), and with a flat phase front. The purpose of targeting a Gaussian beam shape is to ensure good overlap with the fundamental mode of an optical fiber, thereby enabling high coupling efficiency. There are several components to achieving high coupling efficiency: maximizing mode matching of a beam to the target fiber mode, breaking top-bottom symmetry to ensure that all power is launched in only an upward or downward beam, and minimizing reflection. Our focus here will be mode matching. The other two components are addressed elsewhere [20,22,23,47,52,54].

The numerical simulation method used in the second step above is a 2D FDTD method [45]. Alternatively mode matching, harmonic propagation or other rigorous techniques may be used to obtain the same simulation results. 2D simulations are sufficient for the design of beams with an initial flat phase front with few microns or larger lateral extent, because the third (width) direction may be dealt with accurately by the effective index method, replacing the material refractive indices in the 2D simulation with values slightly corrected (lower) to account for the transverse extent of the guided mode.

The steps of the method in detail are:

STEP 1.   First determine the scattering strength distribution along the
grating to form a radiated Gaussian with *MFD=33.5μm*. The scattering strength
α(x) is defined as the radiated power density $S_o(x)$ [W/m] divided by the guided
power $P_g(x)$ [W]. We note that *α(x)* is also the decay rate of the power in the
waveguide, $S_o(x) = -\frac{d}{dx}P_g(x) = \alpha(x)P_g(x)$. It may be obtained directly from
the desired output beam power density $S_o(x)$ through the following [16,51]:

$$\alpha(x) = \frac{S_o(x)}{1-\int_0^x S_o(x\prime)dx\prime.} \tag{3.1}$$

where for a Gaussian beam, as in the present example,

$$S_o(x) = \frac{1}{\sqrt{2\pi(0.25\ MFD)^2}}\exp\left(-\frac{(x-m)^2}{2(0.25\ MFD)^2}\right). \tag{3.2}$$

where *x = 0* is the truncation point at the beginning of the grating, and *x = m* is
the center of the desired output beam intensity profile. For our example case, *α(x)*
is shown in Figure 3.2(a), where the center position of the Gaussian was placed at
m = 1.072 MFD = 35.9μm, so that at *x=0* the Gaussian has an intensity that is 1%
of maximum.

STEPS 2 and 3. To convert this $\alpha(x)$ distribution to a non-uniform grating design, we now find α vs. tooth fill factor δ [Figure 3.2(b)], by simulating uniform gratings. In general, a plot of α (and radiation angle) vs. fill factor δ (and period Λ) is needed. To avoid the need to simulate a complete two-dimensional parameter space, only to collapse it to a 1D contour in that space that represents the desired radiation angle, we instead put FDTD simulations through iterative method to converge on the correct uniform grating period Λ, for each value of fill factor δ. This can be done because this sub-problem is typically smooth and has a single solution. The starting guess for the period, Λ_0, is obtained from the propagation constant β of the waveguide mode entering the grating and the output radiation angle θ (θ_{target}) as

(a)   (b)
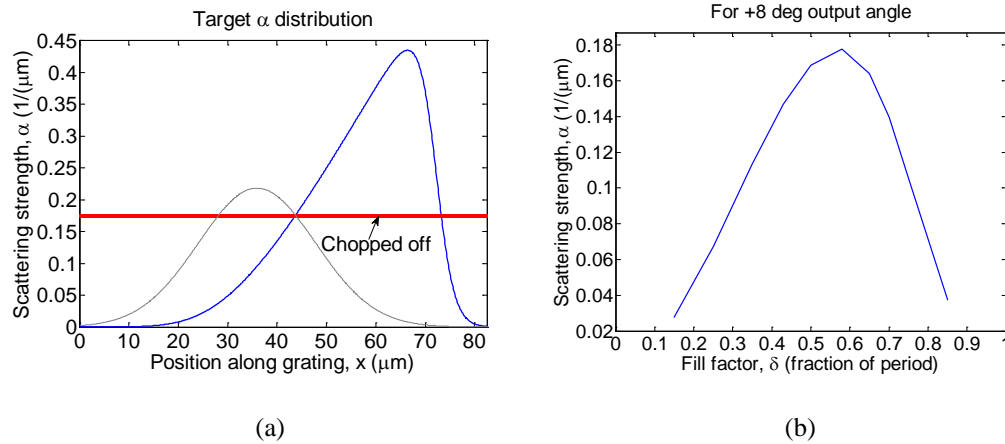
Figure 3.2: (a) Scattering strength $\alpha(x)$ vs. position x for Gaussian beam with $MFD=33.5\ \mu m$, center position $m = 35.9\ \mu m$, and output angle of $+8°$. (b) Scattering strength $\alpha(x)$ vs. fill factor δ.

$$k_{x,target} \equiv k_{cladding} \sin \theta = \beta + \frac{2\pi}{\Lambda_0} m \approx \beta + \frac{2\pi}{\Lambda} m. \qquad (3.3)$$

Where m is the chosen diffraction order (here, and usually, $m = -1$), and $k_{cladding}$ is the k-vector in the uniform cladding above the grating). The approximation here is in β, because the field within the strong grating structure is, in general, not well described by the propagation constant of the unpatterned exciting waveguide, and an exact equality will exist with some "effective" propagation constant in the grating. Based on the starting guess, at iteration n in FDTD simulation yields the actual angle $\theta_{actual}^{(n)}$ ($k_{x,actual}^{(n)} = k_{cladding} \sin \theta_{actual}^{(n)}$) and the period after iteration n is updated until convergence $\left| \theta_{actual}^{(n)} - \theta_{target} \right| < \theta_{tolerance}$ (in our examples, $\theta_{tolerance} = 0.1°$) using

$$\Lambda_n = \frac{2\pi}{\frac{2\pi}{\Lambda_{n-1}} + k_{x,actual}^{(n)} - k_{x,target}}. \qquad (3.4)$$

This simulation process produces simultaneously two design curves. First, it provides $\Lambda(\delta)$, that is period vs. fill factor, for a fixed output angle, shown in Figure 3.3(a). Second, the power decay rate α is obtained from the simulated radiation power density at a horizontal observation plane above the structure, since the uniform grating simulated (for one radiation angle θ, fill factor δ and period Λ) has a single exponential power decay along length, *exp(-α x)*. This is

true except when more than one grating order is excited efficiently; in this case, a more involved procedure is required to disembed α. Extracting the decay constant α in each simulated case by a linear fit of the log of the radiation power density produces Figure 3.2(b), giving scattering strength α vs. fill factor δ at the radiation angle θ of interest.
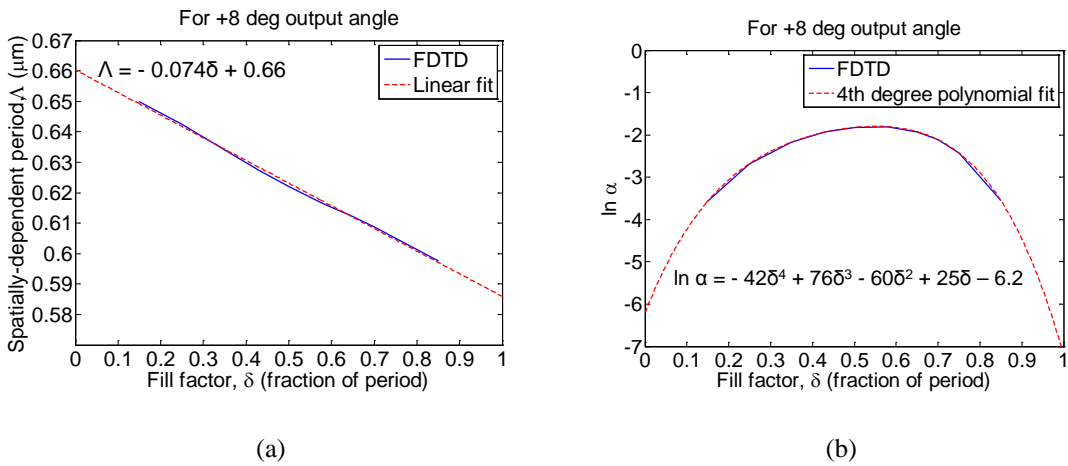
Figure 3.3: (a) To avoid chirp induced by varying the fill factor of a grating, the period Λ vs. fill factor δ is rigorously obtained from FDTD simulations for a fixed output angle (here, +8°). (b) ln α vs. δ and the best found fit of that function.

STEP 4. The next step is to synthesize the grating structure from the parametrized design curves. The first step here is to synthesize functions $\delta(x)$ and $\Lambda(x)$, which we define as continuous functions, from the desired $\alpha(x)$ [Figure 3.2(a)]. To do this, we need to invert the function in Figure 3.3(b). Before starting inversion there is one caveat – the "inverse" of Figure 3.3(b) is double valued that is there are two values of fill factor δ that give a particular α, one above and one

below the strongest scattering fill factor, $\delta_{max} \approx 0.6$. Thus, we must choose one branch of the function to invert, in this case either $\delta > \delta_{max}$ or $\delta < \delta_{max}$.

There is an important physical distinction between the two designs. The large δ case has small low-index gaps in a primarily silicon slab, while the small δ case has small silicon "ribs"/teeth in an unguided cladding. Thus, the latter case is a worse approximation of scattering power from a guided slab mode and will produce larger radiative losses [9]. Another way to understand this is that the small δ case has a lower "effective" propagation constant of the guided light in the grating, which is closer to the radiation spectrum, and thus scattering to many radiation modes is more likely from perturbations. We choose the large-δ case for this reason.

To allow simpler inversion of $\alpha(\delta)$, we fit a 4th-order polynomial to $ln\ \alpha$ vs. δ [see Figure 3.3(b)]. Then, Λ is computed by direct inversion, while δ is found by numerical inversion of the chosen branch of the fit. The obtained $\delta(x)$ and $\Lambda(x)$ functions for the 33.5 µm MFD beam launcher are shown in Figure 3.4.

The reader may observe a flat region in $\delta(x)$ and $\Lambda(x)$ in Figure 3.4. This occurs because the desired grating strength [see Figure 3.2(a)] for a Gaussian beam is too large, and the largest grating strength achievable with the example grating is not large enough [see Figure 3.2(b)]. Hence, the strength $\alpha(x)$ is "capped" at the maximum grating strength, leading to the plots in Figures 3.2(a)
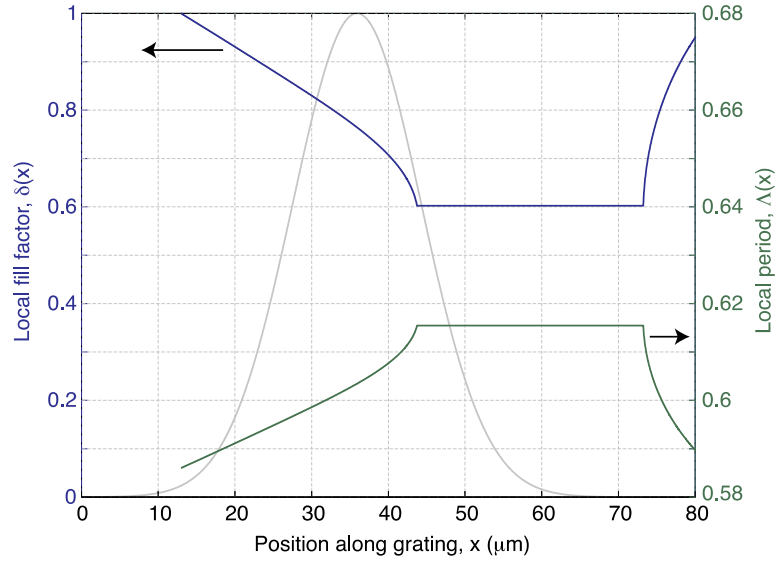
Figure 3.4: Chopped off functions δ(x) and Λ(x) with normalized desired Gaussian beam shape.

and 3.4. In the present case, this is not a concern because the majority of the Gaussian to be synthesized is within the realizable grating strength range, and the α(x) distribution is "capped" only toward the end tail of the Gaussian. However, this continuously rising required grating strength [Figure 3.2(a)] is typical for a Gaussian, which has rapid field fall-off as $exp(-x^2)$, whereas it will be flat (constant) for distributions with exponential tails that are more typical of waveguide and fiber modes. A wise choice of launch field may thus significantly impact realizability of a grating structure in terms of achievable dimensions, with implications for loss. This will be a future consideration.

STEP 5. The final step in the synthesis procedure is the translation of δ(x) and Λ(x) into a physical structure in step-index materials and compatible with

layered, lithography-based manufacture. Since we defined $\delta(x)$ and $\Lambda(x)$ as continuous functions of x, a discretization strategy is needed to produce a discrete grating structure that can be interpreted as producing the best approximation (or, rather, interpretation, because there is not an "exact" implementation) of these continuous functions. The following are two possible strategies:

1) Discrete sampling strategy: Choose a starting position x_0 (relative to the output beam); find $\delta_n = \delta(x_n)$, $\Lambda_n = \Lambda(x_n)$, $w_n = \delta_n \Lambda_n$, $g_n = \Lambda_n - w_n$, and $x_{n+1} = x_n + \Lambda_n$.

2) Integrated sampling strategy: Choose a starting position x_0. For each x_n, find a next position x_{n+1} so that the average of the period function $\Lambda(x)$ from x_n to x_{n+1} is equal to $x_{n+1}-x_n$ (which is the local period between x_n and x_{n+1}). For the fill factor, use the average of $\delta(x)$ between x_n and x_{n+1}.

For simplicity, we use the first strategy in the examples in this chapter. The resulting grating structure for the example being examined is shown in Figure 3.5. The grating is non-uniform because it radiates at a non-uniform rate along the grating to form the Gaussian beam shape. The non-uniform period compensates for chirp [18,63] in the design (that is unwanted) that would otherwise be introduced by the non-uniform fill factor at a constant period.
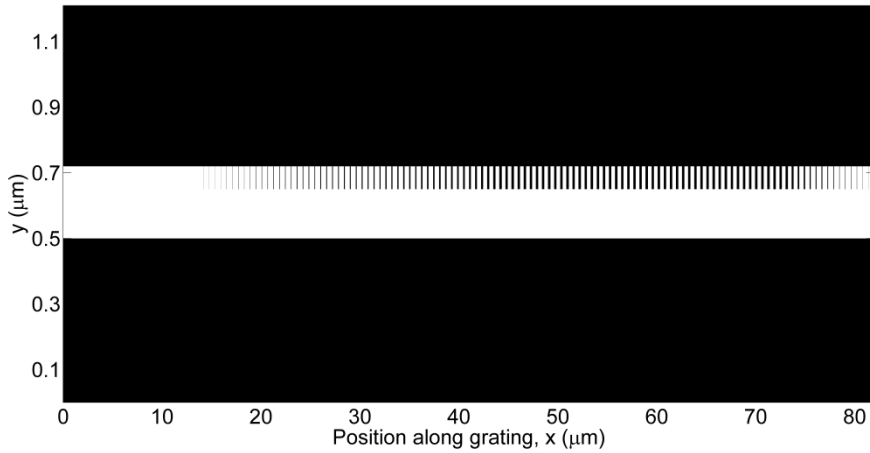
Figure 3.5: Non-uniform grating design launching Gaussian magnitude beam with a flat phase front.

3.2.1 Evaluation of design

The resulting structure, and the quality of the used algorithm, can be evaluated by a full FDTD simulation of the final, non-uniform structure, excited at the input waveguide port. The results are shown in Figures 3.6, 3.7 and 3.8.

Figure 3.6(a) shows power spectra that represent the total fraction of input power radiated up and down, reflected back into the input port, and transmitted through (that is past) the grating in the waveguide mode. Reflection and transmission are nearly zero as intended. The radiated power is split approximately equally between the up and down directions because the silicon grating in this example is buried in a uniform medium and largely symmetric with respect to the plane of the grating. Asymmetric structure designs have been

61

proposed including substrate reflectors [11,13,14,55] and unidirectionally-radiating tooth element design [22,23]. These can be directly incorporated into our approach, which addresses the complementary design issue – mode matching. We consider only the mode matching design in the present examples.

Figure 3.6(b) shows the k_x/k (the y-axis is *sin θ*) Fourier spectrum of the launched field distribution along the length of the grating vs. wavelength, showing that the launch angle depends on the wavelength as expected. Figure 3.6(d) shows a polar plot of the radiation pattern cross section in the x-y plane, in dB scale. Unlike parts (a, b, d), which show total radiated power, Figure 3.6(c) shows the radiated power in the up direction that is in the desired Gaussian beam mode. This is on the same order as the total power radiated upward, is a good indication that the beam is efficiently formed. The plot shows mode overlap efficiency with the Gaussian mode vs. position along the grating, and angle, indicating that the emission angle is as designed, +8°. Figure 3.6(d) also indicates that the radiation angle is as designed, +8°.

The efficiency of the synthesized grating at exciting the desired beam shape is obtained from the total power radiated up, and the up-radiated power specifically launched in the desired beam mode (overlap of radiated field with Gaussian mode). From Figures 3.7(b) and 3.6(a), the mode overlap efficiency is

$$\eta = \frac{P_{beam}}{P_{up}} = \frac{0.4756}{0.4828} = 0.9851 = 98.51\%, \qquad (3.5)$$

where P_{beam} is the power fraction coupled from the input port to the Gaussian beam (or approximately to an optical fiber mode with the same MFD), and P_{up} is the total fraction of input power that is radiated upward.

(a)   (b)

(c)   (d)
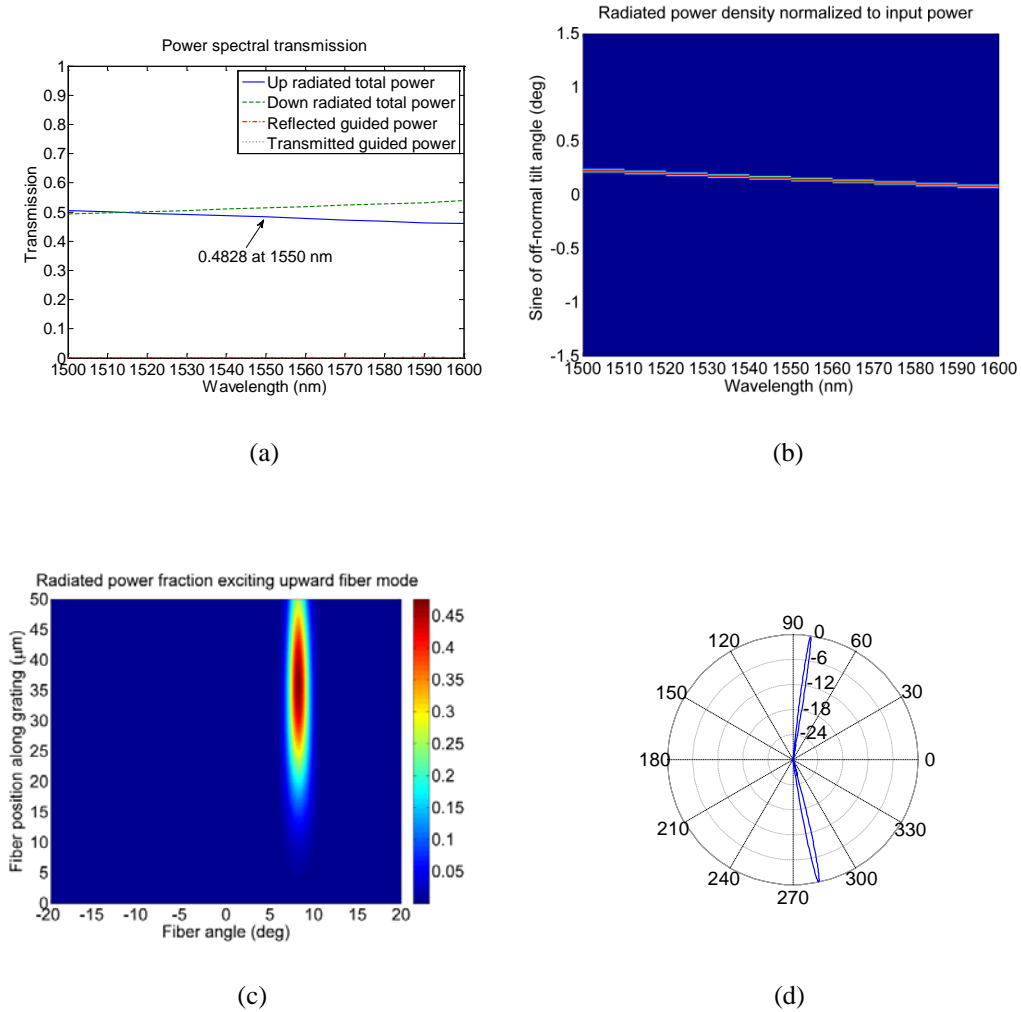
Figure 3.6: Some of resulting grating figures which present different features. (a) Power distribution. (b) sin(θ) vs. wavelength. (c) Input fiber power like third dimension (color scale) vs. fiber position and fiber angle. (d) Grating radiation polar plot in dB scale.
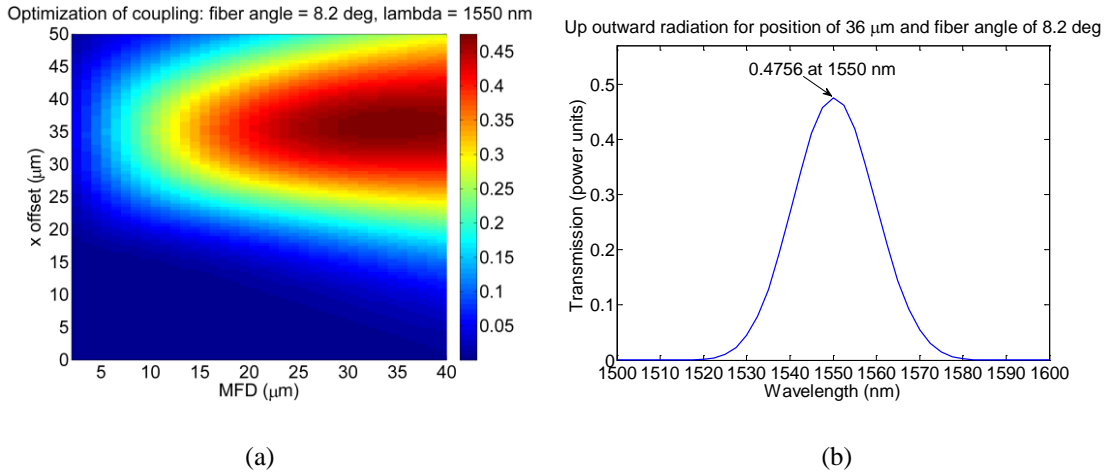
Figure 3.7: Input-to-upward Gaussian beam power fraction: (a) vs. collecting fiber position and MFD; (b) for optimum MFD and fiber position vs. wavelength.

The desired (target) and synthesized (FDTD simulated) radiated beam field profiles are shown in Figure 3.8, showing the near-unity mode overlap.
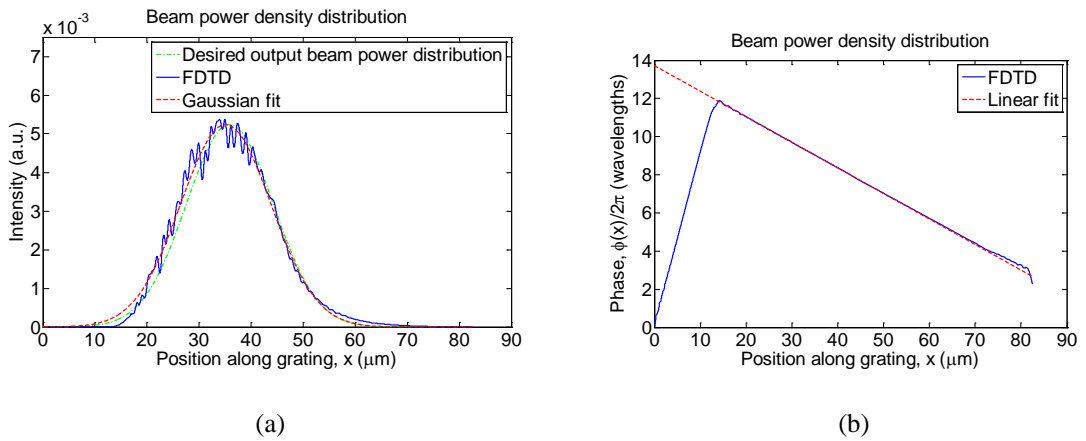
Figure 3.8: (a) Target Gaussian beam shape with MFD = 33.5 µm, simulated beam shape from FDTD with 98.51% mode overlap with the target Gaussian, and predicted Gaussian beam from continuous model synthesis. (b) Flat phase front of simulated beam shape from FDTD.

In part, the excellent mode overlap can be attributed to weak scattering per tooth in this grating that makes a single tooth scatterer a fairly small part of the entire structure, and this makes a continuum approximation a good one. Thus, the continuum approximation used here needs to be examined in such cases to determine its range of applicability. In shorter, stronger gratings needed to synthesize smaller-waist beams, there will be fewer, stronger scatterers (since the periodicity is roughly related to the guided wavelength and output angle, and not strongly dependent on the beam shape). Such designs are also of substantial practical relevance in silicon photonics as mode diameters in monomode optical fibers are about 10μm.

Note that the maximum scattering strength required [in Figure 3.2(a)] must be supported by the grating geometry for some choice of parameters [in Figure 3.2(b)]. A small mismatch in these may be tolerated, but a large mismatch will mean a substantial sacrifice of efficiency. Designing a non-uniform grating requires substantial variation in grating strength, and a 70 nm etch assumed in the present example is too shallow (maximum scattering strength too weak) to allow an efficient grating to be synthesized for small MFDs around 10 μm.

3.3 Application of synthesis method to strong and short gratings

In the second example, to permit sufficiently strong scattering strength for a small-MFD beam, we employ a geometry that is etched completely through the

grating core that is enables greater maximum scattering strength. In addition, we choose a layer geometry (grating core consists of two layers, poly-Si layer on top of body-Si layer) that is consistent with a standard 45 nm SOI-CMOS foundry process (reference [5] describes the used foundry process). The result of the same algorithm, for a 10.5 µm MFD, is a grating design with length of 19.5 µm along the x axis in this chapter [see Figure 3.1(a) for x axis]. In the foundry process used we could not change the BOX thickness, that is first layer bellow the grating (done elsewhere [20]), but the algorithm designed that grating containing this effect in scattering strength α.

Figure 3.9(a) shows the resulting Gaussian beam shape launched by this grating. The output angle here is larger, $\theta = +10^o$, because a stronger grating needs a larger angle to nearly eliminate reflection back to the input waveguide by second order diffraction [9,14,20]. The mode overlap efficiency is $\eta = 95\%$. The primary cause of the reduced efficiency relative to the first example is the "coarser" implementation of the smooth synthesized response due to a shorter (fewer periods long) grating. A second reason for the imperfect overlap is that the maximum scattering strength required by synthesis is a bit higher than that available in the structure below, and we deal with this situation by simply assigning the maximum available strength in the synthesis.
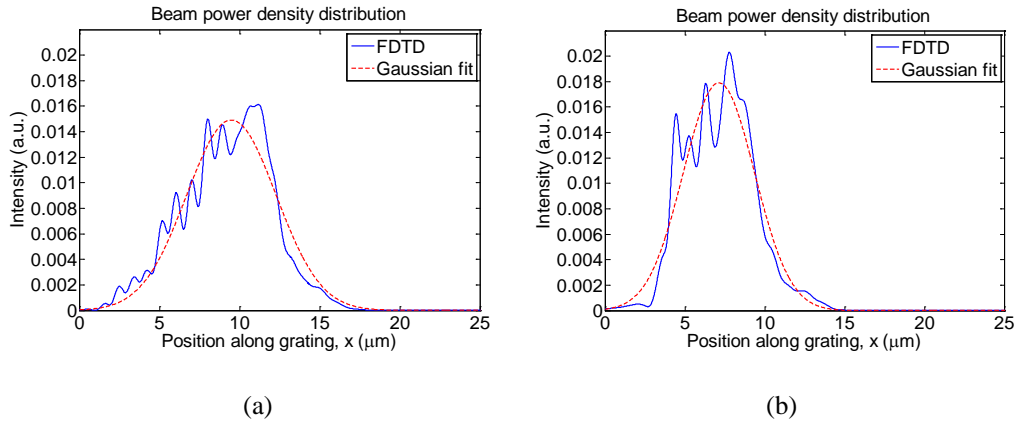
Figure 3.9: (a) Resulting Gaussian beam shape for MFD=10.5 µm. (b) Resulting Gaussian beam shape for MFD=7.8 µm.

A final matter of concern in the practical realization of synthesized structures is the lithographic minimum feature size (critical dimension). A grating synthesized from a continuum model will make use of scattering strengths approaching zero that is gaps or teeth approaching zero width. A realizable case may have minimum gap/tooth widths of the order of 100 nm. A number of strategies may be used to modify a synthesized structure to meet lithography constraints:

1) The grating periods with too small a feature are simply not implemented. In the large δ choice of design, this is acceptable because the contribution of these elements to radiation is typically small.

2) In regions where scattering is weak, join multiple periods into a single period, thus having a larger scatterer less frequently (every two or three

periods). This strategy enables a closer approximation of the idealized case.

Applying the first approach to the grating in the current example produces a grating design with length of 11.65 µm along the x axis, which is completely within the constraints of a standard 45 nm SOI-CMOS foundry process [5], and ready for fabrication. This grating design gives the beam depicted in Figure 3.9(b). The resulting radiation has an output angle of $\theta = 9^o$ and maximum mode overlap efficiency with a Gaussian beam at *MFD = 7.8µm* of *η = 91%.*

The direct truncation operation has changed the MFD, θ, and reflection at 1550 nm from near 0% to 5%. Accordingly it has lower overlap efficiency η. Nevertheless the overlap is efficient at over 90%. In principle, such small reflections can easily be compensated by inserting a single grating tooth with 5% reflectivity in front of the grating, [22,23] placed such that its phasing makes it an "anti-reflection coating" in the guided structure.

Our direct synthesis method can be used for designing gratings in any appropriate foundry process [5,10,64,65].

3.4 Discussion of the synthesis method and future improvements

The method of synthesis presented here primarily differs from previous techniques for synthesizing gratings in that it explicitly and rigorously accounts

for the necessary variation of period with grating strength (tooth fill factor), for a fixed angle of output radiation. This results in a non-uniform fill factor as well as period along the structure that are both direct results of the synthesis, and leads to high mode overlap efficiency.

It should be noted that, even with near ideal mode overlap efficiency, the total coupling efficiency in the presented examples is around 50% because the gratings are near symmetric and near half the power goes above and below the grating, respectively. Techniques have been proposed for providing unidirectional emission, including Bragg mirrors [11,13,14,55] and gratings based on symmetry breaking and antenna theory using unidirectional radiating elements [22,23]. The latter can be incorporated into the present algorithm to synthesize unidirectional designs, can be pursued in future work.

The proposed method can be used not only for arbitrary intensity distributions but also arbitrary phase front distributions, for example to launch focusing or defocusing rather than beams with initial flat phase front. This is accomplished in the next chapter. Non-uniform gratings which launch beams with Gaussian magnitude and flat phase front with MFD around 10 µm are adequate for exciting free-space beams, or for optical chip-to-fiber and chip-to-chip direct coupling over a small air gap of several microns. For point-to-point coupling over larger distances, diffraction will place a limit and require more complex beam shape synthesis.

There are a number of apparent paths for improvement of the presented synthesis method. First, synthesizing narrower-waist beams by using use shorter and stronger gratings leads to progressively worse synthesis accuracy and efficiency, as demonstrated. This has several causes. One of them is the presence of strong guided reflection for some fill factors (and thus resonance) in the grating, an effect that is currently disregarded by our algorithm. A second is the need for accurate estimation of the decay constant α in FDTD simulations in such situations. Both of these issues can be addressed by using a Bloch-mode based mode solver, similar to [20], instead of FDTD simulations to estimate decay constants and the degree of partial reflection. In addition, the algorithm needs to be modified to automatically synthesize from a model that includes reflections, but this problem can be overcome with choosing the appropriate radiation angle θ as an input in algorithm to avoid significant reflections, as we did in all presented grating examples.

In previous work, typically global optimization algorithms have been used to design grating couplers in silicon photonics [12,14,15,17,20,47,48,50,53,55]. While our algorithm can achieve efficiencies comparable to the best results using genetic algorithms, it could also serve as a good starting point for either local or global optimizers that can correct for higher order effects not accounted in the model used by our direct synthesis algorithm.

3.5 Conclusions

We presented a direct method for the synthesis of optical grating couplers that may launch arbitrary beam intensity patterns, and demonstrated the method with Gaussian beams for free-space and chip-fiber coupling applications. The method explicitly compensates unwanted chirp, that is intrinsic to non-uniform grating designs with a constant period, to directly synthesize gratings that efficiently excite a beam, without use of global optimization algorithms. Moreover, with this method full and repeatable control over automatically engineered, from inception to completion, desired beam intensity pattern, which grating radiates, can be achieved with completely rigorous mathematical understanding and so modeling of grating design, which is accomplished for the first time for the non-uniform grating designs. We showed that near ideal mode overlap efficiency, above 98.5%, can be obtained for Gaussian synthesized beams, but that this is somewhat reduced for stronger, shorter gratings. Using the method, we show that a design can be synthesized with a 7.8 µm MFD, compatible with a standard 45 nm SOI-CMOS foundry process with mode overlap efficiency over 90%. In this method can be incorporated unidirectional grating design in the same foundry process from chapter 2, and therefore, practically coupling efficiencies close to 100% with the fiber or grating on other chip on distances of few microns can be experimentally demonstrated for fabricated gratings.

Chapter 4

_____

Direct method for automatic engineering of optical grating couplers that launch beam with desired arbitrary magnitude and desired arbitrary phase front – Focusing gratings

_____

4.1 Introduction

In the development of the future electro-optical computers and their chips in the CMOS technology there is a 3D stacking of the chips and so communication among these is needed. One of the efficient solutions would be that these chips communicate via (wireless) light beams which are launched and received from focusing grating couplers. This can be done such that a grating on one chip radiates a focusing beam of light which after the focal point then defocuses, so it can be detected with the same kind of grating on the chip above (or below), at a

distance double than focal point distance from the grating on the chip below (or above).

In previous work on focusing grating couplers there are theories and many different designs using optimization, among which some are fabricated and experimentally demonstrated [66-95]. Unlike these, we are proposing a fully automatic and rigorous method for generation of optical grating couplers which launch a beam with a desired arbitrary magnitude and a desired arbitrary phase front.

The method presented in Section 3.2 is extended (in Section 4.2) in the third dimension for radiation output angles. This extension is performed on such a way that in FDTD simulation [45] there is one desired central constant output radiation angle θ_c and there is a correspondent range of constant output radiation angles around the mentioned central angle in order to form the desired arbitrary phase front. We demonstrate this method in the case of the automatic design of non-uniform focusing grating couplers for chip-to-chip and chip-to-fiber coupling at desired distances. Figure 3.1 illustrates the non-uniform grating coupler and its parameters under consideration in this chapter. Note that in Figure 3.1, instead of vertical axis y we use vertical axis z, and also instead of constant θ is changeable $\theta(x)$, for the discussion in this chapter. In Section 4.2 we describe the method, and we demonstrate it for a weak grating (which is long, with smaller scattering strength α) example with MFD = 33.5 μm. Then in Section 4.3 we demonstrate

the method on two strong gratings (short gratings, with higher scattering strength α) fully within constraints of the two different fabrication processes. The first strong grating is fully within the constraints of the existing unmodified 45 nm SOI-CMOS foundry process [5]. The second strong grating is fully within the constraints of the existing low-loss poly-Si core in an emulated high-volume electronics fabrication process [96]. Section 4.4 contains conclusions.

All these focusing gratings radiate beams with a Gaussian magnitude and the parabolic phase front, and therefore beam focuses at the desired distance from the grating (chip), and then subsequently defocuses. Also, all gratings in this chapter are designed for the central wavelength $\lambda_0 = 1550$ nm.

Note that in order to follow explanation of this method in the next section it is necessary to follow explanation of the previous method in the section 3.2.

4.2 Outline of direct method

The purpose of the non-uniform grating which launches a beam with a Gaussian magnitude and parabolic phase front is to have a focus at certain distance d. At the focus distance d such grating gives smaller MFD relative to the MFD along the grating (at zero distance from the grating). The focused Gaussian beam will have the same MFD at the distance L = 2d from the grating as it has along the grating (at the zero distance). Therefore, this kind of grating can couple chip-to-chip or chip-to-fiber at a chosen distance L, or at a focus distance d, or somewhere within

distance L, so that the MFDs of the two gratings (chip-to-chip) or grating and fiber (chip-to-fiber) must be consistent.

The method described in Section 3.2 which automatically determines a grating which launches a beam with a desired magnitude and flat phase front, is extended to a new degree of freedom $\theta(x)$ which is the grating radiation angle vs. position x along the grating, for the formation of the desired phase front. This angle $\theta(x)$ was assumed constant in Section 3.2 [see Figure 3.1], which is why the phase front is flat there (in this chapter, $\theta(x)$ changes along the grating length). In addition, the angle $\theta(x)$ is tilted by the central radiation angle θ_c [see Figure 4.1]. The extended method for automatic generation of a high energy efficient (high overlap with desired beam shape – mode) non-uniform grating, which launches a beam with a desired magnitude and a desired phase front, is explained in this section on a weak grating example. This grating example launches the beam with the Gaussian magnitude (with MFD = 33.5 µm along the grating) and the parabolic phase front (so Gaussian beam can focus, and grating is then named as focusing grating coupler).

The five steps explained in Section 3.2 are modified by the following way:

1) in general, this step is unchanged. For focusing gratings, we make the addition before this step;

2) this step is performed for each angle in the corresponding range of angles to form the desired phase front;

3) again, this step is performed for each angle in the corresponding range of angles to form the desired phase front;

4) this step is the same in general, except that here we deal with a 3D function due to the additional arbitrary phase front instead of a 2D function in the case of flat phase front (constant radiation angle);

5) this step is completely unchanged.
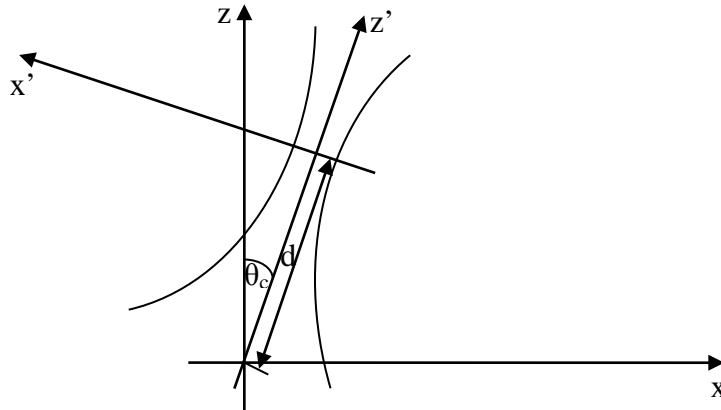
Figure 4.1: Coordinate (x, y) transformation for tilted focusing Gaussian beam in coordinate system (x', y') of the grating that radiates beam at central radiation angle θ_c.

Additions to the steps of the method from Section 3.2 are explained in detail in the example of a focusing weak grating which launches the beam with the Gaussian magnitude (with MFD = 33.5 µm along the grating) and parabolic phase front are:

Step 1 (for a focusing grating an addition is made before this step, which is described here): This step depends on our goal: for a grating for chip-to-chip

coupling with a desired MFD = 33.5 µm, in this case we are using L = b = 404.29

µm. The b is the confocal parameter of focusing Gaussian beam. The minimum

beam radius w_0, which is at a distance d = L/2 (a place of the beam focus – see

Figure 4.1) from the grating, is [62]:

$$w_0 = \sqrt{\frac{2b}{k}} = 11.73 \text{ µm,} \qquad (4.1)$$

We can calculate the beam radius at any distance z' from the grating:

$$w(z') = w_0\sqrt{1 + \left(\frac{z'}{b}\right)^2} = w(z' = L) = w_0\sqrt{2} = w_L = 16.59 \text{ µm.} \qquad (4.2)$$

Coordinates (x', z') are from transformed coordinate system (x, z) [see Figure

4.1]. We chose the central angle of the parabolic phase to be $\theta_c = 8^o$ (because of

~0 reflection) and this gives the following radius of the Gaussian beam and the

corresponding MFD at the other grating which is on the other chip or MFD of the

optical fiber:

$$w_{L \text{ tilted}} = \frac{w_d}{cos\theta} = 16.75 \text{ µm,} \qquad (4.3)$$

$$MFD = 2w_{d\ tilted} = 33.5\ \mu m. \qquad\qquad (4.4)$$

Steps 2 and 3: The principle here is the same as in the method from Section 3.2, but to compose an initial arbitrary phase front, the method from Section 3.2 needs to be extended in the third dimension for the range of angles which form a desired arbitrary phase front (this is the parabolic phase front in the case of the focusing grating).

Steps 2 and 3 are performed each with the angles in the range from 2° to 14° and with discretized step of 2°, such that the chosen central angle is $\theta_c = 8^o$. This range of the angles corresponds to the parabolic phase front which has $\theta_c = 8^o$. However, this method works with the 3D and not with the 2D functions, as was the case for the method from Section 3.2. But for every certain discrete position x_0 along the grating, $\theta(x_0)$ is fixed. Therefore, with this condition we have once again 2D functions for every fixed $\theta(x = x_0)$ along the grating.

Figure 4.2 shows the 3D function α vs. fill factor for discrete angles θ in a range from 2° to 14° with the step of 2°.

Figure 4.3 shows 3D function period vs. fill factor for discrete angles θ in a range from 2° to 14° with the step of 2°.
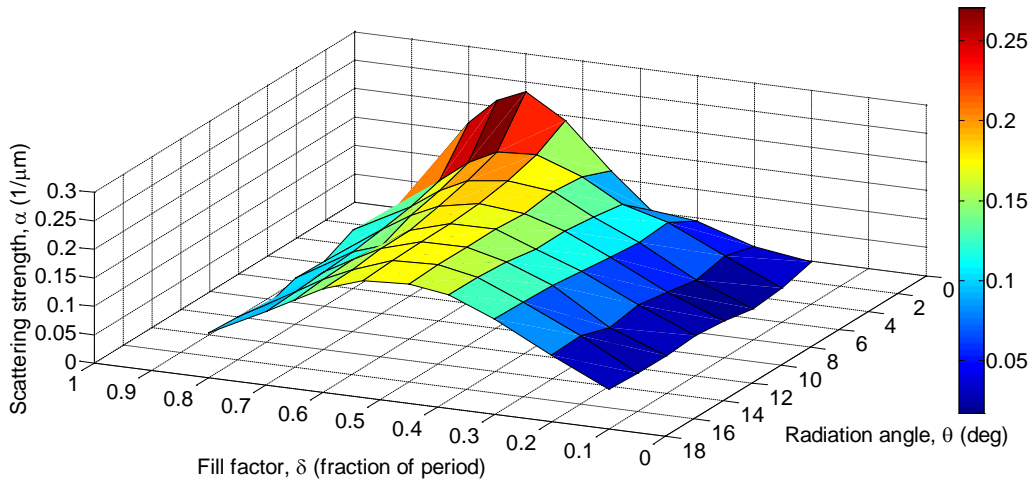
Figure 4.2: α vs. fill factor for fixed radiation angles θ in a range of 2° to 14° with the step of 2°.
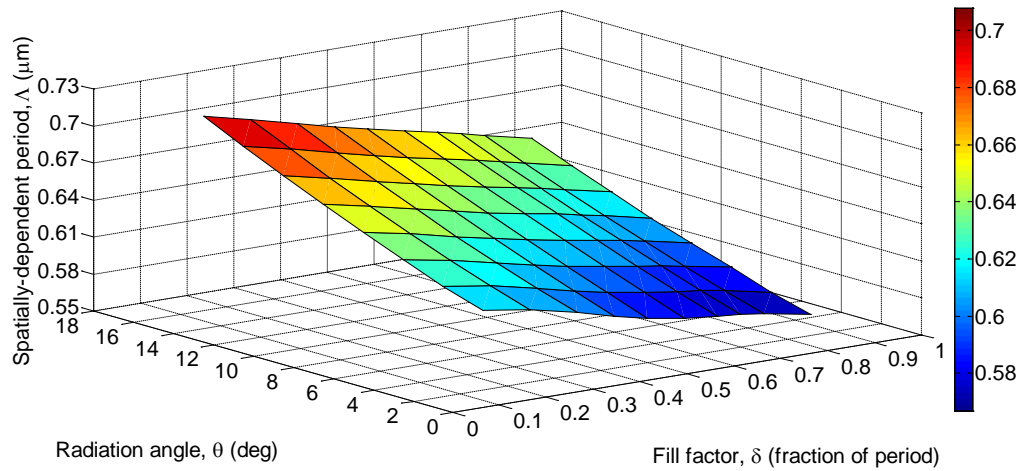
Figure 4.3: Period vs. fill factor for fixed radiation angles θ in a range of 2° to 14° with the step of 2°.

Step 4: For this step we first need the radiation angle $\theta(x)$ to form the initial arbitrary phase front. In our case for the presentation of the method, we chose a parabolic phase front and so the focusing grating coupler will launch the beam with such phase front. The following is the derivation of this angle $\theta(x)$.

The magnitude and the phase of the complex electric field vector of the launched beam along the grating were determined from the known magnitude and the phase of the Gaussian beam [62], taken at the distance d from the focus, and at the tilted angle (central angle) θ_c, where the y coordinate is neglected. The magnitude is given as [62]:

$$E_{magnitude} = \sqrt{\frac{2}{\pi}} \frac{\omega}{w(z\prime)} exp\left(-\frac{x\prime^2}{w^2(z\prime)}\right), \qquad (4.5)$$

and the phase is [62]:

$$E_{phase} = -\frac{\pi}{2} + tan^{-1}\frac{z\prime}{b} - \frac{k_{cl}z\prime x\prime^2}{2(z\prime^2+b^2)} - k_{cl}z\prime. \qquad (4.6)$$

From Figure 4.1, we write the matrix equation:

$$\begin{bmatrix} x \\ z \end{bmatrix} = \begin{bmatrix} sin\theta_c & -cos\theta_c \\ cos\theta_c & sin\theta_c \end{bmatrix} \begin{bmatrix} z\prime + d \\ x\prime \end{bmatrix}. \qquad (4.7)$$

In the matrix equation above the inverse matrix from the quadratic matrix is:

$$\bar{\bar{T}} = \begin{bmatrix} sin\theta_c & cos\theta_c \\ -cos\theta_c & sin\theta_c \end{bmatrix}, \qquad (4.8)$$

which is the transformation matrix. Multiplying matrix equation (4.7) with the transformation matrix (4.8) from the left side gives:

$$\begin{bmatrix} z' + d \\ x' \end{bmatrix} = \bar{\bar{T}} \begin{bmatrix} x \\ z \end{bmatrix} = \begin{bmatrix} x\,sin\theta_c + z\,cos\theta_c \\ -x\,cos\theta_c + z\,sin\theta_c \end{bmatrix}. \qquad (4.9)$$

The resulting transformed coordinates are:

$$z' = x\,sin\theta_c + z\,cos\theta_c - d, \qquad (4.10)$$

$$x' = -x\,cos\theta_c + z\,sin\theta_c. \qquad (4.11)$$

Substituting these coordinates in the expressions for magnitude (4.5) and phase (4.6), give the magnitude and phase of tilted Gaussian beam for angle θ_c in a coordinate system (x, z) of the grating; because the grating radiates beam with the radiation angle θ_c. The gradient of such a phase in tilted coordinate system gives wave vector $\vec{k}$ ($grad\,E_{phase}(x,z) = \vec{k}(x,z)$). In a result of gradient for z =

81

0, it is found that $\theta(x) = tan^{-1} \frac{k_x(x,z=0)}{k_z(x,z=0)}$ for the phase distribution along the x-axis. This expression for a tilt angle $\theta_c = 8^o$ gives continuum range of angles $\theta(x)$ of parabolic phase from 2° to 14°. This derived angle of radiation $\theta(x)$ is:

$$\theta(x) = tan^{-1} \left(k_{cl} \sin\theta_c - \frac{k_{cl}\sin\theta_c\,(-d+(x-m)\sin\theta_c)^2\,((x-m)\cos\theta_c)^2}{(b^2+(-d+(x-m)\sin\theta_c)^2)^2} + \right.$$

$$\frac{k_{cl}\sin\theta_c\,((x-m)\cos\theta_c)^2}{2(b^2+(-d+(x-m)\sin\theta_c)^2)} - \frac{k_{cl}\cos\theta_c\,(-d+(x-m)\sin\theta_c)\,(-(x-m)\cos\theta_c)}{b^2+(-d+(x-m)\sin\theta_c)^2} -$$

$$\left.\frac{\sin\theta_c}{b\,(1+(-d+(x-m)\sin\theta_c)^2/b^2)} \right) / \left(k_{cl}\cos\theta_c - \frac{k_{cl}\cos\theta_c\,(-d+(x-m)\sin\theta_c)^2\,((x-m)\cos\theta_c)^2}{(b^2+(-d+(x-m)\sin\theta_c)^2)^2} + \right.$$

$$\frac{k_{cl}\cos\theta_c((x-m)\cos\theta_c)^2}{2(b^2+(-d+(x-m)\sin\theta_c)^2)} + \frac{k_{cl}\sin\theta_c(-d+(x-m)\sin\theta_c)(-(x-m)\cos\theta_c)}{b^2(-d+(x-m)\sin\theta_c)^2} -$$

$$\left.\frac{\cos\theta_c}{b(1+(-d+(x-m)\sin\theta_c)^2/b^2)} \right); \qquad\qquad (4.12)$$

where $k_{cl} = 2\,\pi\,n_{cl}\,/\,\lambda_o$ is a spatial frequency in cladding, n_{cl} is a cladding refractive index, $\lambda_o = 1.55\ \mu m$, and m is the same as in Chapter 3 (and it is added in Equation (4.12) after the derivation).

In the 3D functions in Figures 4.2 and 4.2 the values between discretized angles with the step of 2° can be obtained by using an interpolation function. For example we used in Matlab function yinterp $= @(x_{in}, x_{data}, y_{data})$. Where x_{in} is a continuous value of $\theta(x_0)$ for a discrete value of x_0 [from Equation (4.12)], x_{data} is the range of angles from 2° to 14° with the step between them of 2°, and y_{data} can be either α or period vs. angles from 2° to 14° with the step between them of 2°

and one fixed fill factor. Therefore, the result is one continuous value of either α

or the period for that particular continuous angle $\theta(x_0)$. Then, these data are

inverted to map the grating strength vs. position to the non-uniform $\delta(x)$ and $\Lambda(x)$

vs. position. As a result of this algorithm, grating is depicted in Figure 4.4.
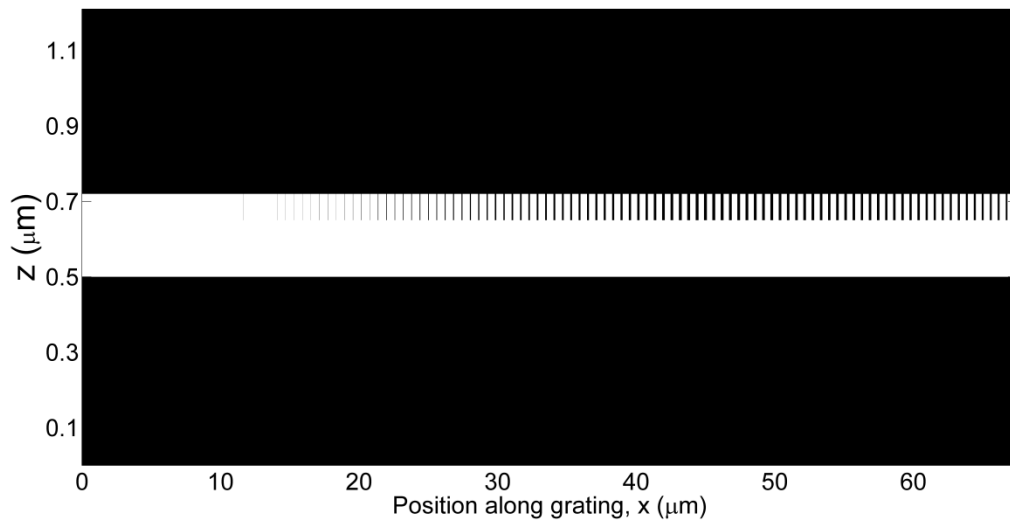
Figure 4.4: Non-uniform grating design which launches beam with Gaussian magnitude and parabolic phase front.

This grating launches a Gaussian beam shape depicted in Figure 4.5(a)

with a parabolic phase front depicted in Figure 4.5(b).
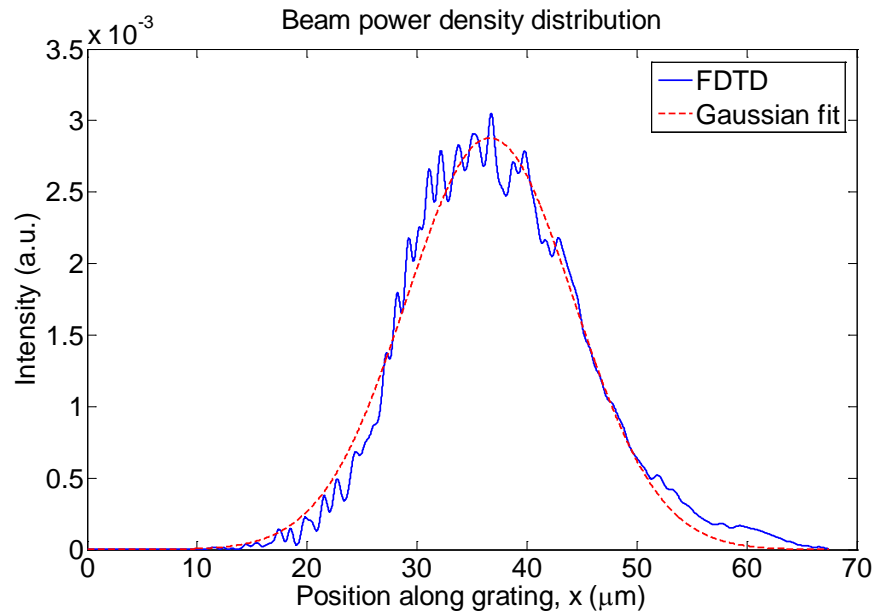
(a)
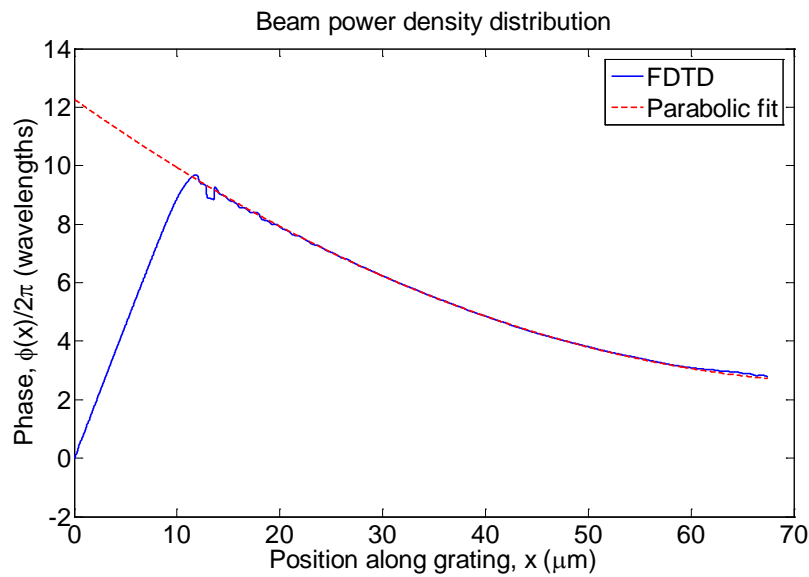
(b)

Figure 4.5: For MFD = 33.5 µm resulting: (a) Gaussian beam shape; (b) parabolic phase front.

For MFD = 33.5 um, resulting Gaussian beam shape has ~99% mode overlap between launched field and Gaussian mode. This Gaussian mode can be either from the optical fiber or the same (or other) focusing grating on the other chip. The resulting parabolic phase has a good fit with the perfect (theoretical) parabola in the spatial range along the grating, in which is the radiated field. This resulting parabolic phase front enables the focus of the Gaussian beam.

4.3 Application of direct method to strong (short) gratings

In this section, we apply our method to the two strong gratings fully within the constraints of the two existing different fabrication processes. These gratings are termed "strong" because they radiate optical power more rapidly (higher scattering strength α) than the weak gratings (which is why these strong gratings are shorter than the weak gratings). But the shortcoming of this shorter length is a rougher engineered radiated desired beam magnitude and phase front. On the other hand, the advantage of these short gratings is the smaller beam MFD across the grating than the beam MFD of longer grating so they can be coupled with the single-mode fiber.

4.3.1 Focusing grating within constraints of existing standard 45 nm SOI-CMOS foundry process

The first grating (with MFD = 11.7 µm) in this subsection is called theoretical, because just the structure agrees with the standard 45 nm SOI-CMOS foundry process [5], but not the width of some gaps. This grating core consists of two layers, poly-Si layer on top of body-Si layer. After the use of the method, the resulting grating has gaps all the way through its core (both layers) [5]. After performed FDTD simulation of this grating, the magnitude (Figure 4.6(a)) and the phase (Figure 4.6(b)) of the beam that this grating radiates are obtained.

For MFD = 11.7 um, the resulting Gaussian beam shape has 94% mode overlap between the launched field and the Gaussian mode. The resulting parabolic phase has a good fit with the targeting perfect (theoretical) parabola in a spatial range along the grating in which is the launched field. This MFD = 11.7 µm grating is suitable for chip-to-(single-mode)fiber coupling on the certain distance and also the chip-to-chip coupling. The difficulty is that this grating cannot be made by this [5] fabrication process. However, the next grating with MFD = 9.03 µm can be.

We needed to chop off the grating width of some gaps (teeth are appropriate) from the previous grating due to the constraints of the existing unmodified 45 nm SOI-CMOS foundry process [5]; this leads to a new grating which launches a Gaussian beam with the MFD = 9.03 µm. This grating is fully

Beam power density distribution

(a)

Beam power density distribution
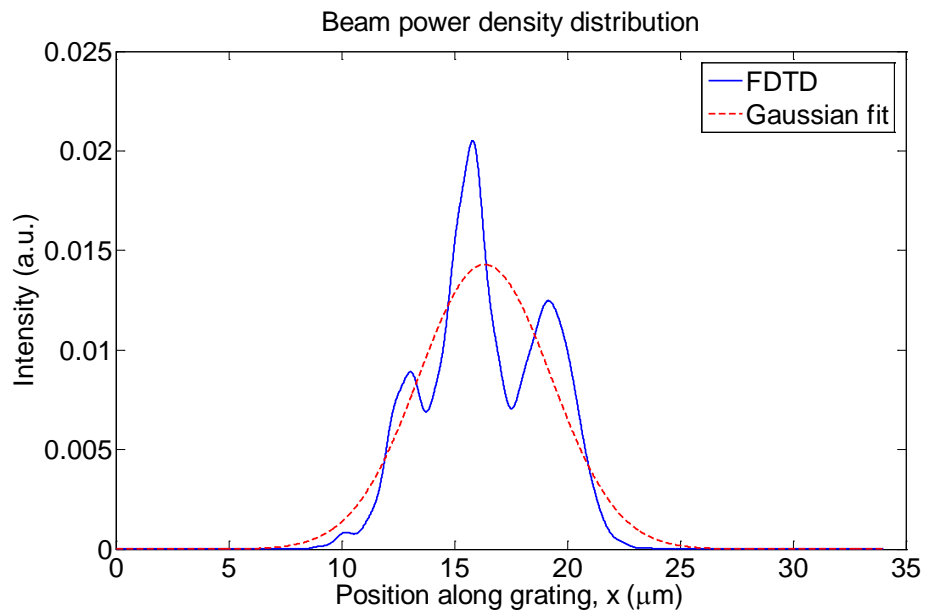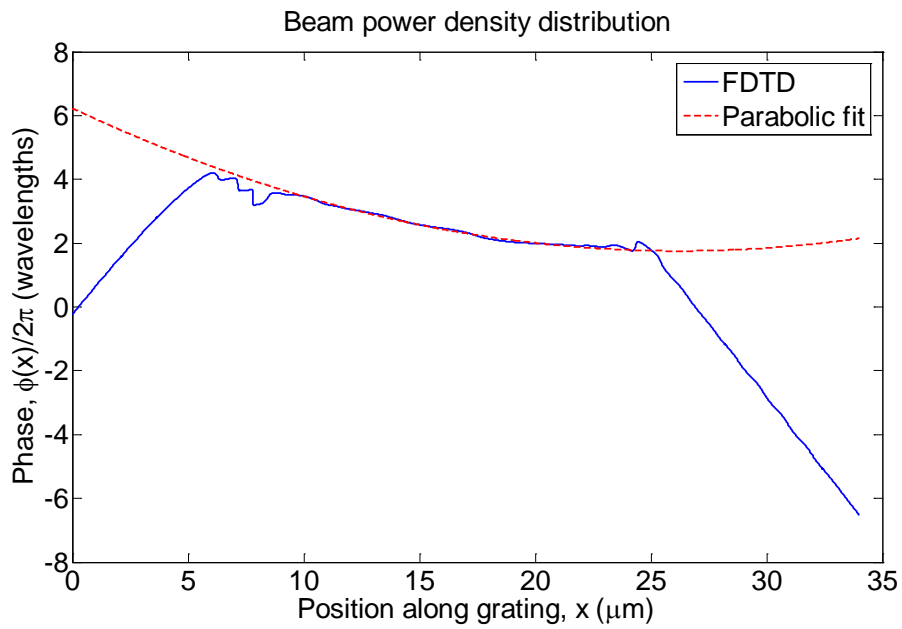
(b)

Figure 4.6: For MFD = 11.7 µm resulting: (a) Gaussian beam shape; (b) parabolic phase front.

within the constraints of the mentioned foundry process [5]. This MFD is at the distance of $z = 0$ and $z = L = 29.38$ μm from the grating, and at a distance $z>L$ it has a larger MFD. The chopping off has resulted in smaller MFD than the Gaussian beam MFD of the previous grating.

This resulting grating launches the Gaussian beam with the parabolic phase front which are depicted in Figures 4.7(a,b).

For this grating, the mode overlap is 85% between the launched field and the Gaussian mode. The resulting parabolic phase has a good fit with the target perfect (theoretical) parabola in a spatial range along the grating where the field is radiated.

This strong grating has worse resolution along the grating relative to the weak grating in Section 4.2 because it has a smaller number of tooth-gap and radiates power more rapidly. This is why it has smaller mode overlap than the weak grating from section 4.2. Also, this strong grating has smaller mode overlap than the previous strong grating because of the inappropriate width of some gaps that are chopped off for this [5] fabrication process.
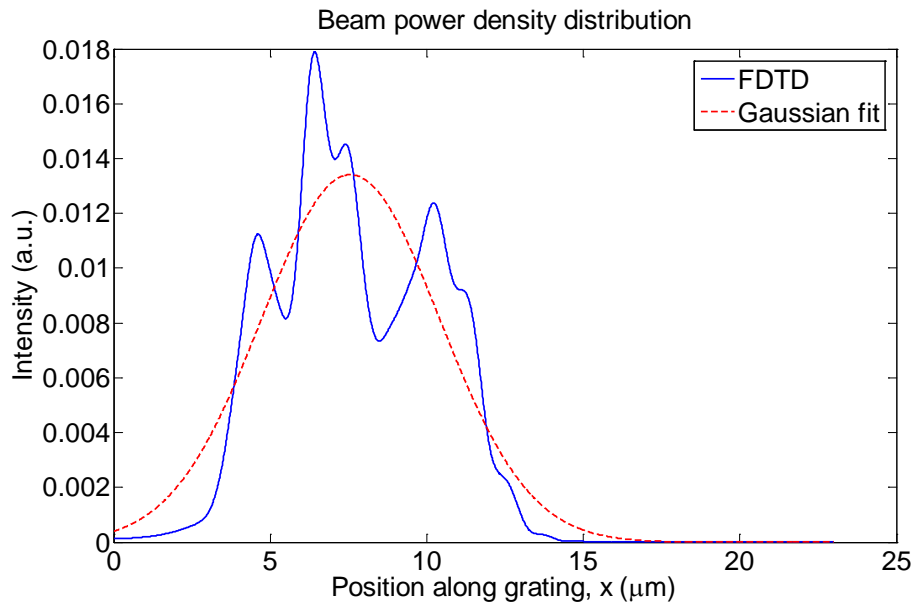
(a)
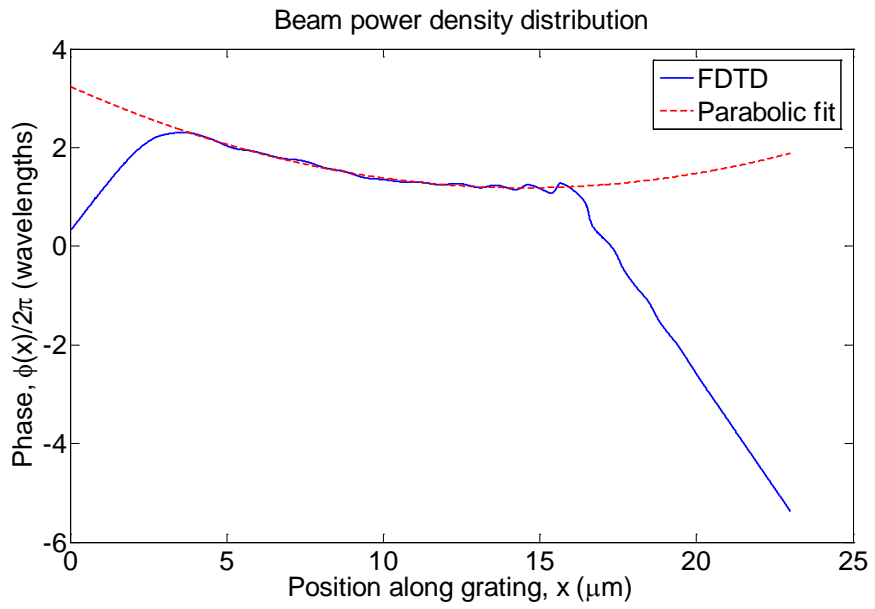
(b)

Figure 4.7: For MFD = 9.03 µm resulting: (a) Gaussian beam shape; (b) parabolic phase front.

4.3.2 Focusing grating within constraints of low-loss poly-Si core in an emulated high-volume electronics fabrication process

This non-uniform focusing grating is designed by using our method with the poly-Si core and oxide cladding in the existing low-loss poly-Si core in an emulated high-volume electronics fabrication process [96]. It has gaps all the way through the core. Figure 4.8(a,b) shows the Gaussian magnitude and parabolic phase front of the beam which this grating launches.

For this strong grating, the mode overlap between the launched field and the Gaussian mode is 88%. The resulting parabolic phase has a good fit with the target perfect (theoretical) parabola in a spatial range along the grating in which the field is radiated.
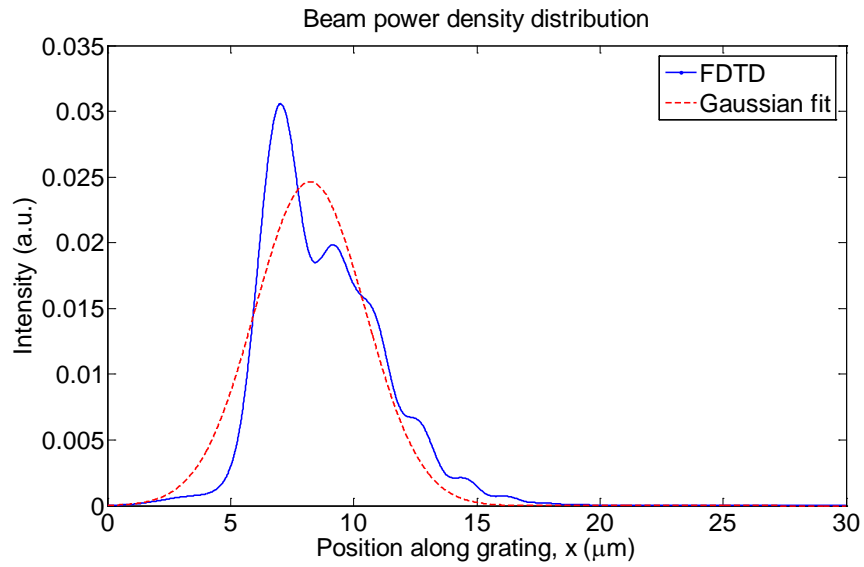
(a)
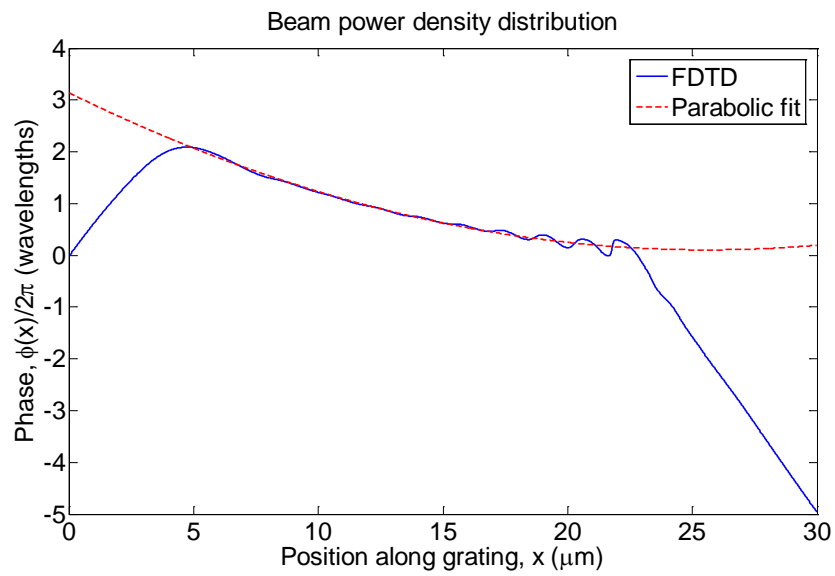
(b)

Figure 4.8: For MFD = 7.9 µm resulting: (a) Gaussian beam shape; (b) parabolic phase front.

4.4 Conclusions

In this chapter, we described a method for the automatic synthesis of a grating that launches a beam with a desired arbitrary magnitude and a desired arbitrary phase front. This method is demonstrated on a weak grating example that launches the beam with the Gaussian magnitude and the parabolic phase front. This produces a beam that focuses above the grating that radiates it, and such a grating is a focusing grating coupler. We demonstrated the method by designing two focusing strong gratings in two different existing fabrication processes. Both gratings with their launched beams achieve a good Gaussian magnitude mode overlap and parabolic phase front fit.

This method can be extended to incorporate the unidirectional grating design from chapter 2 such that high coupling efficiencies can be obtained.

Chapter 5

Novel algorithm for simulation of optical devices from contour files in 3D-FDTD

_____

5.1 Introduction

In this chapter, an algorithm (program) is presented which automatically extracts coordinates of an arbitrary optical device(s) geometry from a contour file, which is obtained after an optical proximity correction (OPC) is performed. This algorithm automatically builds a device for simulation in three-dimensions (3D) within the desired fabrication process, and also does simulation in three-dimensional finite-difference time-domain (3D-FDTD) numerical simulation method [45]. The purpose of the algorithm is to compare such a simulated device with the designed one so that, if needed, modifications of design can be made before fabrication occurs. Operation of this algorithm is demonstrated on the uniform grating coupler example.

There are commercialized 3D-FDTD simulators with the ability to manually import CAD files with arbitrary geometries [**https://www.lumerical.com/tcad-products/fdtd/features/**], [**http://empire.de/page157.html**], [**http://optics.synopsys.com/rsoft/rsoft-cad-environment.html**] (for example GDSII and DXF formats); and it is explained in [97] how to import CAD files in FDTD. In contrast with all of them (to the best of our knowledge), our algorithm automatically imports contour file with extension .mtv, which does not belong to CAD extensions. Also, for the first time building the 3D object(s) from the contour file is performed, which may contain many closed arbitrary curves as geometries of one or several optical devices. In addition, our algorithm does everything automatically, from the importing the optical device(s) from the contour file(s) to the performing the simulation of the 3D device(s). Moreover, our algorithm can automatically distinguish among each arbitrary closed curve (characterized by coordinates) and build a 3D object (optical device) or a 3D objects for the 3D-FDTD simulation in the desired foundry process.

In section 5.2 contour files are described. Section 5.3 is devoted to the explanations of our algorithm. Section 5.4 contains the results of our algorithm. And in section 5.5 conclusions are given.

5.2 Contour files

In Figure 5.1 are depicted three steps for obtaining the contour files. The layout of the designs on the chip goes through an OPC and afterwards the prediction of the device geometry after fabrication is made, which is stored in the contour files for devices on the chip.
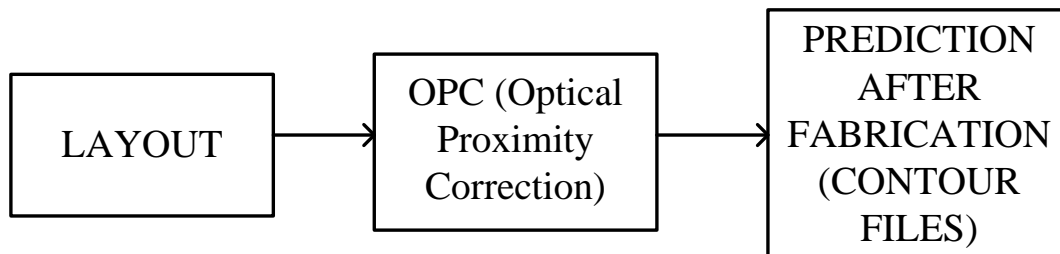
Figure 5.1: Steps in obtaining the contour files.

These steps explained in more detail are:

Step 1: The layout presents graphic designs of devices for the chip fabrication from the top view (surface of the chip). Each layer (material) can be seen from the top by keeping ON that layer and turning OFF layers above it. In the case of an optical device in which the core is for example Si (this can be combined with poly-Si or only poly-Si [5]), this Si layer presents the geometry from the top view. This geometry, within its contour, is filled with the points with the x and y coordinates.

Step 2: The OPC presents the correction of the layout device geometries for the fabrication error expressed as a geometrical deformity. For example, this fabrication error can be that the fabrication makes a geometrical deformity such as bulge in a certain place on the chip. A bulge is shown in Figure 5.2(a) for the case of geometry of rectangle (grating tooth). Then OPC will make mirrored bulge, which is dent. A dent is shown in Figure 5.2 (b).

(a)   (b)   (c)

Figure 5.2: Grating tooth example: (a) Fabrication error as bulge on certain place in deformed geometry; (b) OPC on that place makes mirrored bulge, which is dent; (c) Prediction after fabrication (contour of this geometry is characterized with x and y coordinates and this is contained in contour file).

Step 3: Based on Step 2, at the position of the deformed geometry should be an approximately flat line (Figure 5.2(c)) as a prediction after fabrication. This predicted geometry is presented in the form of the contour files with points of contours (that are closed arbitrary curves) with x and y coordinates on the chip (without coordinates inside of curves).

Curves plotted from the contour file for the uniform grating coupler example are shown in Figure 5.3, for a certain number of grating teeth (it has more teeth than in this Figure). Here, can be seen that coordinates with large values correspond to coordinates on the chip.
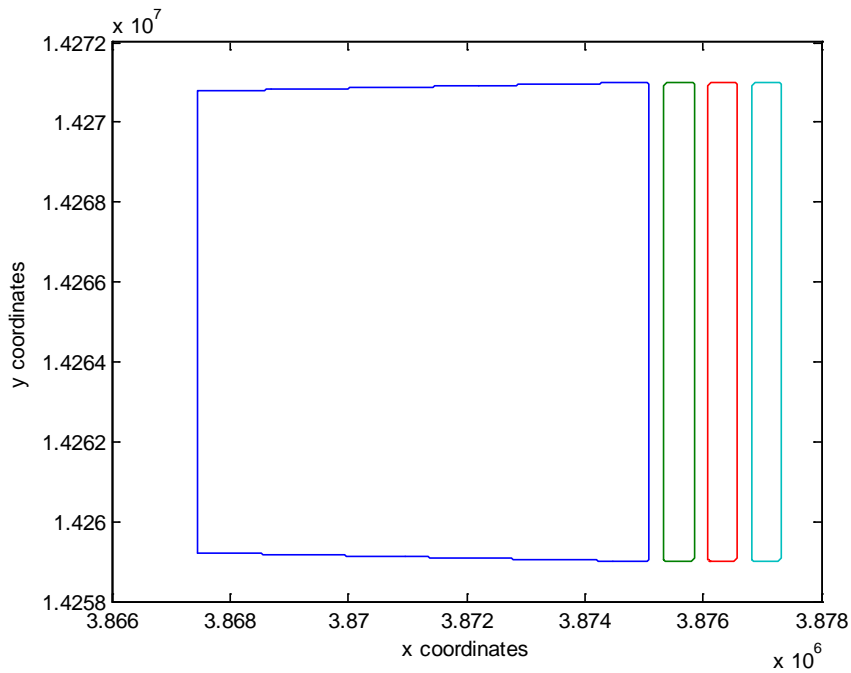
Figure 5.3: Plotted curves from contour file on the uniform grating coupler example for certain number of grating teeth (it has more teeth than in this Figure).

The contour file contains closed curves. Each curve starts with the word "Curve" and the space and a number. The number for the first curve is 0, so it is written "Curve 0", next is "Curve 1" and so on, depending how many closed curves contour file contains. Below each curve there are two columns, first with the x coordinates and second with the y coordinates. Thus, the contour file is a two-dimensional array of strings (this includes numbers as well). It may contain geometry as a part of the device, the whole device, or few devices. This depends on how each contour file is organized. If it contains more than one device, for example, two devices, then it has "Curve 0" repeated two times. The second time is after the end curve of the first device. The extension of the contour files is .mtv, and they do not belong to the CAD formats.

5.3 Algorithm

The algorithm in steps is shown in Figure 5.4. These steps explained in more detail are:

Step 1: The contour file as a two-dimensional array of string is imported and converted into the one-dimensional array of string cell. The string cell is a data type in Matlab, which we used. A number of closed curves (contours) and a number of devices (one device may have more than one closed curve) are determined in imported contour file. In addition, the beginning of each curve is found. If the number of devices is larger than one then, it is asked which ordinal

98

number user wants to choose, and for this device further processing of our algorithm is performed. This section of the algorithm also can be realized for simulation of more than one device (optical system or subsystem) at the same time.

```
┌─────────────────┐
│  Extracts data  │
│  in string cell │
│ array and finds │
│  beginning of   │
│   each curve    │
└─────────────────┘
         │
         ▼
┌─────────────────┐
│ Arranges x and y│
│   in matrix     │
└─────────────────┘
         │
         ▼
┌─────────────────┐
│Discretizes 3d object│
│ (grating) by x, y and z│
└─────────────────┘
         │
         ▼
┌─────────────────────┐
│ Gives appropriate value of│
│refraction index to every point│
│     of 3d object    │
└─────────────────────┘
         │
         ▼
┌─────────────────┐
│Gives parameters to 3D│
│   FDTD as domain,   │
│  layers, 3d object, │
│ source, observation │
│ planes, wavelength...│
└─────────────────┘
         │
         ▼
┌─────────────────┐
│Runs 3D FDTD and plot│
│     results     │
└─────────────────┘
```
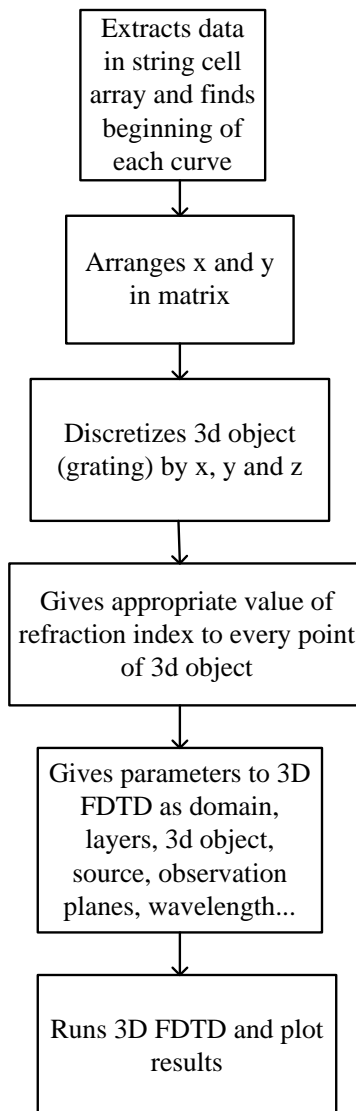
Figure 5.4: Algorithm in steps.

Step 2: After the step 1 when the beginnings of all curves are known, then both beginnings and ends of x and y coordinates for each curve are known as well. Then, the x and y coordinates for all curves for a chosen device are saved in a two-dimensional array (matrix). The smallest and the largest x and y coordinates are determined. The smallest x and y coordinates are treated as the origin of the coordinate system, so in the matrix with coordinates a values of coordinates are subtracted by the smallest x and y coordinates because this algorithm builds and simulates an optical device regardless to its position on the chip.

Step 3: Based on the minimum and maximum values of the coordinates, the size of the 3D device in the (x, y) plane and also the size of the (x, y) plane of the 3D computational domain are determined. In the z direction the thickness of the core of the 3D device is the height of the device itself. In our case of the test grating example the core is Si. Also, based on the fabrication process constraints and layer thicknesses along the z direction, the size in the z direction of the computational domain is determined. This completes the whole size of the 3D device and also 3D (x, y, z) computational domain. The discretization of the 3D object (device) along the x, y and z directions is performed for the desired discretization step.

Step 4: To every point within each contour (closed curve) and its thickness is assigned an appropriate value of the refractive index. This is done to the whole 3D device or devices (in our test example this is one 3D grating).

Step 5: Gives parameters to the 3D-FDTD: such as domain (x, y, z) sizes; discretization steps (dx, dy dz); wavelength range around the central wavelength and wavelength discretization step; layer thicknesses of fabrication process and their refractive indexes; 3D object (device from the contour file) with corresponding refractive index value for each point of the discretized 3D object, and also its chosen anchor point in the computational domain; optical source characteristics; observation planes; and so on.

Step 6: Runs simulation in 3D-FDTD and plots the results.

All presented steps above are fully automated; therefore, the entire algorithm is fully automated.

In the next section are presented results of our algorithm for the uniform grating coupler example.

5.4 Algorithm results

Figure 5.5 depicts results in terms of the 3D device from the contour file in the computational domain of our fully automated algorithm. For the test example of our algorithm, we chose uniform grating coupler. These results are obtained after performed 3D-FDTD simulation. They are presented for the horizontal (x, y) cross section of the grating (Figure 5.5(a)) and the vertical (x, z) cross section of the grating (Figure 5.5(b)). The algorithm showed good performances.

Refractive index distribution

(a)

Refractive index distribution
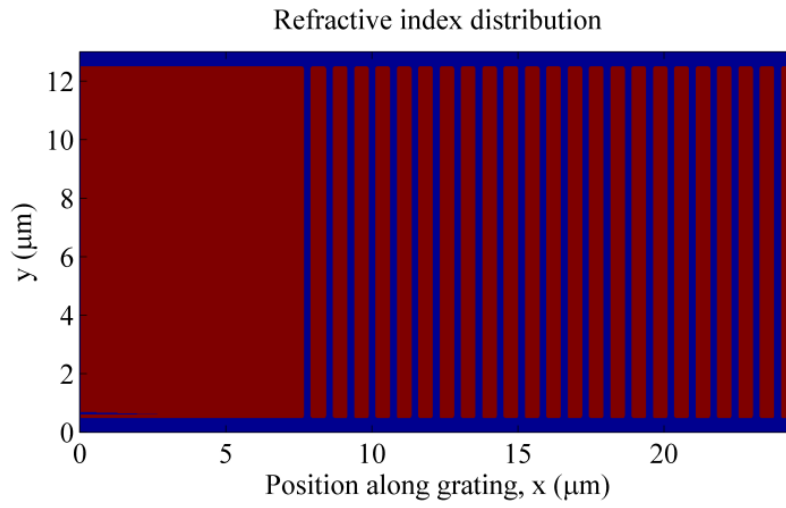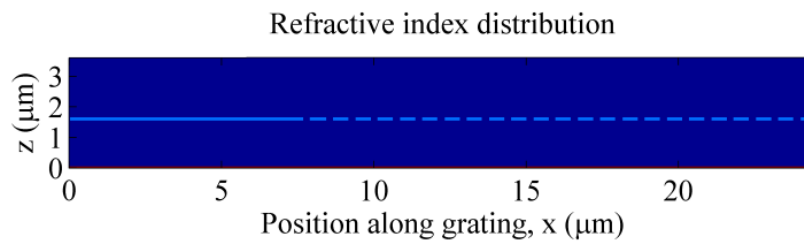
(b)

Figure 5.5: Results of algorithm by using 3D-FDTD for uniform grating example: (a) horizontal cross section; (b) vertical cross section.

The features of any built and simulated 3D device from the contour file can be compared with the features of the designed device. On this way, it can be seen in advance is designed device robust enough for the fabrication, or needs to be redesigned before fabrication occurs.

5.5 Conclusions

The fully automatic algorithm presented builds a 3D device(s) from the contour file(s) in the desired fabrication process, and does 3D-FDTD simulation in order to compare robustness of the designed device on fabrication errors expressed as geometrical deformities on the certain places. In this chapter, the algorithm is demonstrated on the 3D uniform grating example, and shows good performances.

Our algorithm is universal, therefore it can be applied on any contour file (or files) which consists of: any number of devices (by choosing one device or building and simulating arbitrary number of devices, as optical system or subsystem); any kind of the device (arbitrary shape, or in other words, arbitrary geometry of closed curves); and any number of points with x and y coordinates for each curve. All this with respect to the limits of the computer used.

When the author's previous MIT advisor, Professor Vladimir Stojanović (while he was at MIT), gave this algorithm task to the author, Professor V. Stojanović said to the author that in the same way as SPICE simulates circuits, this algorithm can be a beginning of a software which based on the geometrical shapes can build up and simulate photonic system (combination of several photonic devices) – this is how the author understood him.

Chapter 6

_____

A novel electronically-controlled optical switch

_____

6.1 Introduction

In the literature on (future) electro-optical computers there has been discussion of electronically-controlled optical switching between waveguides integrated on a chip. Three important criteria have been recognized for the design of this kind of switch: small area footprint, high switching speed (low switching time), and low energy consumption.

In this earlier work one finds proposals that include Mach-Zehnder interferometer (MZI) switches, directional coupler switches, dual mode interference switches, multimode interference (MMI) switches, and various other electrical control mechanisms; also papers discussing mathematical modeling and derivations, waveguide modes analysis, coupled-mode theory; and fabricated devices which have been tested [98-138]. We note that none of these switches has been designed within the constraints of the unmodified CMOS foundry process;

with the electronically controlled (through the free-carrier injection) switching mechanism by the driver circuit on the same chip in the same foundry process.

As an exception relative to the earlier work, there is an MZI switch [139] which was designed in IBM's 90 nm CMOS silicon integrated nanophotonics technology, with free-carrier injection controlled by the driver circuit on the same chip. Moreover, these CMOS process constraints are similar with the process constraints of the unmodified 45 nm SOI-CMOS foundry process [5], which we used for our switch designs. In the paper cited, this MZI switch has a length of the region of refractive index change in one arm of roughly 210 μm (which is relatively long); it is reported that this MZI switch has area footprint of 0.02 mm^2 (20000 μm^2). To turn this MZI switch ON, and to turn OFF, takes a total of 5.7 ns; the associated transients are 4.5 and 1.2 ns, respectively (measured between 10 and 90 % of the maximum). In addition, the switching energy (for turning ON and turning OFF) for this CMOS-driven MZI switch is inferred to be 16 pJ.

In contrast, the new switch designs we describe below in this chapter and Appendix A, with 1% refractive index decrease of Si which are within the constraints of the unmodified 45 nm SOI-CMOS foundry process [5], have a few hundred times smaller area footprint on the chip, a switching time that is several times shorter, and also several times smaller energy consumption. Due to the addition of two broadband 50% couplers, the bandwidth of 75 nm centered near a wavelength of 1520 nm for below -15 dB crosstalk between two output ports of

cited MZI switch is several times greater than the bandwidth of our switch designs; note that our switch designs are broadband and have bandwidths that are of the same order of magnitude as typical broadband MZI designs with free-carrier injection and no additional device for increase of bandwidth [130]. We do not use additional elements to increase the bandwidth of our switch designs.

Our optical switch design makes use of two TE mode interference for switching, as discussed in the next section. In [138] a thermo-optic dielectric loaded surface plasmon polariton waveguide switch also uses two mode interference for switching (referred to as "dual mode interference" in cited paper [138]) of the fundamental quasi-transverse magnetic (TM) polarized plasmonic mode and the second-order transverse-electric (TE) photonic mode. The mechanism in that case relies on thermal control using a metal film as the heating electrode; that is a very different control mechanism than employed in our proposed switch. That thermo-optic switch uses different core and cladding materials, and also a different kind of two modes than our switch. To the best of our knowledge our switch designs are the first to make use of two TE mode interference in Si-core and SiO_2-cladding for switching purposes, and also the first in using free-carrier injection with two TE mode interference, again for switching purposes.

We choose to focus on optical switch designs in this chapter and Appendix A for the specific application of switching optical data from a bus waveguide

toward electronic memory banks in (future) electro-optical computers (Figure 6.1). These switch designs also can be used in any other application of switching the light from one waveguide into other, and in any other appropriate topological arrangement.
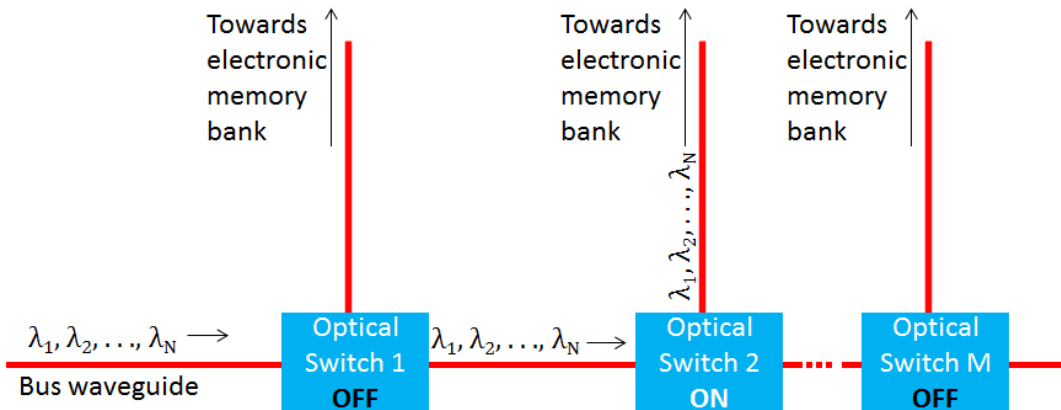
Figure 6.1: Illustration of possible usage of optical switches in future electro-optical computers (top view).

In [7] a digital driver circuit is applied to inject free carriers in a ring resonator modulator. In this chapter, we apply it for free-carrier injection in order to switch the optical data. In the case of our switch, when free carriers are injected in the refractive index change region, the refractive index of that region is decreased and so the propagation constants of the two interfered modes are changed, resulting in switching due to the final phase difference between the OFF state and the ON state just before the two output ports. In this case, in the ON state, as Figure 6.1 shows, optical data goes in second waveguide (toward the

electronic memory bank; but before the optical data reaches the electronic memory bank, it requires opto-electrical conversion through a photodetector integrated on the chip [8]); otherwise, in the OFF state, the optical data proceeds along the bus waveguide toward the next switch (if the previous switch is not the last switch, and if it is, then only proceeds along the bus).

Consequently, as an optimum choice to meet all three criteria for switch design mentioned above, we propose an electronically-controlled optical switch based on two mode interference, which relies on free-carrier injection in a PIN diode [140] in the horizontal junction, and makes use of the digital driver circuit developed previously in [7]. We focus on optical switch designs with a small area footprint. The driver circuit enables high switching speed and low energy consumption; it is capable of enabling sufficient injected free carriers to reduce the refractive index by 1% as required by our designs. The optical switch designs and driver circuit are both within the constraints of the same existing unmodified 45 nm SOI-CMOS foundry process [5], and therefore both of them can be fabricated on the same chip. Note that we also present a design with a higher refractive index decrease of 2.9%, which is feasible [141] to fabricate in a Si-core and SO_2-cladding foundry processes.

For the two mode waveguide (which is the refractive index change region) cross section of our switch design, we used the published cross section of a one mode ring resonator waveguide [7], shown in Figure 6.2.
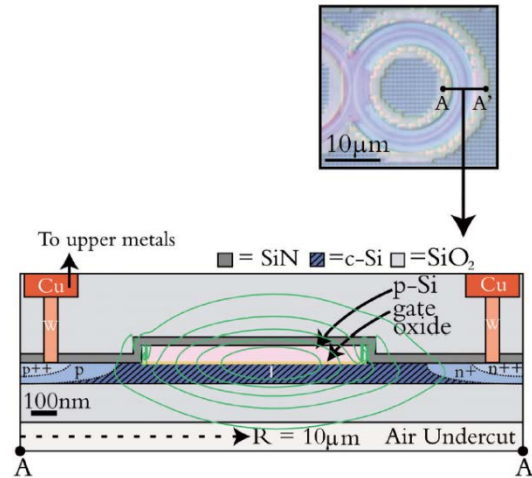
Figure 6.2: Optical ring resonator connection to modulator driver circuit (cross section with one mode waveguide contains PIN diode as well). From [7]. Structurally the same cross section in (x, y) plane would correspond to our optical switch designs with two mode waveguide when they are electronically controlled by this driver circuit.

In subsection 6.2.1 we describe our optical switch design; in subsection 6.2.2 we explained the optical operational principle; in section 6.2.3 we derive the model of our switch design; in section 6.3 the application of the driver circuit for switching purposes is discussed; section 6.4 contains the switch design for 2D-FDTD simulations and simulated interference of two modes; section 6.5 (and also appendix A) is devoted to optical switch design results; in section 6.6 is checked

validity of our derived analytical model through our switch designs; in section 6.7 are given switch design patterns based on which desired optical switch can be designed within its physics of operation; and conclusions are given in section 6.8.

All of the optical switch designs presented in this chapter and Appendix A are designed for a central wavelength of $\lambda_c = 1550$ nm; at room temperature the Si-core waveguide refractive index is $n_1 = 3.47644$; the SiO_2-cladding refractive index is $n_2 = 1.44402$. These refractive index values are found in [142] and [143] for λ_c at room temperature. Also, all optical switch designs are modeled using a two-dimensional finite-difference time-domain (2D-FDTD) numerical simulation method [45]. Since in the case of the switch designs under discussion, the field interactions are basically two-dimensional in the top view plane, it is appropriate to use 2D-FDTD in this plane for modeling, and also to understand the mechanism for how each switch functions.

6.2 Optical switch design

6.2.1 Description of design and its structural elements

The Figure 6.3 illustrates our switch design in the existing unmodified 45 nm SOI-CMOS foundry process [5]. In the top view plane (Figure 6.3(a)), the one mode Si waveguides are: the input waveguide in switch through which optical power P_0 propagates, first output waveguide through which optical power P_1 propagates, second output waveguide through which optical power P_2 propagates
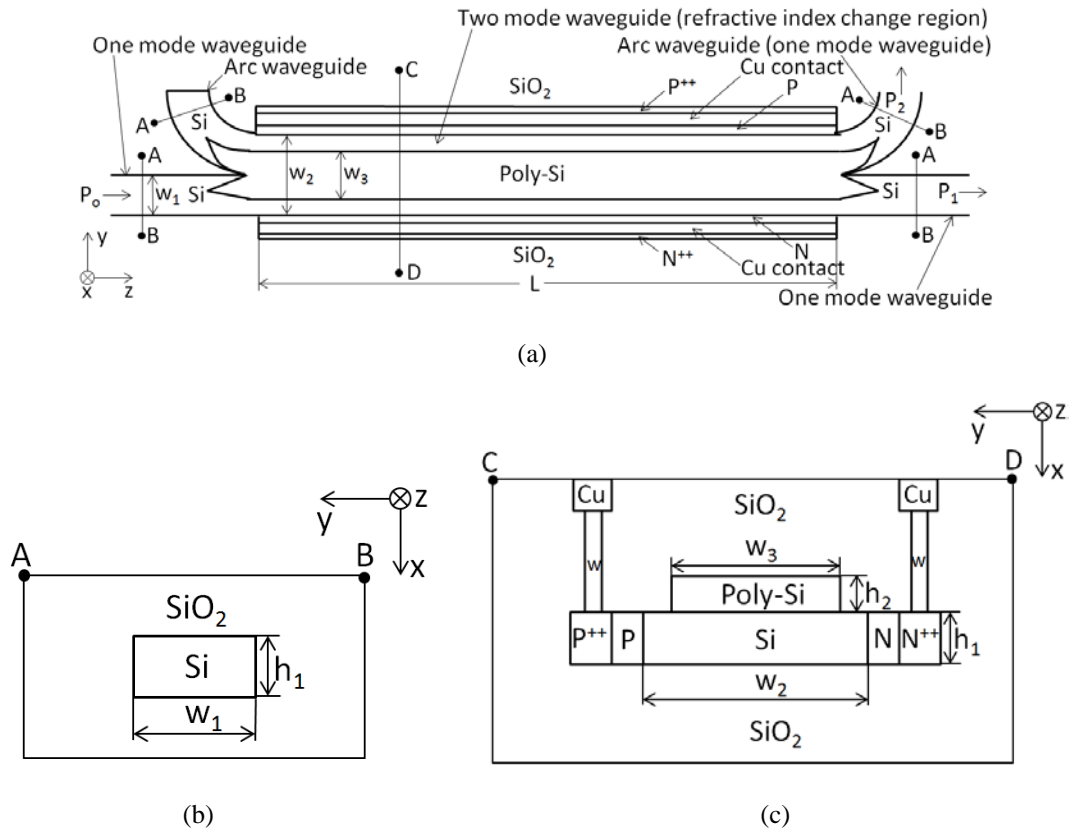
Figure 6.3: Illustration of switch design in 45 nm SOI-CMOS foundry process [5]: (a) top view (surface of chip); (b) cross sectional view of rectangular Si waveguide; (c) cross sectional view of rib waveguide with top Poly-Si layer and bottom Si layer.

(partly this is output arc waveguide), and input arc waveguide. Their cross section is depicted in Figure 6.3(b). Dimensions for these waveguides are w_1 and h_1, width and height, respectively. The input and the output Si waveguide through which optical powers P_0 and P_1 propagate, respectively, can be bus waveguide [see Figure 6.1]. In this case, the optical power P_1 propagates towards the next switch (if this switch is not the last switch), and power P_2 propagates towards the electronic memory.

At the input in the switch, we chose the Si arc waveguide [see Figure 6.3(a)] for the smooth transition, through coupling, from the one mode to the two modes regime. Also, in the end, the switch has a mirrored arc waveguide for an opposite smooth transition, from two modes into the one mode regime. In the extension of the arc waveguide at the end of the switch, light can be led in the direction that depends on the need. For example, this direction can be up [in the top view plane, as in Figure 6.3(a)] towards the electronic memory.

Figures 6.3(a,c) show the rib waveguide with the length L and two layers, which are the Poly-Si layer on the top of the Si layer. This rib waveguide guides two modes. The dimensions for Si layer are width w_2 and height h_1. While, the dimensions for Poly-Si layer are width w_3 and height h_2. A length L is also the length of the Si refractive index change region, which is the intrinsic region of the forward biased PIN diode [see Figure 6.2(c)]. In this region, the free carriers are injected in the two mode Si waveguide layer in the ON switching state, and not in the poly-Si layer due to significant loss. The PIN diode with the highly doped P++ and N++ regions, and contacts Tungsten (w) and Copper (Cu), is continuously placed along the length L [see Figures 6.3(a,c)].

In Figure 6.3(a), the Poly-Si tapers at the beginning of the switch and at the end enable smooth transitions from the one mode Si waveguide into the two mode rib, and also out of the rib waveguide back to the one mode Si waveguide. For the poly-Si taper on the top of the wider Si layer, on the example of a straight

one mode rib waveguide and a straight one mode Si waveguide, the author is thankful to Cheryl Sorace-Agaskar from MIT.

Cladding is SiO_2.

The switch geometry in terms of offset of the wider rib waveguide relative to the input Si waveguide is such that enables excitation of the two modes in the rib waveguide [see Figure 6.3(a)].

There is an optical loss in the mode overlap with the P and N regions of the PIN diode [see Figure 6.3(a,c)] which contains free carriers, mostly free holes and mostly free electrons due to P and N type dopants, respectively. This loss can be minimized by finding the optimum between the heights h_1 and h_2 and widths w_2 and w_3.

The Si material is isotropic and uniform unless it is stressed. Also, Si lattice is symmetrical in all three directions. Consequently, Si influences on the field on the isotropic and uniform way.

The presented switch geometry can be obtained by photolithography and etching in the standard CMOS fabrication processes [10].

This switch design is fully consistent with the existing unmodified 45 nm SOI-CMOS foundry process [5]. The estimated fabrication error of ±10nm in this foundry process [5] is negligible for dimensions of our switch designs in this chapter and Appendix A.

6.2.2 Operation principle

Our switch design operates by the following [follow Figure 6.3(a)]. In input of the switch is the optical power P_0 confined in the fundamental mode TE_{11} (or TE_0), which propagates along the z direction of the Si waveguide with the width w_1 [see Figures 6.3(a,b)] and the electric field of light is x-polarized [see Figure 6.4]. Input in the switch should not excite the TM_{11} (or TM_0) mode, and this can be regulated by the polarization of the input electric field in the waveguide that carries P_0. This polarization can be from a laser or can be further appropriately changed by polarizers before it reaches the chip and so input in the switch. At the beginning of the switch, the switch geometry (offset of the wider rib waveguide from Figures 6.3(a,c)) relative to the input Si waveguide with the width w_1 is such that enables excitation of both modes, TE_{11} (or TE_0) and TE_{21} (or TE_1) [see Figure 6.4(b)] within the rib waveguide (poly-Si layer with the width w_3 on top of the wider Si layer with width w_2) with a length L. These two modes interfere (mode beating) and resulting field travels from one side of the rib waveguide to the other side across its width (in the y direction) and propagates along the z direction (on the zigzag way). Eventually when this zigzag field reaches the output of the switch in the OFF state (no injected free carriers), most of the output optical power is P_1 and somewhat is P_2. In the ON switch state, when the free carriers (electrons and holes) are injected in the Si layer with width w_2 (refractive index change region) cause the plasma-dispersion effect [141,144], this layer has then

114

decreased the refractive index. This decrease alters the number of zigzags due to the change of the propagation constants β_1 and β_2 of the two interfered modes. In this case, the most of the output optical power is P_2 and somewhat is P_1, and this is how the switching is achieved.

(a)   (b)
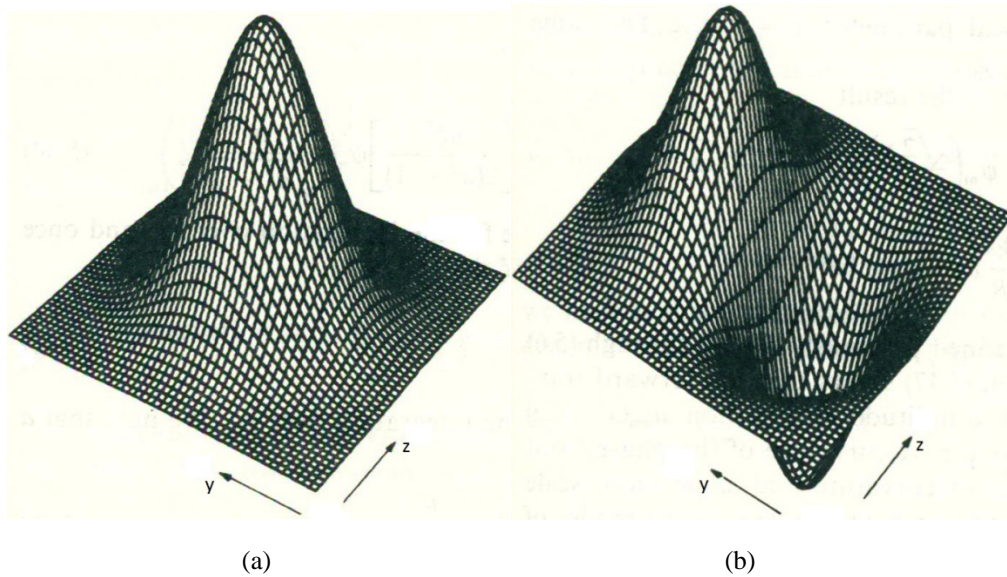
Figure 6.4: Illustration of modes in 3D: (a) TE_{11} (or TE_0); (b) TE_{21} (or TE_1). From [62].

The dimensions w_1 and h_1 of the Si waveguide [see Figure 6.3(b)] need to be such that the only fundamental mode TE_{11} [see Figure 6.4(a)] is confined. The first 1 in the subscript of TE correspond to the symmetric mode (Gaussian shape) along the y direction. And the second 1 in the same subscript correspond to the symmetric mode (Gaussian shape) along the x direction. Then, the dimensions w_2 and (again) h_1 of the wider Si layer and also w_3 and h_2 of the poly-Si top layer [see Figure 6.3(c)] of the rib waveguide need to be such that confines the TE_{21}

mode [see Figure 6.4(b)] besides the TE_{11}, and also to cutoff all higher modes than the TE_{21}. In the TE_{21}, the first subscript 2 corresponds to the antisymmetric mode (sine shape) along the y direction. And the second subscript 1 is the same as already explained for the TE_{11} second subscript 1. Consequently, this is why it is a good approximation for all optical switch designs in this chapter and Appendix A to be modeled using a two-dimensional finite-difference time-domain (2D-FDTD) numerical simulation method [45] instead of a 3D-FDTD. Since in the case of the switch designs under discussion, the field interactions are basically two-dimensional in the top view (y, z) plane, it is a good approximation to use 2D-FDTD in this plane for modeling. Also, a 2D model is appropriate to demonstrate and to study the mechanism based on which each switch design functions.

The known equation for the cutoff of the m-th order mode in the top view plane of the waveguide is [46]:

$$k_0 w \sqrt{n_1^2 - n_2^2} = m\pi, \qquad (6.1)$$

where k_0 ($=2\pi/\lambda_0$) is a spatial frequency in the vacuum, w is the width of the waveguide and n_1 is the Si-core refractive index and n_2 is the SiO_2 cladding refractive index. At the central wavelength $\lambda_0 = 1550$ nm and the room temperature, n_1 and n_2 have values mentioned at the end of the section 6.1, which are $n_1 = 3.47644$; the SiO_2-cladding refractive index is $n_2 = 1.44402$. By using the

Equation (6.1) for the confinement of the only first order mode (m=1), which is

the fundamental mode TE_0, the Si waveguide width needs to satisfy the condition

$w_1 < 245$ nm. Also, for the confinement of the first two order modes (m=2),

which are TE_0 and TE_1, the Si waveguide width needs to satisfy the condition 245

nm $< w_2 < 490$ nm. For 2D-FDTD simulations of the switch designs in the top

view plane in this chapter and Appendix A, we chose the safe values of $w_1 = 220$

nm and $w_2 = 440$ nm.

In next subsection 6.2.3, the switch design operational principle with

resulting zigzag field is illustrated. In section 6.4 of the switch design for the 2D-

FDTD simulations, the switch operational principle is explained on the example

of simulated interfered field of the two modes.

6.2.3 Analytical model of our switch design

The known equation for the phase difference which we are using for the analytical

model of our switch is:

$$L \, \Delta\beta = \Delta\varphi. \qquad (6.2)$$

Where $\Delta\beta$ denotes the propagation constants change for the two modes from the

OFF state to the ON switching state, and it is:

$$\Delta\beta = (\beta_{1,ON} - \beta_{2,ON}) - (\beta_{1,OFF} - \beta_{2,OFF}). \qquad (6.3)$$

The propagation constant of the TE_0 mode is β_1, and the propagation constant of the TE_1 mode is β_2. And $\Delta\varphi$ is the phase difference of the two interfered modes from the OFF state to the ON switching state.

In order to show the functionality of Equations (6.2) and (6.3) in Figure 6.5(a,b) is illustrated resulting zigzag field of interfered two modes TE_0 and TE_1, in the two mode region (refractive index change region) of length L. The functionality (switching) is illustrated for OFF and ON (injected free carriers in Si) switching state for the phase difference $\Delta\varphi = \pi$ between the ON and OFF switching states.

In Figure 6.5(a) in OFF state, there are 6 zigzags which correspond to 6π phase, so in this case the last zigzag propagates towards the next switch. We named that the one zigzag corresponds to π phase. While in Figure 6.5(b) in ON state, there are 7 zigzags which correspond to 7π phase, so in this case the last zigzag propagates towards the electronic memory. The phase difference $\Delta\varphi = 7\pi - 6\pi = \pi$ corresponds to exactly one more zigzag in ON state than in OFF state, which enables the switching.
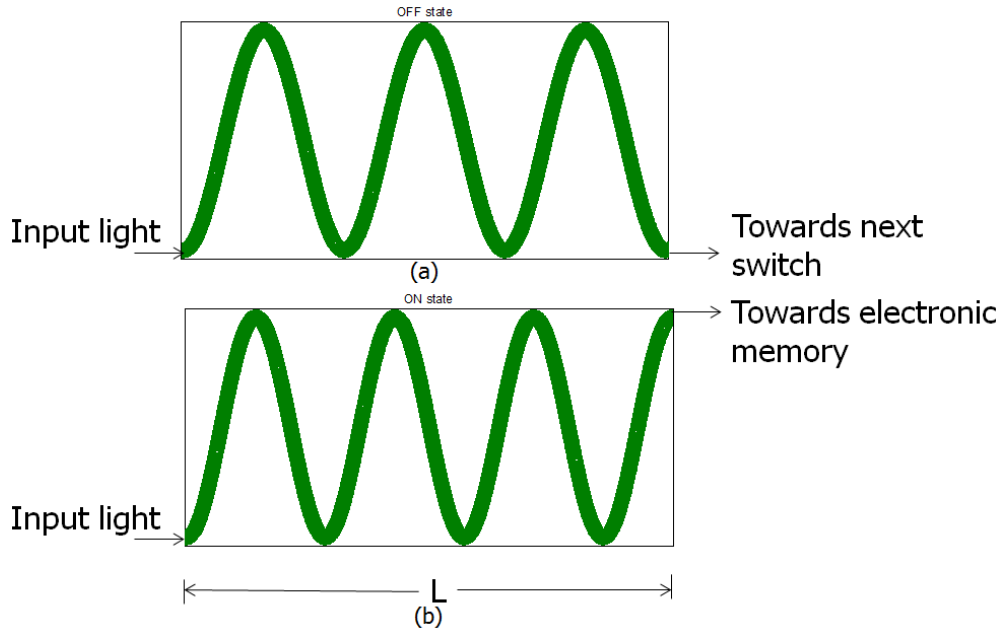
Figure 6.5: Switching illustration in two mode region (refractive index change region) in top view (y, z) plane for phase difference $\Delta\varphi = \pi$: (a) OFF state; (b) ON state (exactly one more zigzag than in OFF state).

In order to have a complete analytical model for our switch, in the following we derived propagation constants β_1 and β_2.

The wave equation for the electric field E derived from the complex form of Maxwell's equations is [46]:

$$\nabla^2\vec{E} + \omega^2\varepsilon\mu\vec{E} = 0, \qquad (6.4)$$

where ∇ is the del operator (square of it is the Laplace operator ∇^2), ω is the temporal frequency, ε is the dielectric permittivity and μ is the magnetic

permeability. For the TE field, the vector of electric field $\vec{E}$ is x-polarized in our case; it does not depend from x coordinate so the above equation can be written in the form of the eigenvalue equation:

$$\left[\left(\frac{\partial^2}{\partial y^2} + \frac{\partial^2}{\partial z^2}\right) + \omega^2 \varepsilon \mu\right] \vec{E} = 0. \qquad (6.5)$$

For this derivation, it is used the right orientation of coordinate system (x, y, z) as it is in the Figures 6.3(a,c), with the origin on the half width $w_2/2$ of the two mode Si waveguide (refractive index change region; without the poly-Si layer) with the full width w_2 (for our switch designs, $w_2 = 0.44$ μm). Then, it has the permittivity ε_1 in the Si waveguide and ε_2 in the SiO_2 cladding. Under these conditions, the electric field vector in TE case satisfies the Equation (6.5) with a solution:

$$\vec{E} = \hat{x} e^{-j\beta z} \cdot \begin{cases} E_2 e^{-\alpha\left(y - \frac{w_2}{2}\right)}, & y \geq \frac{w_2}{2} \\ E_1 \cdot \begin{bmatrix} cos(k_y y) \\ sin(k_y y) \end{bmatrix}, & -\frac{w_2}{2} \leq y \leq \frac{w_2}{2}, \\ E_2 e^{\alpha\left(y + \frac{w_2}{2}\right)}, & y \leq -\frac{w_2}{2} \end{cases} \qquad (6.6)$$

where β ($\beta = k_z$) is the propagation constant, k_y is the y component of the wave vector $\vec{k}$, and α is the decay rate coefficient of the exponentially decaying evanescent field in the SiO_2 cladding (in this subsection, this is not the absorption

120

α). Within the waveguide full width w_2, the cosine function across it characterizes the even modes (with the subscript 0) $TE_{0, 2, 4, ...}$; while, the sine function characterizes the odd modes $TE_{1, 3, 5, ...}$. By plugging in the above solution in the Equation (6.5), it is obtained:

$$k_y^2 + \beta^2 = k_1^2; \qquad (6.7)$$

$$-\alpha^2 + \beta^2 = k_2^2; \qquad (6.8)$$

where, $k_i^2 = \omega^2 \varepsilon_i \mu_i = k_o^2 n_i^2$, for i = 1, 2 and $k_o = 2\pi/\lambda_o$ (λ_o = 1.55 μm).

When the Equation (6.8) is subtracted from the Equation (6.7), the resulting equation is:

$$k_y^2 + \alpha^2 = k_o^2(n_1^2 - n_2^2). \qquad (6.9)$$

Therefore, α is:

$$\alpha = \sqrt{k_o^2(n_1^2 - n_2^2) - k_y^2} \,. \qquad (6.10)$$

By employing the boundary condition in the Equation (6.6) for the tangential

vector $\vec{E}$ at the boundary y = w₁/2 between ε_1, ε_2, it is obtained:

$$E_2 = E_1 \cos\left(k_y \frac{w_2}{2}\right);$$ (6.11)

$$E_2 = E_1 \sin\left(k_y \frac{w_2}{2}\right).$$ (6.12)

By applying the Faraday's law from the complex form of the Maxwell's

equations:

$$\nabla \times \vec{E} = -j\omega\mu\vec{H},$$ (6.13)

on the electric field solution in the Equation (6.6), it is obtained for the magnetic

field z component:

$$H_z = -\frac{1}{j\omega\mu} e^{-j\beta z} \cdot \begin{cases} -\alpha E_2 e^{-\alpha\left(y-\frac{w_2}{2}\right)}, & y \geq \frac{w_2}{2} \\ k_y E_1 \cdot \begin{bmatrix} -\sin(k_y y) \\ \cos(k_y y) \end{bmatrix}, & -\frac{w_2}{2} \leq y \leq \frac{w_2}{2}. \\ \alpha E_2 e^{\alpha\left(y+\frac{w_2}{2}\right)}, & y \leq -\frac{w_2}{2} \end{cases}$$ (6.14)

In the equation above, within the waveguide full width w_2 the sinus function characterizes the even modes; while the cosine function characterizes the odd modes $TE_{1, 3, 5, ...}$. By employing the boundary condition in the Equation (6.13) for the tangential component H_z of the vector $\vec{H}$ (the surface current density $J_s = 0$) at the boundary $y = w_2/2$ between ε_1, ε_2, it is obtained:

$$\alpha E_2 = k_y E_1 \sin\left(k_y \frac{w_2}{2}\right); \qquad (6.15)$$

$$\alpha E_2 = -k_y E_1 \cos\left(k_y \frac{w_2}{2}\right). \qquad (6.16)$$

By substituting E_2 from Equations (6.11) and (6.12) into Equations (6.15) and (6.16), the following two Equations are obtained, respectively:

$$\alpha = k_y \tan\left(k_y \frac{w_1}{2}\right); \qquad (6.17)$$

$$\alpha = -k_y \cot\left(k_y \frac{w_1}{2}\right). \qquad (6.18)$$

Further, by substituting α from the Equation (6.10) into the both Equations (6.17) and (6.18), and then dividing each equation by k_y, resulting two equations are, respectively:

$$\sqrt{\frac{k_o^2}{k_y^2}(n_1^2 - n_2^2) - 1} = tan\left(k_y \frac{w_2}{2}\right), \quad 0 < k_y < \left(\frac{\pi}{2}\right)\left(\frac{2}{w_2}\right) = \frac{\pi}{w_2}; \qquad (6.19)$$

$$\sqrt{\frac{k_o^2}{k_y^2}(n_1^2 - n_2^2) - 1} = -cot\left(k_y \frac{w_2}{2}\right), \quad \left(\frac{\pi}{2}\right)\left(\frac{2}{w_2}\right) = \frac{\pi}{w_2} < k_y < (\pi)\left(\frac{2}{w_2}\right) = \frac{2\pi}{w_2}.$$

$$(6.20)$$

In general (without given ranges for the k_y), the equation (6.19) corresponds to the even modes, while the Equation (6.20) corresponds to the odd modes. These two equations above are the transcendental equations, and they can be solved numerically or graphically for the each unknown k_y. From the Equation (6.7) follows:

$$\beta = \sqrt{\left(\frac{2\pi}{\lambda_o}n_1\right)^2 - k_y^2}. \qquad (6.21)$$

In the case of our switch design is the following. Now through the Equation (6.21) the propagation constants β_1 can be calculated from k_y from the Equation (6.19), when the solution of k_y is in a given range for this equation. This k_y range corresponds to the mode TE_0, and k_y can be calculated for the both states of the switch, OFF and ON (any value of the Si refractive index n_1 in the two

mode region). Likewise, through the Equation (6.21) the β_2 can be calculated from k_y from the Equation (6.20), when the solution of k_y is in a given range for this equation. This k_y range corresponds to the mode TE_1, and k_y can be calculated for the both states of the switch, OFF and ON (any value of the Si refractive index n_1 in the two mode region). This makes the analytical model of our switch design complete; this model is given by Equation (6.2) through the Equations (6.3), (6.21), (6.19) and (6.20). In our model k_y depends on n_1 (in the ON state, this depends on the injected free-carrier concentration), n_2, λ_0 (through k_0), and w_2, for each of the two modes. Since β depends on n_1, λ_0, and k_y, then β_1 and β_2 for the two modes depend on n_1, n_2, λ_0, and w_2, so that $\Delta\beta$ also depends on n_1, n_2, λ_0, and w_2. The previous finally means that if length L is unknown, then it depends (through $\Delta\beta$) on n_1, n_2, λ_0, and w_2, and also on $\Delta\varphi$.

Based on the form of Equations (6.2) and (6.3) we can calculate the period of zigzags (two zigzags) P that corresponds to the phase $\varphi = 2\pi$ for OFF or ON state by the following Equation:

$$P = \frac{2\pi}{(\beta_1 - \beta_2)_{OFF \, or \, ON}}. \qquad (6.22)$$

Also, based on the same form of Equations (6.2) and (6.3) we can calculate the number of zigzags N for any length l within the two mode region with length L for OFF or ON state by the following Equation:

$$N = \frac{(\beta_1 - \beta_2)_{OFF\ or\ ON} \cdot l}{\pi}. \qquad (6.23)$$

In section 6.6, we will check the validity of our analytical model through our switch designs.

6.3 Driver circuit for free-carrier injection in switching applications

The all-digital driver circuit is applied in [7] for free-carrier injection into the optical ring resonator modulator [see Figure 6.2], and in this section we apply the same driver circuit design for free-carrier injection into our optical switch designs, which enables switching. This driver circuit can inject free carriers (electrons and holes) which enable the Si-core uniform refractive index decrease of 1% (Δn = 0.03476) for n_1 = 3.47644, which produces a new Si-core refractive index of 3.44168. This decrease occurs when the switch is ON and so when the free carriers are injected into the intrinsic (I) region of the forward biased PIN diode [140] (in the horizontal junction) with a uniform free-carrier (electrons and holes) concentration of ~3×10^{19} cm^{-3} [see Figure 6.6], according to Figure 6.7 (from [141]). The intrinsic region is the refractive index change region of the two modes interference Si waveguide with length L.

According to Figure 3-6 in [6], the above mentioned injected free-carrier concentration can be achieved using a voltage across PIN diode of roughly ~0.8 V. This voltage provides a uniform distribution of injected free carriers (electrons and holes) [see Figure 6.6] and so a uniform refractive index decrease, across the width of two modes interference Si waveguide. Furthermore, this diode voltage would correspond to a driver circuit HVDD voltage of roughly ~1.1 V. The voltage across the PIN diode is lower than the HVDD voltage for around 0.3 volts due to the decrease of the voltage on the on-resistance of the NMOS and PMOS transistors which are in series with the PIN diode (Figure 7.6.4 in [7]). In order to achieve an injected free-carrier concentration, the P and N regions are doped with a concentration of roughly ~2×10^{18} cm^{-3}, according to Figure 3-6 in [6].
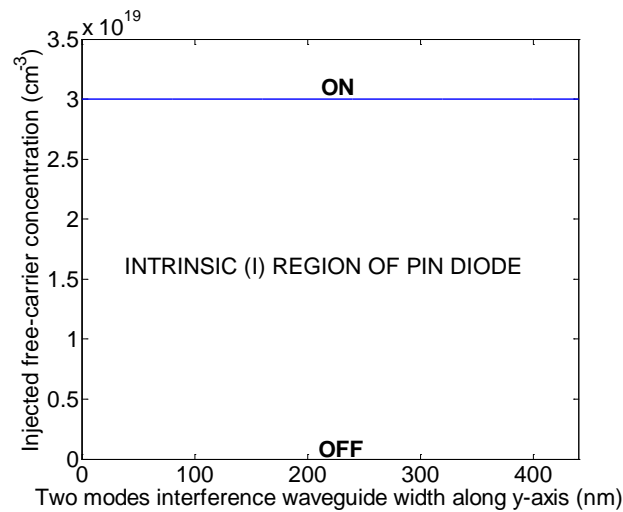
Figure 6.6: Injected free-carrier (electrons and holes) concentration in two modes interference Si waveguide of width 440 nm (intrinsic region of PIN diode), for OFF and ON (voltage across PIN diode is ~0.8 V) states of switch. We made this plot based on data in Figure 3-6 from [6].
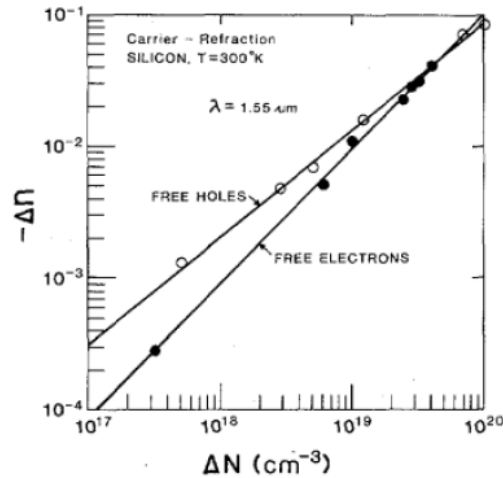
Figure 6.7: Si refractive index decrease Δn vs. injected free carriers concentration ΔN for wavelength of 1550 nm and room temperature. From [141].

According to Figure 7.6.6 in [7], an HVDD voltage of 1.1 V in the driver circuit gives an energy consumption of 0.68 pJ/b for a speed of 2.5 Gb/s. From Figure 6.2 (from [7]), where is a ring resonator modulator for which the driver circuit is applied to inject free carriers, we extracted a length of 54.6 μm for the circularly curved waveguide (most of the ring) along which the PIN diode with highly doped P++ and N++ regions, and contacts (tungsten (W) and copper (Cu)), is continuously placed. Our switch along length L (z-axis) would have a structural cross section from Figure 6.2 [see Figure 6.3(a,c)], which corresponds to the x-y plane of our switch [see Figure 6.3(a) for axes of this plane] when realized with the rib waveguide in 3D. When an energy consumption of 0.68 pJ/b is divided by a length of 54.6 μm, an energy consumption of 12.45 fJ/(b μm) per bit and unit length of 1 μm, is obtained. Energy consumption and speed of modulation are

both expressed per bit. Modulating one bit of information corresponds to one switching operation of N bits (λ_1, λ_2,…, λ_N), in a case when this same driver circuit is applied to electronically control our optical switch. These N bits (λ_1, λ_2,…, λ_N) propagate all together along the waveguide (it is WDM) and this means that switching operation is performed simultaneously for all these bits (so for the same switching time, regardless of the number N of these bits). For example, for one switching operation of N bits (λ_1, λ_2,…, λ_N) for a refractive index change region of length L expressed in μm, the energy consumption is E = 12.45•L fJ and the switching time is τ = 1/(2.5 10^9/s) = 400 ps. This switching time is approximately the same for any length L in this chapter and Appendix A (for switch designs which can use mentioned driver circuit [7]) and it takes into account carrier lifetime as well. By multiplying 12.45 fJ/(b μm) and 2.5 Gb/s, the obtained power consumption per unit length for any number of N bits is 31.13 μW/μm. For example, for one switching operation of any number of N bits for a refractive index change region of length L expressed in μm, the power consumption is P = 31.13•L μW. Energy and power consumptions are given in Appendix A in Table A.4 for different switch design lengths L.

From Figure 5 in paper [5] (the same mentioned foundry process) we extracted (by dividing the full bandwidth of eight optical channels by 8) the full width of one optical channel, which is ~1.37 nm. This value will be used as a referent value for number N of full width optical channels in further analysis of

multiple channels (broadband) switch designs. Each channel at central wavelength λ_i is within one full width channel of 1.37 nm, and this corresponds to one bit, in the case of our analysis in this chapter and Appendix A. Therefore, if there are N central wavelengths ($\lambda_1, \lambda_2, \ldots, \lambda_N$), which are within the full width of N channels, then these correspond to N bits. Each of these N wavelengths is central within its corresponding one full width optical channel, and they are all around the main central wavelength of 1550 nm.

For a bandwidth analysis of each switch design it is useful to know which full wavelength bandwidth (range) $\Delta\lambda$ (full width of a certain number N of optical channels) corresponds to the full frequency bandwidth $\Delta\nu$. This conversion is performed using well known Equation (6.24) and results are given in Table 6.1.

$$\Delta\nu = \frac{c}{\lambda_c^2}\Delta\lambda, \qquad\qquad (6.24)$$

where c is the speed of light in a vacuum, and $\Delta\lambda = N \cdot 1.37\ nm$.

Table 6.1: Conversion of full wavelength bandwidth $\Delta\lambda$ into the full frequency bandwidth $\Delta\nu$ by the number N of full width optical channels.

Number N of full width optical channels	1	2	4	8	16
$\Delta\lambda$ (nm)	1.37	2.74	5.48	10.96	21.92
$\Delta\nu$ (GHz)	171	342	684	1368	2736

6.4 The switch design for 2D-FDTD simulations

In this section we will explain the switch design in the form for 2D-FDTD simulations. Also, we will demonstrate simulated optical operation principle of two mode interference (mode beating).

The optical switch design for the 2D-FDTD simulations is depicted in Figure 6.8(a) in the OFF state [follow this Figure in further explanations]. We assume that the optical signal on the Si bus waveguide contains optically encoded data on all of the different channels, and we would like to switch all of the channels towards the electronic memory bank, or continue all of the channels along the bus towards the next switch. This incoming bus waveguide with a width of 220 nm supports only a single TE_0 mode. The wider Si waveguide with a width of 440 nm (refractive index change region) of the optical switch supports two TE modes (TE_0 and TE_1 with mode profiles shown in Figure 6.9). When the bus waveguide reaches the wider waveguide, the single mode of the bus splits its optical power into the two modes of the switch. The switch operates optically by interference of these two modes (mode beating). The resulting light travels back and forth (on the zigzag way) from one side of the waveguide into the other [see zoomed-in Figure 6.8(c) for CW field]. For an appropriate length L, with no injected free carriers present (switch is OFF), the final result of the interference is to couple the light mostly into the single mode of the outgoing bus waveguide
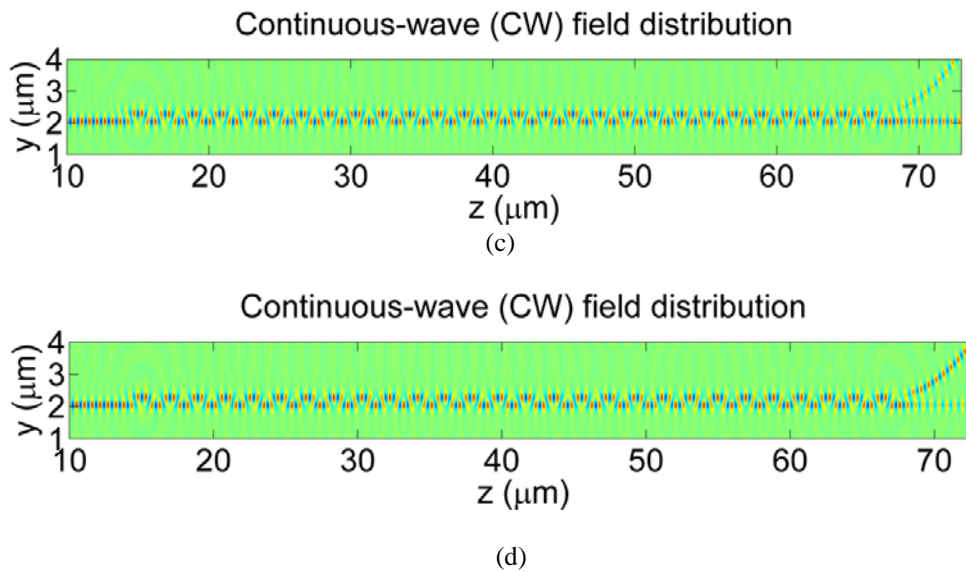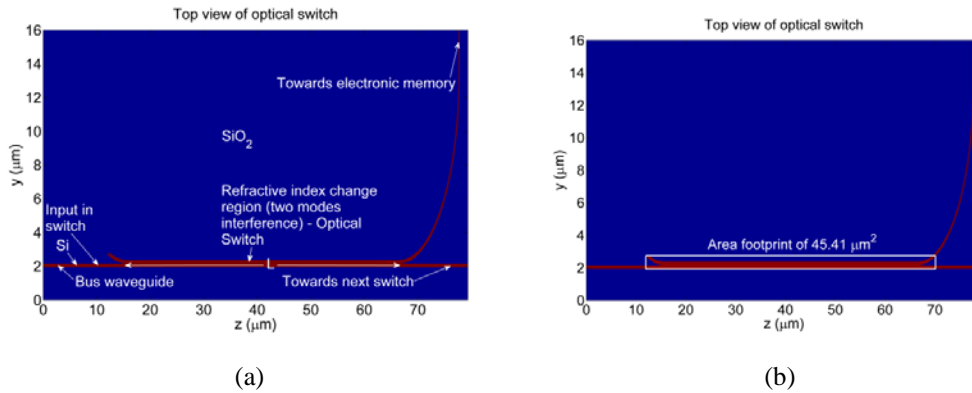
Figure 6.8: (a) Illustration optical switch design (here is in OFF state) for L = 51.26 μm; (b) The same switch design in ON state – free carriers are injected into the refractive index change region and therefore the Si-core refractive index is decreased by 1%; Zoomed-in one mode of the bus waveguide at the input in switch, two interfered modes waveguide of the switch and the beginning of two output waveguides, each with one mode for: (c) CW field distribution in the OFF state; and (d) CW field distribution in the ON state.

(with a width of 220 nm) that goes towards the next switch (and not into the upward curving waveguide that goes towards the memory) [see Figure 6.8(c)].

When the free carriers are injected in the refractive index change region of the optical switch (switch with the same length L is ON), then, the Si refractive index is decreased (Figure 6.8(b)). As a result, propagation constants of the two interfered modes are changed, so a number of light (interfered two modes) back and forth from one side of the waveguide into other is altered; and at the end of the switch, the light mostly goes into the single mode of the waveguide (220 nm width) towards the memory bank (and not into the bus waveguide that goes towards the next switch); this is illustrated in the zoomed-in Figure 6.8(d) with CW field.

In this chapter and Appendix A, all (Si) waveguides for all of the optical switch designs are designed for a wavelength range of 1500 to 1600 nm at room temperature (~300 K). The cladding is SiO_2.

Figure 6.9 is obtained using 1D mode solver (which numerically solves the eigenvalue equation of the field of modes) and it represents field distributions of two modes across the Si waveguide width of 440 nm and a part of the SiO_2-cladding from both sides of this waveguide (across the y-axis) at the central wavelength of 1550 nm, when the switch is OFF.
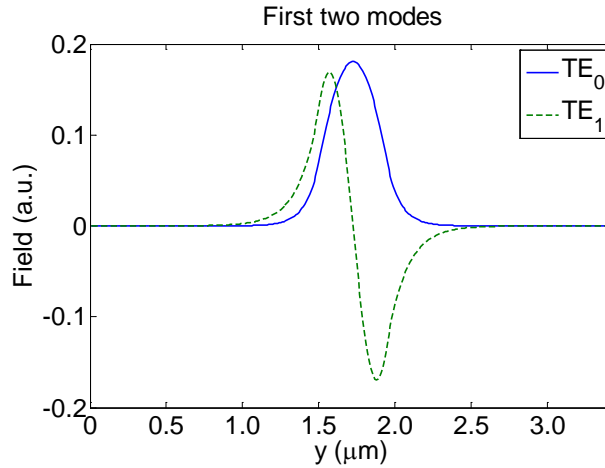
Figure 6.9: Two mode field distributions across the Si waveguide width of 440 nm (refractive index change region) and a part of the SiO$_2$-cladding from both sides of this waveguide (across the y-axis) at the central wavelength of 1550 nm, when the switch is OFF.

In this chapter and in Appendix A, each of our 2D-FDTD simulated switch design structures is as in Figure 6.8(a), but with a different length L. This 2D structure in the top view plane (y, z) is a good approximation for optical switch designs to be modeled using a two-dimensional finite-difference time-domain (2D-FDTD) numerical simulation method [45] instead of a 3D-FDTD. In the case of the switch designs under discussion, the field interactions are basically two-dimensional in the top view (y, z) plane. In addition, if only one mode is confined along the x direction with the proper choice of heights, h$_1$ and h$_2$ [see Figure 6.3(a,c)], then it is a good approximation to use 2D-FDTD in this (y, z) plane for modeling.

Roughly, the refractive index change region is the switch itself. And precisely, the switch also has an arc waveguide at the beginning and at the end.

For each optical switch design, we calculate the area footprint precisely which includes two arcs [see Figure 6.8(b) – it also marks with brighter red color the refractive index change region when the switch is in the ON state]. The area footprint is 45.41 μm^2 for this switch design from Figure 6.8(a,b) which has a L = 51.26 μm. This is our shortest switch design and its features are given in Appendix A.

6.5 Results of switch designs

6.5.1 Optimum optical switch design with refractive index decrease of 1%

In this subsection we present optimum optical switch design with refractive index decrease of 1% in the two mode interference Si waveguide (when switch is ON). The switch is optimum according to the optimum choice of the length L of refractive index change region, which is L = 98.8 μm. Further this length implies optimum in terms of the transmission towards the next switch and towards the memory, area footprint, number of channels, and energy and power consumptions.

The power distribution spectrum is shown in Figure 6.10(a,b) for OFF and ON states of the switch, respectively. This figure represents the fraction of the input power into the switch, for transmitted power towards the memory and for transmitted power towards the next switch. When the switch is in the ON state,

the spectrum is shifted towards smaller wavelengths, to the left (Figure 6.10(b)). This shift is ~10.08 nm for the refractive index decrease of 1% in the two mode Si waveguide. The switch is designed such that it balances two transmissions; the first is towards the next switch in OFF state and the second is towards the memory in ON state, and both are at the central wavelength of 1550 nm (this is for one channel) [see Figure 6.10(a,b)]. This switch can be used either for switching of one full width optical channel, two, or four [see Figure 6.10(a,b)], all around the central wavelength of 1550 nm.

(a)   (b)
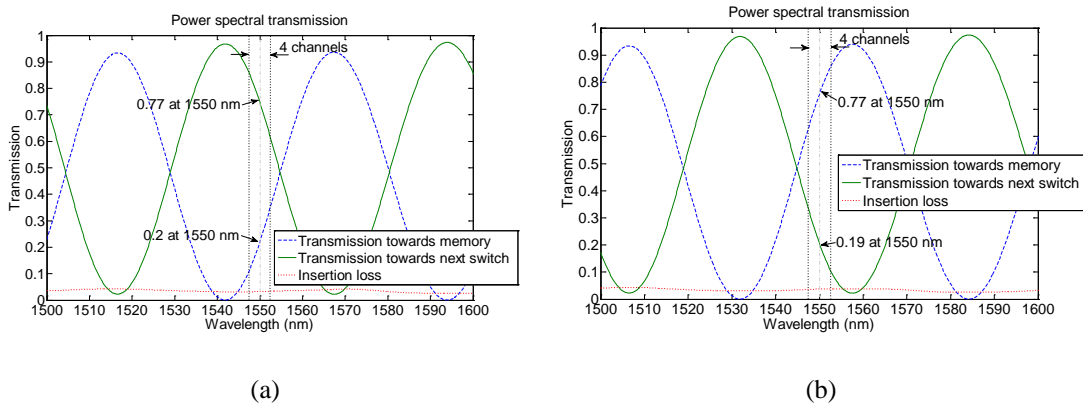
Figure 6.10: Power distribution spectrum for L = 98.8 μm: (a) Switch is OFF; (b) Switch is ON.

Table 6.2 shows the values of transmission for the number of channels N (and correspondent wavelength ranges) when the switch is both OFF and ON. For the number of channels larger than one in correspondent wavelength range, two mentioned transmissions have roughly antisymmetrical values, relative to the vertical line at the central wavelength of 1550 nm [see values in Table 6.2]. This is the case for every switch design in this chapter and Appendix A for the number

of channels larger than one, except for the switch design in the next subsection (4.2).

Table 6.2: Power spectral transmissions per number N of full width channels, for L = 98.8 μm.

	Number N of full width channels	1	2	4
	Wavelength range (nm)	1550	1548.6 – 1551.4	1547.3 – 1552.7
Switch is OFF	Transmission towards next switch (%)	77	83 – 70	88 – 63
	Transmission towards memory (%)	20	14 – 27	9 – 34
Switch is ON	Transmission towards next switch (%)	19	30 – 17	37 – 12
	Transmission towards memory (%)	77	66 – 80	59 – 84

For this switch design, the maximum achieved usable full wavelength bandwidth of four full channel widths is ~5.48 nm, which corresponds to the full frequency bandwidth of 684 GHz (this is given in Table 6.1). Thus, this is a broadband design.

In this chapter and in Appendix A, insertion loss is the optical insertion loss of the optical switch, which is obtained as a remainder of the two previously mentioned transmitted power fractions (or two transmissions). This is without including absorption in Si. In addition, insertion loss is given when the switch is both OFF and ON, and it is roughly flat in the 1500 to 1600 nm range of wavelengths. According to [5], measured propagation loss in Si waveguide with no injected free carriers (switch is OFF) is approximately 3 dB/cm, at a

wavelength of ~1550 nm. In the ON switch state absorption in Si is discussed in section 6.7.

At the central wavelength of 1550 nm, this switch design has insertion loss of 3% when the switch is OFF and of 4% when the switch is ON.

For this switch design area footprint, energy consumption and power consumption are all given in Appendix A in Table A.4. The same Appendix A contains these three magnitudes, then spectral transmissions for the OFF and the ON states for each number N of full width channels and insertion loss at the central wavelength, of the various switch designs with L = (51.26, 159.68, 171.08) μm. All these switch designs, including one from this subsection, have refractive index decrease of 1% and can be electronically controlled with discussed driver circuit [7]. Moreover, all these switch designs, including the driver circuit, are fully within constraints of the existing unmodified 45 nm SOI-CMOS foundry process [5].

In Appendix A among mentioned various designs, the design with L= 171.08 μm has two transmissions over 90% at the central wavelength.

If we choose to use some of the switch designs with more than one switch, as shown in Figure 6.1, for every next switch along the bus waveguide there is decreased value from the previous switch(es). The maximum number of switches depends on the maximum value of light intensity in the input of the first switch. It also depends on the minimum value of light intensity as binary "1", such that

electronic memory can store binary "1" or "0" for each bit, after photodetector [8] opto-electrical conversion.

6.5.2 Optical switch design with 2.9% refractive index decrease in Si-core and SiO$_2$-cladding foundry processes

The switch design in this subsection in the ON state has uniform Si refractive index decrease of 2.9% ($\Delta n = 0.1$). With this refractive index decrease and its length L = 89.02 μm, this switch is different than all other designs in this chapter and Appendix A. At this point, there is no proof that this design can be electronically controlled with the driver circuit [7], which makes it exception relative to all other designs in this chapter and Appendix A. This Si-core refractive index decrease at the 1550 nm is practically feasible to achieve, according to [141], for the free-carrier concentration (electrons and holes) of approximately 10^{20} cm^{-3} [see Figure 6.7].

The switch transmission spectrum is depicted in Figure 6.11. The mentioned length L is chosen such that each spectral transmission (from two of them) is approximately on its maximum value for each switching state, OFF and ON. This switch can be used either for switching of one full width optical channel, two, four, eight, or sixteen [see Figure 6.11(a,b)], all around the central wavelength of 1550 nm. The values of two transmissions for the number of channels N (and the correspondent wavelength range) when the switch is OFF and

ON, are shown in Table 6.3. Here, it can be seen that for any number of channels, in correspondent wavelength range, two transmissions have roughly symmetrical values, in the OFF and the ON switching states, relative to the vertical line at the central wavelength.

(a)   (b)
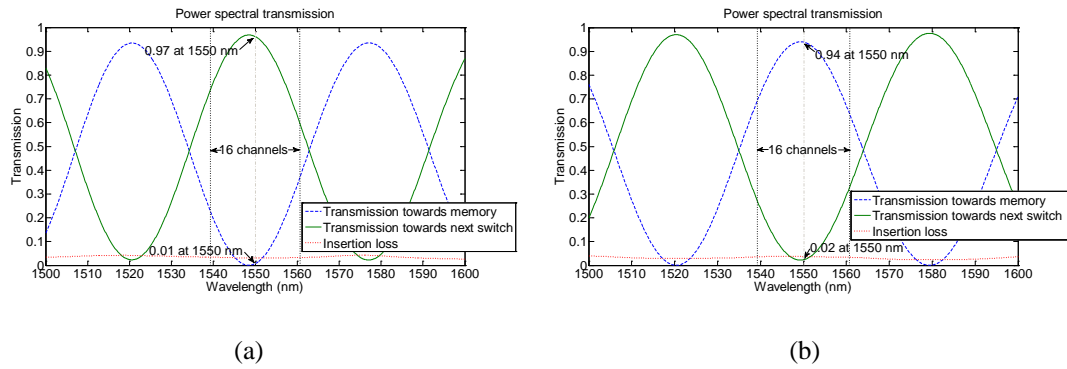
Figure 6.11: Power distribution spectrum for L = 89.02 μm: (a) Switch is OFF; (b) Switch is ON.

Table 6.3: Power spectral transmissions per number N of full width channels, for L = 89.02 μm.

	Number N of full width channels	1	2	4	8	16
	Wavelength range (nm)	1550	1548.6 – 1551.4	1547.3 – 1552.7	1544.5 – 1555.5	1539 – 1561
Switch is OFF	Transmission towards next switch (%)	97	97 – 95	96 – 93	91 – 85	74 – 60
	Transmission towards memory (%)	1	0 – 2	1 – 4	6 – 12	22 – 36
Switch is ON	Transmission towards next switch (%)	2	3 – 3	4 – 4	10 – 11	27 – 32
	Transmission towards memory (%)	94	94 – 93	92 – 92	87 – 86	70 – 65

At the central wavelength of 1550 nm this switch design has insertion loss of 2% when the switch is OFF and of 4% when the switch is ON. In the ON switch state absorption in Si is discussed in section 6.7.

The switch area footprint is 74.86 μm^2.

For this switch, the maximum achieved usable full wavelength bandwidth of sixteen full channel widths is ~22 nm, which corresponds to the full width frequency bandwidth of 2.736 THz (this is given in Table 6.1).

6.6 Analysis of simulated switch designs by using analytical model

By using derived Equations (6.19), (6.20), (6.21), and (6.3) from the subsection 6.2.3, we calculated the values of $\Delta\beta$ for the two different ON states (two different Si refractive index decreases), and also for the OFF state ($\Delta n = 0\%$). These two different Si refractive index decreases Δn (1% and 2.9%) correspond to our switch designs in this chapter and Appendix A. When the switch is in the OFF state there is no Si refractive index decrease so $\Delta n = 0\%$. For analytical calculation we used: $\lambda_o = 1.55$ μm, $w_2 = 0.44$ μm, and $n_2 = 1.44402$, which are all the same values as for our all switch designs. The values of n_1 used in calculations, are obtained based on the refractive index decrease Δn values. These resulting calculated values of $\Delta\beta$ are shown in the Table 6.4 with the correspondent calculated values of k_y (for both modes), β_1 and β_2.

Table 6.4: Values of $\Delta\beta$ for two different ON states (two different refractive index decreases) and also for OFF state ($\Delta n = 0\%$), of switch designs, with correspondent values of k_y (for both modes), β_1 and β_2. All values of k_y, β and $\Delta\beta$ in this table are calculated by using derived analytical model from subsection 6.2.3. In derived analytical model values of λ_o, w_2 and n_2 are as we used them for our all switch designs: $\lambda_o = 1.55$ μm, $w_2 = 0.44$ μm, and $n_2 = 1.44402$. The values of n_1 used in calculations, are obtained based on the refractive index decrease Δn values.

Δn (%)	0	1	2.9
n_1	3.47644	3.44168	3.37644
k_y for TE$_0$ mode (rad/μm)	5.23	5.21	5.18
β_1 (rad/μm)	13.09	12.94	12.67
k_y for TE$_1$ mode (rad/μm)	10.13	10.09	10.0
β_2 (rad/μm)	9.80	9.64	9.35
$\Delta\beta$ (rad/μm)	N/A	0.01	0.03

We obtained the same values (in accuracy of the two decimal places) of all β_1 and β_2 with the 1D mode solver as the values shown in Table 6.4 (by using our analytical model). This confirms the validity of our derived analytical model, and also the validity of 1D mode solver used.

From the Table 6.4 we can notice that as the Si refractive index decrease Δn is larger in the ON state that both values of propagation constants β_1 and β_2 are smaller, so that $\Delta\beta$ is larger. The two mode waveguide width w_2 needs to satisfy requirement that both modes TE$_0$ and TE$_1$ are confined, so it cannot be much smaller. Also, this width cannot be much larger because the third order mode TE$_2$ will not be cutoff anymore and can be excited. We used the safe value of $w_2 = 440$

nm [see the end of subsection 6.2.2] for our all switch designs, in order to analyze them in this chapter and Appendix A.

By using Equation (6.2) and a value of Δβ for Δn=2.9% from Table 6.4, we calculate the phase difference $\Delta\varphi = \frac{\pi}{1.18} \ rad$ for switch design with L= 89.02 μm. For this switch, in Figure 6.12(a,b) are shown CW field distributions for OFF and ON state respectively. From the value of the phase difference $\Delta\varphi = \frac{\pi}{1.18} \ rad$, which is of all our switch designs in this chapter and Appendix A the closest value to $\Delta\varphi = \pi \ rad$, we can see in Figure 6.12 that there is very nearly one more zigzag in ON state than in OFF state. One more zigzag corresponds to the value of phase difference $\Delta\varphi$ which is close or equal to the π rad. This zigzag difference enables switching. Also, we can notice that for this phase difference in Figure 6.12(a) in OFF state almost all optical power goes towards the next switch; and in Figure 6.12(b) in ON state almost all optical power goes towards the electronic memory.

In Figure 6.13 are the 10 zigzags zoomed-in from Figure 6.12(a) in OFF state. Everything shown in Figure 6.13 is obtained from 2D-FDTD simulation. One period of zigzags (two zigzags) for the phase of $\varphi = 2\pi$ correspond to the length of 1.91 μm. 10 zigzags for the phase of $\varphi = 10\pi$ correspond to the length of l = 9.54 μm. By using the Equation (6.22) and β_1 and β_2 values from Table 6.4,
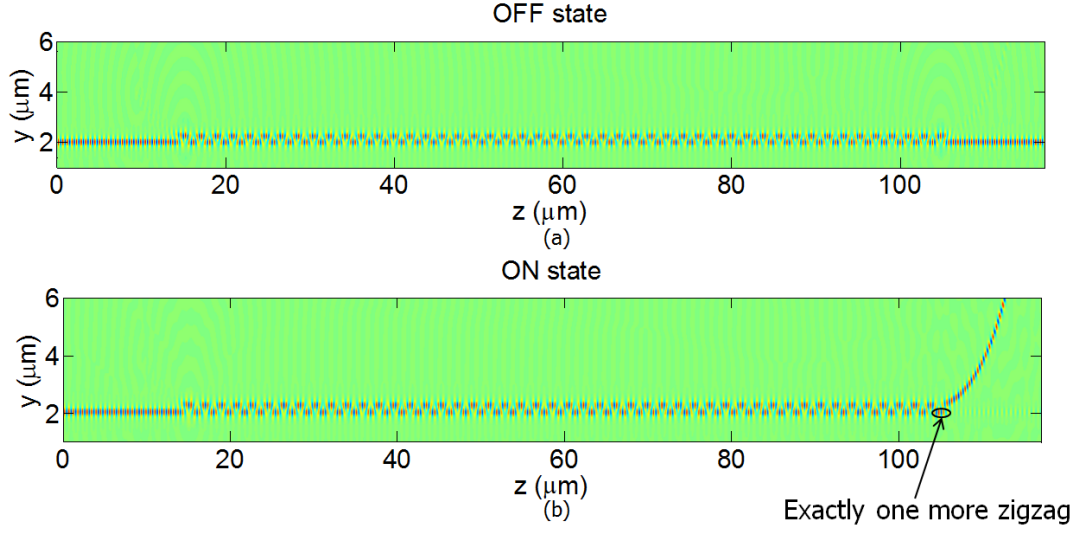
Figure 6.12: CW field distribution of switch design with L = 89.02 μm, refractive index decrease in ON state Δn = 2.9%, and calculated phase difference by using analytical model (Equation (6.2) and value of Δβ from Table 6.4) of $\varphi = \frac{\pi}{1.18}$ rad, which is the closest to $\varphi = \pi$ rad from all our switch designs in this chapter and Appendix A: (a) OFF state; (b) ON state (there is exactly one more zigzag than in OFF state).

we calculate the period of zigzags $P = \frac{2\pi}{(13.09-9.8)_{OFF}} = 1.91$ μm, which is the same as obtained in simulation. Also, by using the Equation (6.23) and $β_1$ and $β_2$ values from Table 6.4, we calculate the number of zigzags for the length of l = 9.54 μm. This number is $N = \frac{(13.09-9.8)_{OFF}\cdot9.54}{\pi} = 9.99 \approx 10$ zigzags, that is approximately the same number of zigzags obtained in the simulation for the same length l. With these two calculations, we again confirmed the validity of our derived analytical model and also the validity of used 2D-FDTD simulations.

144
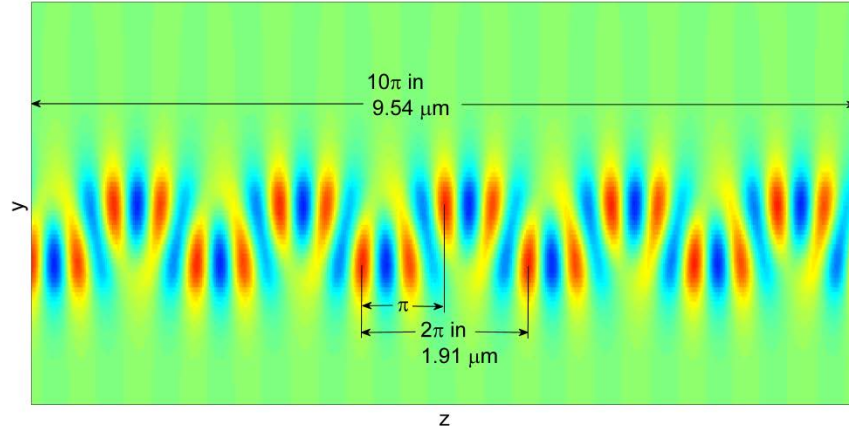
Figure 6.13: Zoomed-in 10 zigzags of 2D-FDTD simulated CW field distribution from Figure 6.12(a) for switch in OFF state. All numbers in this Figure 6.13 are obtained from 2D-FDTD simulation.

From the Equation (6.2) and for the constant phase difference $\Delta\varphi$, as larger is $\Delta\beta$ the switch needs smaller length L for efficient switching between the two output ports. By using Equation (6.2) and values $\Delta\beta$ from Table 6.4, we calculated the phase difference $\Delta\varphi$ values for the different switch designs in this chapter and the Appendix A with different lengths L. These $\Delta\varphi$ values and average transmissions at 1550 nm of two output ports are presented in Table 6.5. Also, in the same table we calculated the two values of L for the phase difference $\Delta\varphi = \pi$ and the two different Si refractive index decreases (each $\Delta\beta$ depends on each of these two), and roughly estimated the two average transmissions at 1550 nm wavelength for the two output ports.

145

Table 6.5: Phase difference $\Delta\varphi$ vs. refractive index change region length L and Si refractive index decrease Δn ($\Delta\beta$ depends on it), and also average transmission at 1550 nm of two output ports.

L (μm)	51.26	98.8	159.68	171.08	314.16	89.02	104.72
Δn (%)	1	1	1	1	1	2.9	2.9
$\Delta\varphi$ (rad)	$\dfrac{\pi}{6.13}$	$\dfrac{\pi}{3.18}$	$\dfrac{\pi}{1.97}$	$\dfrac{\pi}{1.84}$	π	$\dfrac{\pi}{1.18}$	π
Average transmission at 1550 nm of two output ports (%)	64.5	77	87.5	90.2	~96 (rough estimate)	95.5	~96 (rough estimate)

In Table 6.5 and also in fitted curve in Figure 6.14 obtained from this table, we notice that it is not necessary to have $\Delta\varphi = \pi$ for a high transmission to be obtained at both output ports. For the $\Delta\varphi = \pi$, we need a much larger L than for the smaller value than π to obtain close transmissions. For example, for the Si refractive index decrease of 1%, the length L for $\Delta\varphi = \pi$ is somewhat less than 2
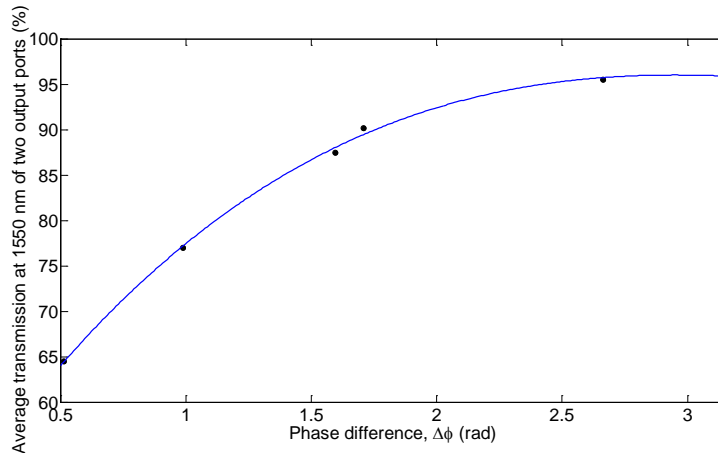
Figure 6.14: Fitted curve on points of average transmission at 1550 nm of two output ports vs. phase difference $\Delta\varphi$, obtained from Table 6.5.

times larger than length L for the $\Delta\varphi = \frac{\pi}{1.84}$; and transmission is roughly for 6%

larger for almost double larger L; however, both transmissions are very high

(>90%) for the both lengths L. This is why we recommend that $\Delta\varphi$ can be smaller

than π and this much decreases L. Our optimum choice of $\Delta\varphi$ is for our optimum

switch design for L = 98.8 μm (previously discussed) and this is $\Delta\varphi = \frac{\pi}{3.18}$. For

this value of $\Delta\varphi$, we plotted in Figure 6.15 the dependence of L on Si refractive

index decrease Δn within L region. This decrease Δn goes from the value 0.7% up

to the value of 2.9% with the step of 0.1%, and it is presented numerically on the

horizontal axis (and not in percentage).
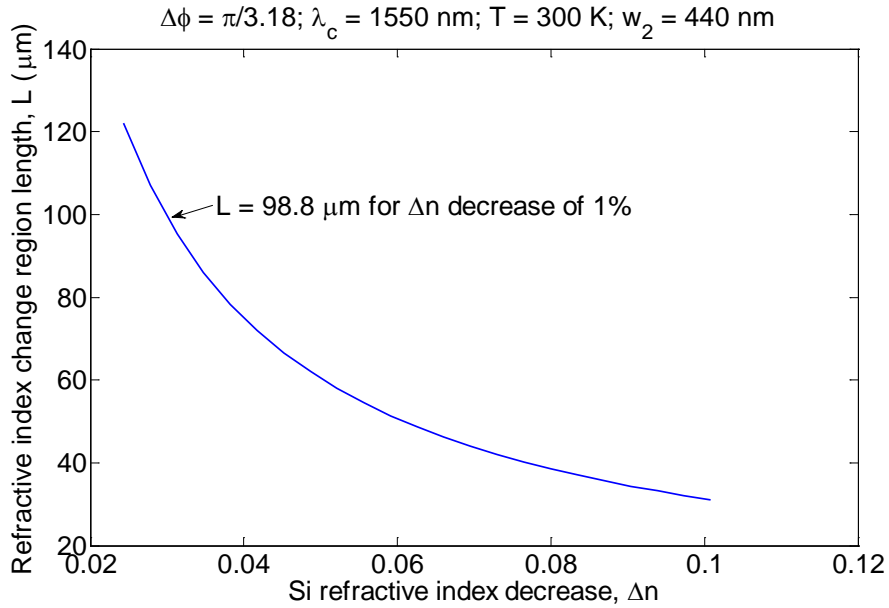
Figure 6.15: Dependence of L on Si refractive index decrease Δn within L, for $\Delta\varphi = \pi/3.18$. Decrease Δn goes from the value 0.7% up to the value of 2.9% with the step of 0.1%, and it is presented numerically on the horizontal axis and not in percentage.

In Figure 6.15, we can see that for this optimum $\Delta\varphi$ value, switch design with length L of ~31 μm can be obtained with efficient transmissions on the both output ports.

6.7 Design patterns

As we ran many 2D-FDTD simulations, we noticed certain patterns based on which desired optical switch can be designed within physics of operation.

The graph of wavelength shift Δλ towards smaller wavelengths vs. refractive index decrease Δn (in the refractive index change region of the switch) for 0.1%, 0.2% and up to 2.9% of the Si-core refractive index of 3.47644 at the 1550 nm, is shown in Figure 6.16. As last decrease of 2.9% is chosen due to the correspondent value of Δn = 0.1, which is the highest value in Figure 6.7 (from [141]) for the free carriers (electrons and holes) concentration of 10^{20} cm^{-3}. Note that the values on the horizontal axis are not given in percentages, but in numerical values of Δn.

From the linear fit of this graph, we obtained equation:

$$\Delta\lambda \approx 290 \, \Delta n \, (nm), \qquad (6.25)$$

which can be used for calculation of wavelength shift $\Delta\lambda$ towards left (smaller wavelengths) in a spectrum based on refractive index decrease value of Δn. In this equation (6.25) unit for constant 290 is in nm such that $\Delta\lambda$ is in nm.
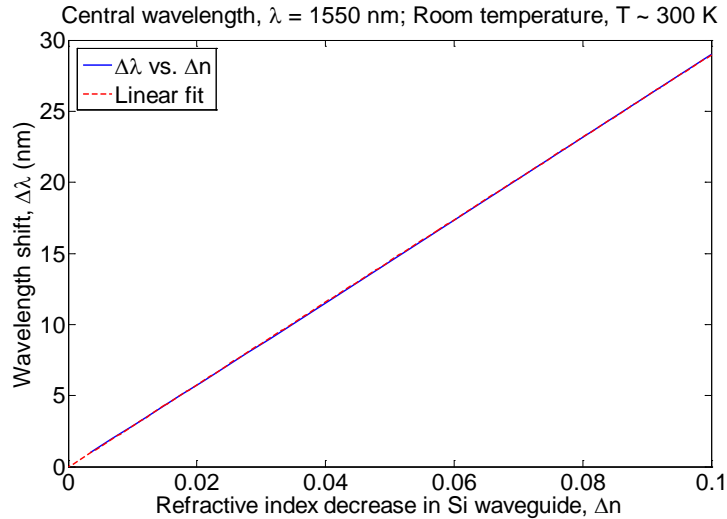
Figure 6.16: 2D-FDTD simulated wavelength shift $\Delta\lambda$ towards smaller wavelengths vs. refractive index decrease Δn for 0.1%, 0.2% and up to 2.9% of Si-core refractive index of 3.47644 at 1550 nm (values on horizontal axis are not given in percentage, but in numerical values of Δn); and its linear fit.

If the refractive index decrease is, for example, of 1% ($\Delta n = 0.03476$) along the whole length L, then the shift of the spectrum will be $\Delta\lambda \approx 290 \cdot 0.03476$ (nm) = 10.08 nm to the left (towards a smaller wavelengths) relative to the spectrum in the OFF state of the switch. This equation holds for a refractive index decrease along the whole L. This value of wavelength shift will be for any length L, only if a refractive index is decreased along the whole length L. For example, if

we decrease the refractive index only in 2/3 of the L the wavelength shift will be 2/3 of Δλ. The previous happens regardless in what order refractive index is decreased along L, for example it can be 1/3 decreased, then 1/3 unchanged, and then 1/3 decreased, or for example it can be 1/3 decreased, then 1/3 decreased, and then 1/3 unchanged.

Figure 6.17 shows the increase of the refractive index change region length L for ΔL vs. wavelength shift Δλ of the spectrum towards a smaller wavelengths (to the left), or decrease of length L for ΔL vs. wavelength shift Δλ of spectrum towards larger wavelengths (to the right). The previous simply means that it works in both directions. It is characterized by the equation (6.26) where Δλ is in nm and then ΔL is in μm. So the constant 0.039 has unit μm/nm, and the constant 0.072 has unit μm.

$$\varDelta L \approx 0.039 \,\varDelta\lambda(nm) + 0.072 \,(\mu m). \qquad (6.26)$$

This equation holds for both states of the switch, ON and OFF. We recommend it to be used for some initial length L. For example, if the initial L = 98 μm and we look the spectrum in the OFF state, and also if design needs to balance the transmission values in the OFF and the ON state, then the spectrum needs to be moved in a certain direction (left or right) for a certain value Δλ. In addition, based on equation (6.25) we can estimate how much it will shift when

150

the refractive index is decreased in ON state. If spectrum needs to be moved to the left for $\Delta\lambda = 23$ nm, and then length L needs to be increased for $\Delta L \approx 0.039$ $23+0.072$ (μm) $= 0.97$ μm. Also, the same values would hold if spectrum needs to be moved to the right for $\Delta\lambda = 23$ nm, and then length L needs to be decreased for $\Delta L \approx 0.97$ μm.
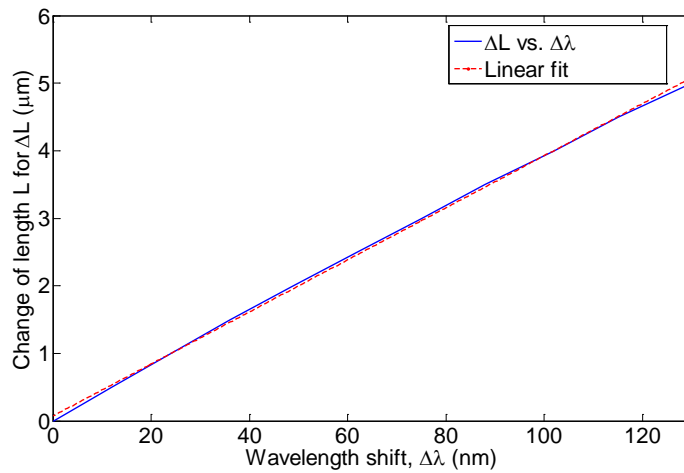
Figure 6.17: 2D-FDTD simulated increase of refractive index change region length L for ΔL vs. wavelength shift $\Delta\lambda$ of spectrum towards smaller wavelengths (to the left), or decrease of length L for ΔL vs. wavelength shift $\Delta\lambda$ of spectrum towards larger wavelengths (to the right); and its linear fit.

In Figure A.3(b) the spectrum eye width Δw is marked in the transmission spectrum. Figure 6.18 depicts the spectrum eye width Δw vs. length of the refractive index change region L; and its 6th degree polynomial fit. Equation (6.27) is obtained for this fit. In this equation, L is in μm and Δw is in nm (these units are appropriately managed by units of constants). There is no significant

difference in this graph and so in the equation, when the switch is OFF or ON. Here, it can be seen that as longer is L it is narrower spectrum eye width Δw. Therefore, the switch transmission spectrum has steeper rising and falling edge. The previous is important in terms of estimating useful bandwidth for a certain number of channels. Also, this can be noticed by comparing the spectrum eye widths in transmission spectrums of the switch designs with different lengths L but the same refractive index decrease of 1%.

$$\Delta w \approx 1.74\ 10^{-10}\ (L(\mu m) - 90.1)^6 - 1.91\ 10^{-8}\ (L - 90.1)^5 - 1.19\ 10^{-7}\ (L - 90.1)^4 + 2.69\ 10^{-5}\ (L - 90.1)^3 + 3.43\ 10^{-3}\ (L - 90.1)^2 - 3.38\ 10^{-1}\ (L - 90.1) + 28\ (nm). \qquad (6.27)$$
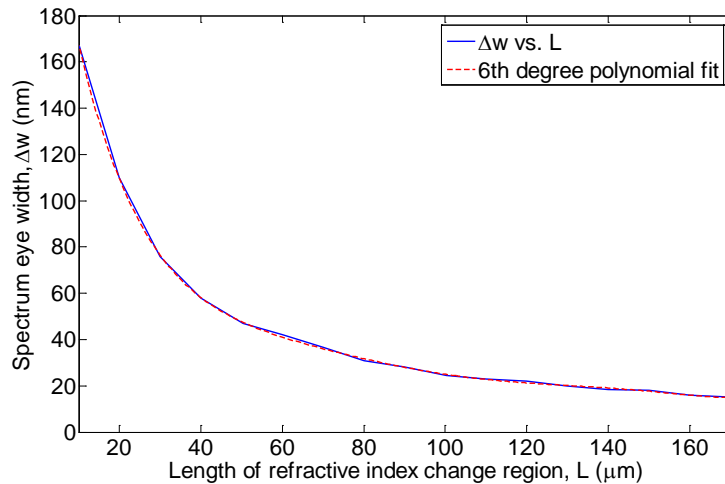
Figure 6.18: 2D-FDTD simulated spectrum eye width Δw vs. length of refractive index change region L; and its 6ᵗʰ degree polynomial fit.

For example, if in equation (6.27), L = 91 (which means 91 μm) then $\Delta w \approx 27.7$ nm.

For reaching the desired switch design, we recommend first to simulate in FDTD initial switch design and so its initial length L, which is close enough to desired design. In addition, the initial values from the switch designs, presented in this chapter and Appendix A, can be used for estimation. Then, use graphs above for a fine tuning of the switch design parameters. Finally, the finest tuning of them perform by repeating the FDTD simulations, which also depends from discretization that you are using.

The desired optical switch can be designed by using the previous equations as fits from graphs and the instructions given about the physics of the switch.

6.8 Absorption in Si due to free-carrier injection

It is known that when free carriers (electrons and holes) are injected in Si there is absorption loss [141]. In Figure 6.19 (a,b) (from [141]) is shown the absorption in Si at λ = 1.55 μm and room temperature as a function of free-electron concentration and free-hole concentration, respectively. From the data in this figure, we can estimate the absorption in the refractive index change region of the switch when the free carriers (electrons and holes) are injected in the ON switching state.
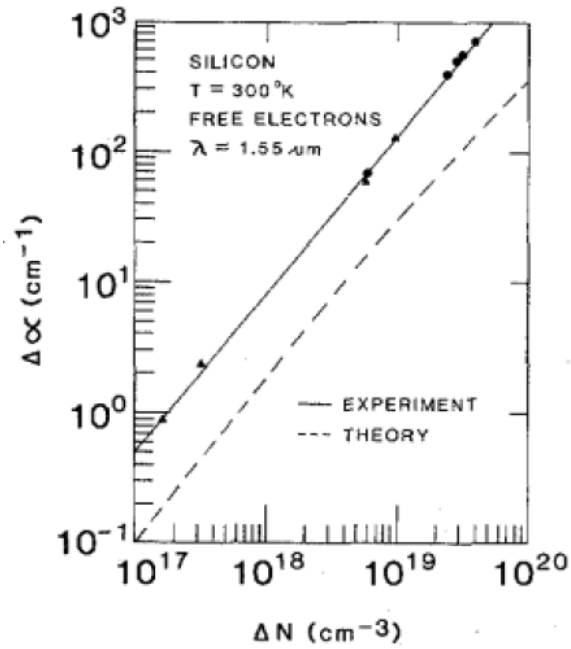
(a)
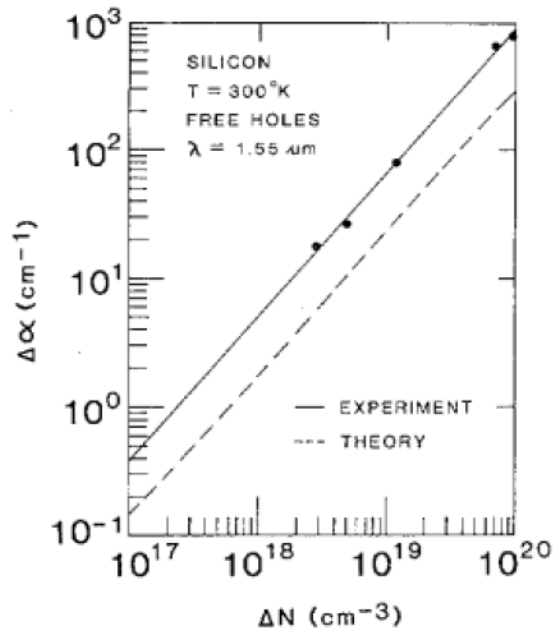
(b)

Figure 6.19: Absorption in Si at $\lambda = 1.55$ μm and room temperature as a function of: (a) free-electron concentration; (b) free-hole concentration. From [141].

To achieve a Si refractive index decrease of 1% an injected free-carrier (electrons and holes) concentration of $\sim 3 \times 10^{19}$ cm^{-3} is needed. The corresponding Si refractive index decrease is $\Delta n \approx 4.8 \times 10^{-3} + 3 \times 10^{-2} = 0.0348$ (in our notation we do not use minus sign) from Figure 6.7. Since

$$\Delta n = \Delta n_e + \Delta n_h, \qquad (6.28)$$

we can split Δn into $\Delta n_e \approx 4.8 \times 10^{-3}$ for the free-electron refractive index decrease, and $\Delta n_h \approx 3 \times 10^{-2}$ for the free-hole refractive index decrease. We choose a corresponding lower free-electron concentration $\Delta N_e \approx 4.3 \times 10^{18}$ cm^{-3} and corresponding higher free-hole concentration $\Delta N_h \approx 2.6 \times 10^{19}$ cm^{-3} (from Figure 6.7) so that in total it remains approximately $\Delta N \approx 3 \times 10^{19}$ cm^{-3}. The reason for the choice on the mentioned way of injected free-carrier concentrations is that the absorption due to injected free electrons in Figure 6.19(a) is larger than the absorption due to injected free holes in Figure 6.19(b). Absorption can be minimized in this way by choosing the refractive index decrease for free-electron Δn_e and free-hole Δn_h to favor the contribution of the free holes.

Consequently, from Figure 6.19(a,b) at the wavelength of 1550 nm and the room temperature and for the mentioned free-electron and free-hole concentrations, the experimentally obtained absorption in Si is approximately $\Delta \alpha_e \approx 40$ cm^{-1} for free electrons and approximately $\Delta \alpha_h \approx 130$ cm^{-1} for free holes. The

experimentally obtained absorption is larger than the theoretically obtained absorption. From the equation

$$\Delta\alpha = \Delta\alpha_e + \Delta\alpha_h, \qquad (6.29)$$

the absorption of injected free carriers (electrons and holes), $\Delta\alpha \approx 170$ cm^{-1} is obtained.

In the same way as above, for a Si refractive index decrease of $\Delta n \approx 2\text{x}10^{-2} + 8\text{x}10^{-2} = 0.1$ (2.9%), from Figure 6.7 we can split it into $\Delta n_e \approx 2\text{x}10^{-2}$ for the free-electron refractive index decrease, and $\Delta n_h \approx 8\text{x}10^{-2}$ for the free-hole refractive index decrease. The corresponding lower free-electron concentration is $\Delta N_e \approx 1.8\text{x}10^{19}$ cm^{-3}, and the corresponding higher free-hole concentration is $\Delta N_h \approx 8.2\text{x}10^{19}$ cm^{-3} (from Figure 6.7), so that the total remains approximately $\Delta N \approx 10^{20}$ cm^{-3}. From Figure 6.19(a,b) at a wavelength of 1550 nm and at room temperature, the experimentally obtained absorption in Si is approximately $\Delta\alpha_e \approx 200$ cm^{-1} for free electrons and approximately $\Delta\alpha_h \approx 600$ cm^{-1} for free holes. Therefore, the incremental absorption of injected free carriers (electrons and holes) is $\Delta\alpha \approx 800$ cm^{-1}. In this case (when the switch is ON), we note that absorption is few times higher than in the case of Si refractive index decrease of 1%.

The fraction of the transmitted optical power due to absorption through the switch in ON switching state expressed in percentage we calculated as

$$f_{tr,P} = 100 \, e^{-\Delta\alpha L} \, (\%), \qquad (6.30)$$

and the results are shown in Table 6.6 for various switch designs.

Table 6.6: The fraction of transmitted optical power due to absorption through switch in ON switching state $f_{tr,P}$ expressed in percentage versus refractive index change region length L, and absorption $\Delta\alpha$ (which depends on Δn).

L (μm)	51.26	98.8	159.68	171.08	314.16	89.02	104.72
Δn (%)	1	1	1	1	1	2.9	2.9
$\Delta\alpha$ (cm^{-1})	170	170	170	170	170	800	800
$f_{tr,P}$ (%)	41.84	18.64	6.62	5.46	0.48	$8.1 \cdot 10^{-2}$	$2.3 \cdot 10^{-2}$

All of the switch designs from Table 6.6 were useful in this study, and the results obtained in this chapter are helpful for engineering of our novel switch. However, the simulated designs (not including the two estimated for the phase difference $\Delta\varphi = \pi$ from section 6.6) do not work as initially conceived (due to carrier photoabsorption) for all channels around the central wavelength of 1550 nm with a fixed electronic memory threshold. This is because the transmitted optical power to the output port in the direction of the electronic memory in the ON state is lower (due to absorption) than the leaked (undesired) transmitted optical power towards the electronic memory in the OFF state. But, the simulated

switch designs with L = [159.68, 171.08, 89.02] μm for some channels in the range around the central wavelength of 1550 nm when their transmitted power towards the electronic memory is approximately 0% in the OFF state, could work with a fixed memory threshold. Also, all of simulated switch designs with lengths L = [51.26, 98.8, 159.68, 171.08, 89.02] μm can work if the electronic memory, after the photodetector opto-electrical conversion, has an adjustable threshold for determination of binary ones and zeros. This means that this adjustable threshold should be above the leaked (undesired) power towards the electronic memory in the OFF state, and then to be lowered down appropriately relative to the switch design absorption in the ON state. The previous could be accomplished because the whole electro-optical system in the future electro-optical computer is synchronized. Therefore, since the optical binary signals are proportionally decreased due to absorption, if the threshold of the electronic memory is correspondently decreased when the electrical signals from converted light in the ON switch state reaches it, then these signals can be detected in electronic memory.

However, let us consider the worst case scenario from Table 6.6 for the $f_{tr,P} = 2.3 \cdot 10^{-2}$ %. If the input power in the switch is 1 mW, the output power in the ON state is $1 \cdot 10^{-3} \cdot 0.96 \cdot 2.3 \cdot 10^{-4} = 0.22$ μW. This power can be detected. This switch design at the central wavelength of 1550 nm has estimated 96% of transmitted power towards the electronic memory in the ON state, and

approximately 0% of the transmitted power towards the electronic memory in the OFF state, due to phase difference of $\Delta\varphi = \pi$. So this switch with the length of L = 104.72 μm, and on the same way the switch with the length L = 314.16 μm, which also has the same phase difference, are both fully operational with no adjustable electronic memory threshold (as long as the leaked power in the OFF state is sufficiently smaller than the power after the absorption in the ON state). Therefore, the switch with any feasible refractive index decrease has the potential to be fully operational when the phase difference is $\Delta\varphi = \pi$ with no adjustable electronic memory threshold.

Also, a switch with an appropriate phase difference smaller than π can also be fully operational if designed such that two output ports are not balanced in terms of transmission. This can be done by designing the switch so that it has maximum power transmission towards the next switch, but approximately 0% power transmission towards the electronic memory, in the OFF state. All that is needed then is to arrange for a Si refractive index decrease such that the transmission towards the electronic memory is sufficiently above approximately 0% in the ON state with the included absorption. Alternatively, we could just use a wavelength close to the 1550 nm with features of the output ports as above in the simulated switches already designed. These approaches cannot be applied to the switch designs with lengths L = [51.26, 98.8] μm because they have insufficient refractive index decrease to shift the spectrum enough to the left in

the ON state; so the power transmitted towards the electronic memory is larger than the transmitted power towards the next switch. But, for example, if for the switch with L = 159.68 μm we choose the central wavelength of 1546 nm in Figure A.2 in Appendix A, this will cause that, in the OFF state, the switch has approximately 0% transmitted power towards the electronic memory and 97% the transmitted power towards the next switch. Also, it is calculated in the previous section by using Equation (6.25) that the wavelength shift $\Delta\lambda \approx 10.08$ nm for the Si refractive index decrease of 1% in the ON state. Thus, in this case the switch will have the transmission towards the electronic memory of 71% and the transmission towards the next switch of 26% with no absorption (in the ON state). With the absorption, towards the electronic memory the transmitted power is 0.71 · 0.0662 = 0.047, which is 4.7%, sufficient to be detected in electronic memory after opto-electrical conversion by photodetector. The other way is to slightly redesign this switch so it can be operational for the central wavelength of 1550 nm instead of 1546 nm. The needed wavelength shift to the right (in the OFF state) is $\Delta\lambda \approx 4$ nm so that based on the Equation (6.26) the switch length of L = 159.68 μm needs to be decreased for $\Delta L \approx 0.039 \cdot 4 + 0.072$ (μm) ≈ 0.23 μm and this results in a new L = 159.45 μm. The transmitted powers on both output ports in both switching states will be approximately the same as previous. Also, the area footprint is slightly smaller, and the switching time and the (electrical) energy consumption, both remain unchanged. The same analogy (one from the

two previous) can be applied for the simulated switch designs with L = [171.08, 89.02] μm.

Consequently, there are ways how all of the switches can be fully operational with small area footprint, and also small switching time and (electrical) energy consumption; although at this point these switches have a significant absorption loss and so low optical energy efficiency in the ON switching state.

Based on derived analytical model for a switch in subsection 6.2.3, we can also approximately design a new switch around the central wavelength of 1550 nm with a low concentration of injected free carriers (and corresponding small Si refractive index decrease), and hence with a low absorption. In this design, all parameters remain the same as in other designs from this chapter and Appendix A, except the length L and refractive index decrease Δn (everything else that follows from these is different as well). For this design, we choose a free-electron concentration of $\Delta N_e \approx 4 \times 10^{17}$ cm^{-3} and the higher free-hole concentration of ΔN_h $\approx 3 \times 10^{18}$ cm^{-3}, so that the total injected free carriers (electrons and holes) concentration is $\Delta N \approx 3.4 \times 10^{18}$ cm^{-3}. In addition, the advantage of choosing the concentrations below 4×10^{19} cm^{-3} from Figure 6.7 is that the free-hole refractive index decrease is larger than the free-electron refractive index decrease. Also, as we mentioned earlier, the absorption of free holes is smaller than the absorption of free electrons. For the last chosen two concentrations from Figure 6.7 we obtain,

$\Delta n_e \approx 4 \times 10^{-4}$ for the free-electron refractive index decrease, and $\Delta n_h \approx 6 \times 10^{-3}$ for the free-hole refractive index decrease, so that $\Delta n \approx 6.4 \times 10^{-3}$. For this switch design the propagation constants in the OFF and in the ON state are: $\beta_{1,ON} = 13.0603$ rad/μm, $\beta_{2,ON} = 9.7682$ rad/μm, $\beta_{1,OFF} = 13.0871$ rad/μm, and $\beta_{2,OFF} = 9.7972$ rad/μm; so that from Equation (6.3) $\Delta\beta = 0.0022$ rad/μm. In the OFF state the propagation constants are the same as in the previous designs, only here we are using them in four decimal places and not in two, because of the need of high precision in the calculation of $\Delta\beta$ (due to its very small value) for the small value of refractive index decrease in the ON state. By using Equation (6.2) for $\Delta\varphi = \pi/1.84$ we calculate a length $L = (\pi/1.84) / 0.0022 = 776.09$ μm. For this length according to Table 6.5 and Figure 6.14, the transmitted power is approximately balanced on both output ports, and it is for the both output ports approximately 90.2%. The transmissions (in the absence of absorption) are approximately the same as in Figure A.3 in Appendix A.

From Figure 6.19 the experimentally obtained absorption in Si is approximately $\Delta\alpha_e \approx 2$ cm^{-1} for free electrons, and $\Delta\alpha_h \approx 14$ cm^{-1} for free holes; so the total absorption of injected free carriers (electrons and holes) obtained is $\Delta\alpha \approx 16$ cm^{-1}. By using the Equation (6.30) we calculate the fraction of the transmitted optical power due to absorption through the switch in the ON switching state expressed in percentage, which is $f_{tr,P} = 28.9\%$. In the ON state the transmitted power towards the electronic memory with no absorption is 90.2% and with the

absorption is $0.902 \cdot 0.289 = 0.26$, which is in percentage 26.1%. This resulting power is larger than the leaked (undesired) power in the OFF state towards the electronic memory, which is 6.6% [see Figure A.3 in Appendix A]. All mentioned transmitted powers for this switch design are at the central wavelength of 1550 nm. With this very long switch design due to the choice of the small refractive index decrease Δn and the large phase difference $\Delta \varphi$, our goal was to show that design of our switch with the balanced two output ports (without absorption) at the central wavelength of 1550 nm can be accomplished and used in the presence of free-carrier absorption. This switch design can be driven with the applied driver circuit [7] with free-carrier injection for switching purposes in this chapter.

This last design has an area footprint of 610.78 μm^2, a switching time of roughly 400 ps (as for other designs), and energy consumption per one switching of 9.66 pJ. With these three, even this very long switch design has many times smaller area footprint and switching time, and also smaller energy consumption than the cited (in introduction section 6.1) switch based on MZI [139], which also operates based on free-carrier injection (so it also has absorption losses).

It is not necessary to design such a large switch as the last one because simply the approaches discussed above can be used for the design of a much smaller operational switch.

In this section, besides other switch parameters and their tradeoffs, we showed that there is important tradeoff with the absorption due to free carriers injection in the ON switching state.

6.9 Conclusions

In this chapter and Appendix A, a novel two mode interference optical switch designs – electronically controlled with the free-carrier injection are presented and studied. This study is accomplished first through the optical switch designs with the Si refractive index decrease of 1% in the ON state. These designs are within the constraints of the fabricated driver circuit, which is applied in this chapter for switching, although it is published for the ring resonator modulator. These designs and the driver circuit are both within the constraints of the existing unmodified 45 nm SOI-CMOS foundry process. And second, through the optical switch design with the Si refractive index decrease of 2.9% in the ON state, which is practically feasible to achieve in Si-core and SiO_2-cladding processes.

Roughly, the refractive index change region is the optical switch itself.

It is shown that our all simulated switch designs have (three switch criteria) hundreds of times smaller area footprint, they are several times faster and also several times more energy efficient than any switch based on traditionally used MZI. Moreover, our designs are broadband with an order of magnitude band similar to MZIs at FWHM (full width at half maximum), with no additional

devices to increase their bandwidth. Since our switch designs are analyzed in this chapter and Appendix A with the full width of the optical channel, which is larger than at FWHM, this means that our switch designs can support even more channels within an FWHM bandwidth than the number of channels reported in this chapter and Appendix A.

We derived the analytical model for our switch design from the Maxwell's equations and showed that it is valid in accuracy of two decimal places in comparison with 1D mode solver. In addition, we again confirmed the validity of the analytical model by also comparing with 2D-FDTD simulation in terms of the period of zigzags and the number of zigzags. These comparisons confirmed vice versa validity as well, which are of 1D mode solver and 2D-FDTD simulator. Also, we found that the refractive index change region length L~31 μm can be achieved with the efficient transmissions on the two output ports (without including the absorption) for the optimum choice of phase difference Δφ between the ON and the OFF states of the switch. This optimum choice of phase difference Δφ is not necessary to be π, but it can be smaller, which decreases length L significantly, and still high transmissions at both output ports can be obtained (without including the absorption).

We considered the impact of absorption when free carriers are injected in the ON switching state. The reduced optical power towards the electronic memory is addressed when the switch is in the ON state. Also, we proposed several

approaches how to deal with the absorption loss and to still have preserved all three mentioned switch criteria of our simulated switch designs. Hence, these three criteria remained more efficient (as mentioned) than these three in the recently published switch based on the MZI with the free-carrier injection and so absorption loss as well. Like any other electro-optical device with free-carrier injection, as MZI modulators, switches, ring modulators and so on, our switch in the same way has a tradeoff with the absorption when the free carriers are injected (in the ON state). Based on derived analytical model for our switch, we approximately designed the switch around the central wavelength of 1550 nm with the phase difference $\Delta\varphi = \pi/1.84$, with a low concentration of injected free carriers (and corresponding small Si refractive index decrease), and hence with a low absorption. This switch design has the transmitted power with the included absorption towards the electronic memory in the ON state of 26.1%, which is several times larger than the leaked (undesired) power towards the electronic memory in the OFF state, which is 6.6%. In addition, this switch design has many times smaller area footprint, several times smaller switching time, and also smaller energy consumption, than the recently published switch based on the MZI, which has absorption loss as well.

The MZI has optical bending losses at the locations of 12 waveguide arcs, through which light propagates in the ON and the OFF switching state; while our switch design has only one bending loss at the location of the one (output) arc

waveguide when the light propagates towards the electronic memory in the ON state. In the OFF state, there is no bending loss because the light propagates straight along the bus. Therefore, here there are less optical power losses in the geometry of our switch design than the geometry of the MZI.

Future work can be about increasing the bandwidth that contains very high transmissions (above 90%) without including the absorption for all multiple channels of our switch design, and also about discovering a more efficient way(s) how to cancel or decrease the absorption loss further. A designer needs to keep in mind that as the bandwidth becomes larger, it may require (but not necessary) higher refractive index decrease (higher concentration of injected free carriers and so higher absorption in Si) so higher voltage, then higher energy consumption and possibly higher power consumption; such that wide bandwidth in the spectrum is shifted enough for the switching in ON state. Hence, mentioned tradeoffs need to be overcome or found, depending on the purpose of the switch design.

We showed that our switch designs are convenient to be usable in the future electro-optical computers. They all have low optical insertion loss (equal or less than 4%), and among which some achieved transmissions over 90% (without including the absorption). Also, we provided guidance as to how to design a desired optical switch with the free-carrier injection.

Besides applications in switching the light signals from one waveguide into other, our optical switch structure can have applications as modulator, filter and other applications in itself.

Chapter 7

_____

Conclusions

_____

In this Ph.D. thesis many novel advances are described, including: various optical grating couplers; an algorithm for the 3D simulation of optical devices from contour files; the proposed electronically-controlled optical switch; a proposed measurement method for current through the heater on an electro-optical chip; a symmetric method for heating the chip to a desired temperature; and an algorithm for the measurement of off-normal angles of the input and the output fibers for fiber-to-chip coupling.

The optical coupling of fiber-to-chip and chip-to-chip through grating couplers is of fundamental importance for energy efficiency of the future electro-optical computers. This is because the light is brought on the chips through these gratings. Chip-to-chip communication via the (wireless) focusing of light can be accomplished through focusing grating couplers in a 3D stacking of the chips. In addition, there are influences of each device on a chip on energy efficiency because all devices work together in the electro-optical system. Unidirectional gratings were designed, and after fabrication compared experimentally with

(typical) bidirectional gratings. The experimental comparison is performed by using a new method of comparison of symmetrical structures, each with the same kind of the gratings. This method can be used for the comparison of appropriate symmetrical structures generally. The optical grating algorithms enable the design of optical grating couplers with desired (and arbitrary) output field parameters which can be given as input in these algorithms.

The novel fully automatic algorithm is presented which from the contour file, after optical proximity correction, extracts coordinates and builds any 3D optical device which can be further simulated in 3D-FDTD. The purpose of this is to compare such a simulated device with the designed device before the fabrication occurs, so that modification of the designed device can be performed if needed.

It is shown that our novel electronically-controlled optical switch has hundreds of times smaller area footprint, it is several times faster and also several times more energy efficient, than the switch based on the traditionally used Mach-Zehnder Interferometer (MZI). Our switch design can use multiple channels (multiple wavelengths), centered around the central wavelength, which means that it is broadband. The bandwidths of our switches are of the same order of magnitude as typical broadband MZI designs with free-carrier injection and no additional device for increase of bandwidth. In our switch designs, we do not use any additional device to increase the bandwidth. Our switch designs are the first

to make use of two TE mode interference in Si-core and SiO$_2$-cladding for switching purposes, and also the first in using free-carrier injection with two TE mode interference, again for switching purposes.

Three different measurement methods can enable different kinds of measurements in understanding and engineering of devices during the development of the future electro-optical chips and so the future electro-optical computers. The first method is for measurement of the electrical current through the heater (resistor), which means that some devices on the chip can be thermally controlled. Also, this method can be used for the simplification of commonly used forward and reverse biased diodes in complex circuit topologies with many of these diodes. The second (symmetry) method can provide for measurements or confirmation of the desired temperature on the chip. This is suitable for tests of devices that are exposed to heat variations on the chip while electro-optical computers operate. This method can find applications in any appropriate symmetrical structure. It is appropriate in terms of the corresponding values of temperature from the two external heaters and dimensions of that structure, such that it provides a uniform temperature in each line parallel with the heaters across the structure. The third method (algorithm) is for the automated measurement of the angles of input and output optical fibers, when they are vertically coupled with the chip, for lab testing of devices on the chip. This algorithm can also be used for

the automated adjustment of desired angles of the input and output optical fibers. All three methods are confirmed experimentally.

The results presented in this thesis allow for improved design of optical grating couplers, a new optical switch, and algorithms (methods) which contribute towards the technology of (future) electro-optical computers, and to this other applications as well. The goal is to develop electro-optical computers with high processing speeds and high energy efficiency, which chips and devices based on fabrication in the existing unmodified CMOS processes. These processes were developed initially for the fabrications of circuits only; however people have found ways to use them for the fabrication of the optical components as well.

The technology of computers, and also in general the electrical engineering, is heading in the direction of smaller, faster, and more energy efficient (less energy consumption) devices. These three criteria for the direction of the mentioned technology, at this point, are the same three mentioned criteria which people have addressed in the literature for the new electronically-controlled optical switch, the design of which is presented in this thesis. This means that in terms of the three criteria, the switch itself is a small part of a big picture, or in other words, the switch three criteria present the direction of the total technology in the electrical and computer engineering, which corresponds to a big picture, and vice versa.

Appendix A

_____

Various optical switch designs with refractive index decrease of 1%

_____

In this appendix, various switch designs are presented, and all can be driven with the existing driver circuit for the free-carrier injection in the horizontal junction [7]. All these switch designs with the driver circuit [7] are within the constraints of the existing unmodified 45 nm SOI-CMOS foundry process [5]. Also, these switch designs can be applied in any Si-core and SiO_2-cladding foundry process with the mentioned driver circuit or appropriate one which can inject the free-carrier concentrations of electrons and holes of $\sim 3 \times 10^{19}$ cm^{-3}, such that, it decreases Si-core refractive index for 1%.

For each of the following switch designs with the different lengths L, its energy and power consumptions, and also area footprint, vs. L are given in Table A.4.

Figure A.1(a,b) shows the transmission spectrum at the 1550 nm in the OFF and the ON state of the switch with the length of L = 51.26 μm, respectively. This switch can be used for either one or two full width channels, all around the central wavelength of 1550 nm. The values of two transmissions per number of channels N (and correspondent wavelength range) when switch is OFF and ON, are given in Table A.1. In the OFF state, the switch insertion loss is 3%, while, in the ON state, its insertion loss is 4%.

(a)   (b)

Figure A.1: Power distribution spectrum for L = 51.26 μm: (a) Switch is OFF; (b) Switch is ON.

Table A.1: Power spectral transmissions per number N of full width channels, for L = 51.26 μm.

	Number N of full width channels	1	2
	Wavelength range (nm)	1550	1548.6 – 1551.4
Switch is OFF	Transmission towards next switch (%)	64	68 – 59
	Transmission towards memory (%)	33	29 – 37
Switch is ON	Transmission towards next switch (%)	31	36 – 28
	Transmission towards memory (%)	65	60 – 68

Figure A.2(a,b) shows the transmission spectrum at the 1550 nm in the OFF and the ON state of the switch with the length of L = 159.68 μm, respectively. This switch can be used for either one, two, or four full width channels, all around the central wavelength of the 1550 nm. The values of two transmissions for the number of channels N (and correspondent wavelength range) when the switch is OFF and ON, are given in Table A.2. In the OFF and the ON state, the switch insertion loss is ~4%.

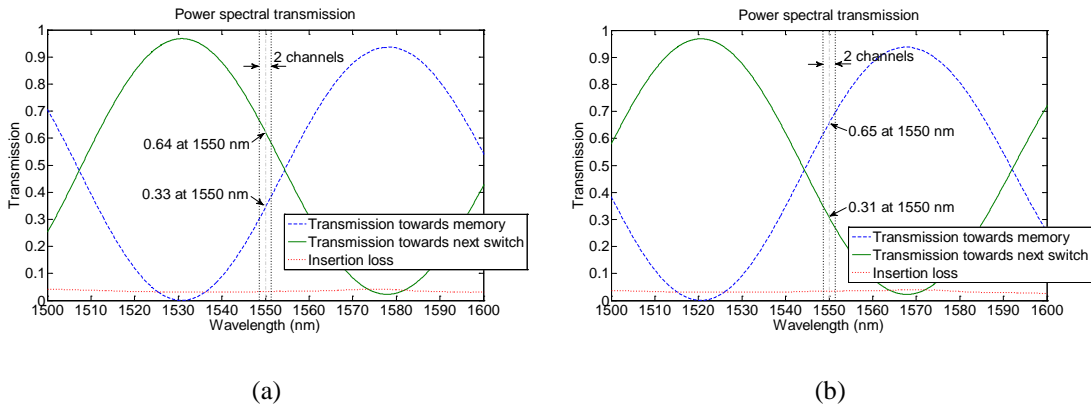**Figure A.2:** Power distribution spectrum for L = 159.68 μm: (a) Switch is OFF; (b) Switch is ON.

Table A.2: Power spectral transmissions per number N of full width channels, for L = 159.68 μm.

	Number N of full width channels	1	2	4
	Wavelength range (nm)	1550	1548.6 – 1551.4	1547.3 – 1552.7
Switch is OFF	Transmission towards next switch (%)	87	94 – 78	96 – 68
Switch is OFF	Transmission towards memory (%)	9	3 – 18	0 – 29
Switch is ON	Transmission towards next switch (%)	8	19 – 5	29 – 2
Switch is ON	Transmission towards memory (%)	88	77 – 91	67 – 94

Figure A.3(a,b) shows the transmission spectrum at the 1550 nm in the OFF and the ON state of the switch with the length of L = 171.08 μm, respectively. This design has transmissions over 90% at the central wavelength when the switch is in the OFF and the ON state. This switch can be used for either one, two, or four full width channels, all around the central wavelength of 1550 nm. The values of two transmissions for the number of channels N (and correspondent wavelength range) when the switch is OFF and ON, are given in Table A.3. In the OFF state, the switch insertion loss is 3.3%, while, in the ON state its insertion loss is 3.7%.
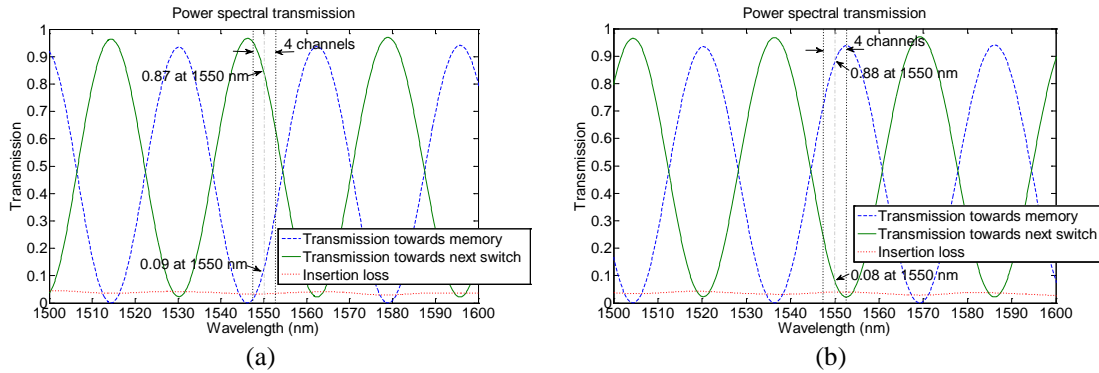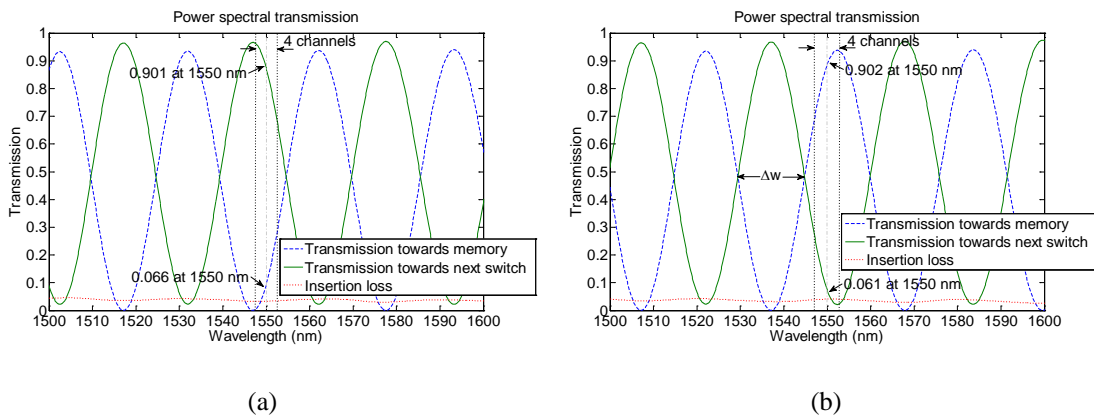

Figure A.3: Power distribution spectrum for L = 171.08 μm: (a) Switch is OFF; (b) Switch is ON.

Table A.3: Power spectral transmissions per number N of full width channels, for L = 171.08 μm.

	Number N of full width channels	1	2	4
	Wavelength range (nm)	1550	1548.6 – 1551.4	1547.3 – 1552.7
Switch is OFF	Transmission towards next switch (%)	90.1	95 – 81	97 – 71
	Transmission towards memory (%)	6.6	1 – 15	0 – 26
Switch is ON	Transmission towards next switch (%)	6.1	19 – 4	29 – 2
	Transmission towards memory (%)	90.2	77 – 92	67 – 94

Table A.4: Energy consumption per one switching, power consumption and area footprint, vs. L. All these switch designs for different L have refractive index decrease of 1% of two mode interference Si waveguide.

L (μm)	51.26	98.8	159.68	171.08
Energy consumption (pJ)	0.64	1.23	1.99	2.13
Power consumption (mW)	1.6	3.08	4.97	5.33
Area footprint (μm^2)	45.41	82.49	129.98	138.87

Appendix B

_____

Measurement methods

_____

B.1 Introduction

In a new environment on the electro-optical chip in the package connected to the chip board [see Figure 2.6(b)] new methods for measuring electrical, electro-optical and optical device performances are needed. These methods also can find applications elsewhere besides this project. In this appendix we present novel three methods of measuring, which are experimentally tested. The first method in the section B.2 is a novel measurement method of current through heater on electro-optical chip. The second method in the section B.3 is a novel symmetry method of heating the chip on the desired temperature. And the third method in the section B.4 is an algorithm for measuring (off-normal) angles of input and output optical fibers.

B.2 Novel measurement method of current through heater on electro-optical chip

B.2.1 Description of method

Figure B.1 depicts part of the circuits on the electro-optical chip with the connected external elements. The problem has been how to measure changes of the heater resistance R (heater is a resistor R) with values of out of the chip DAC (digital analog convertor) direct current I_{DAC} in a range from 0+ to 20 mA. In order to measure resistance, we should measure the heater voltage and the current. Voltage was easy to measure between for example chosen PADs P_36 (PHASE _36) and P_L_C (PHASE_LEFT_COMMON) [measured heater resistance is between these two PADs], but current has been a problem because of the complex structure of the diodes. These diodes produce many current leakages so heater current in this topology could not be measured without canceling these diodes. Simple solution is proposed for this problem, and it is proved theoretically and experimentally.

The heater R can be adjacent to the ring resonator [see Figure 2.1], such that when the DAC current I_{DAC} is increased, the resistance R is increased, the heater power dissipation is increased and so the temperature is raised. Consequently, the refractive index of the ring waveguide is decreased, and the spectrum of the ring resonator, which is the Notch transfer function, is shifted to

the left (towards smaller wavelengths). This is how the ring can be thermally controlled either to pass or to stop its resonant wavelength. This heater can also be used as a corrector of fabrication errors for devices that tightly depend on the phase of the propagating field through the waveguide, for example, electro-optical modulator [144].
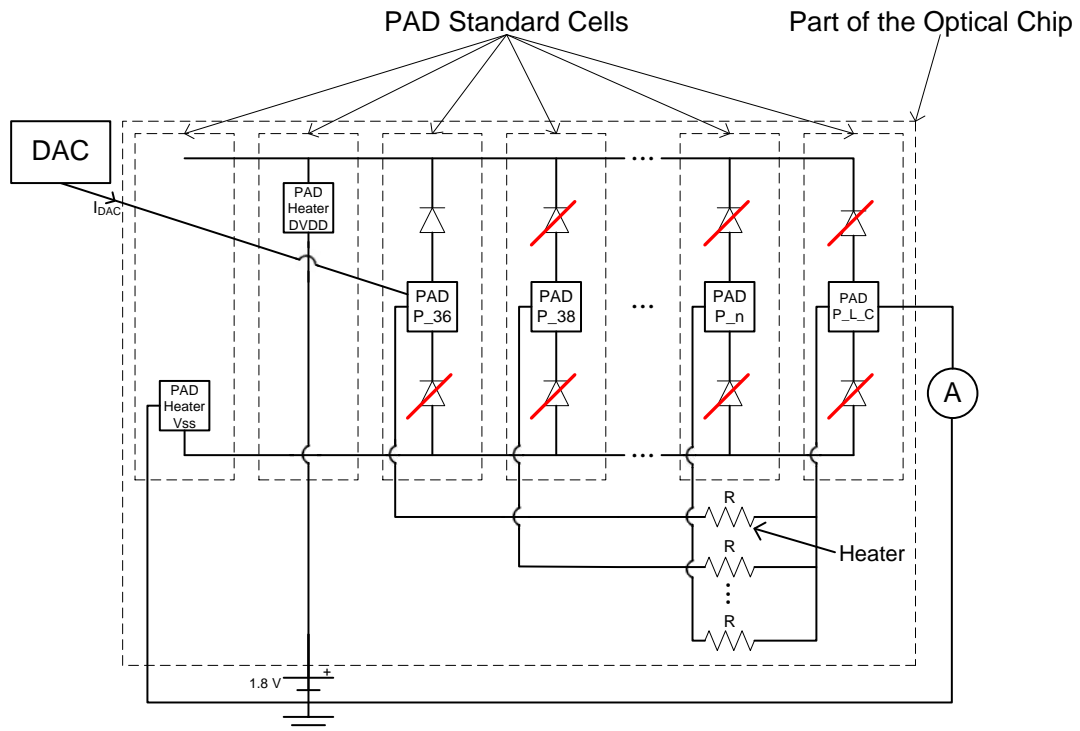

Figure B.1: Scheme of part of the circuits on the electro-optical chip with connected external elements.

Part of these circuits contains PAD Standard Cells, which are within rectangles with dashed lines [follow Figure B.1]. Inside of them are PADs that are metal parts hooked up with wires for external connections (out of the chip). Moreover, forward and reverse bias ESD (electrostatic discharge) diodes are for overvoltage protection of the circuits inside the PADs. External voltage supply with 1.8 V is connected between the PAD HeaterDVDD and the ground.

These circuits in Figure B.1 are designed by Jonathan Leu and Jason Orcutt.

When the P_L_C is connected to the ground, all diodes are canceled; only the diode above P_36 is an exception because I_{DAC} is pumped through the P_36. Now the leakage currents through the diodes are neglected [see Figure B.3 where both, the heater and the DAC currents are approximately the same in the first segment of the curve]. In this case Figure B.2 depicts the simplified version of the original circuit shown in Figure B.1. The ammeter for measuring heater current can be connected between P_L_C and the ground. Because of its negligible internal resistance simplified circuits in Figure B.2 remains the same.
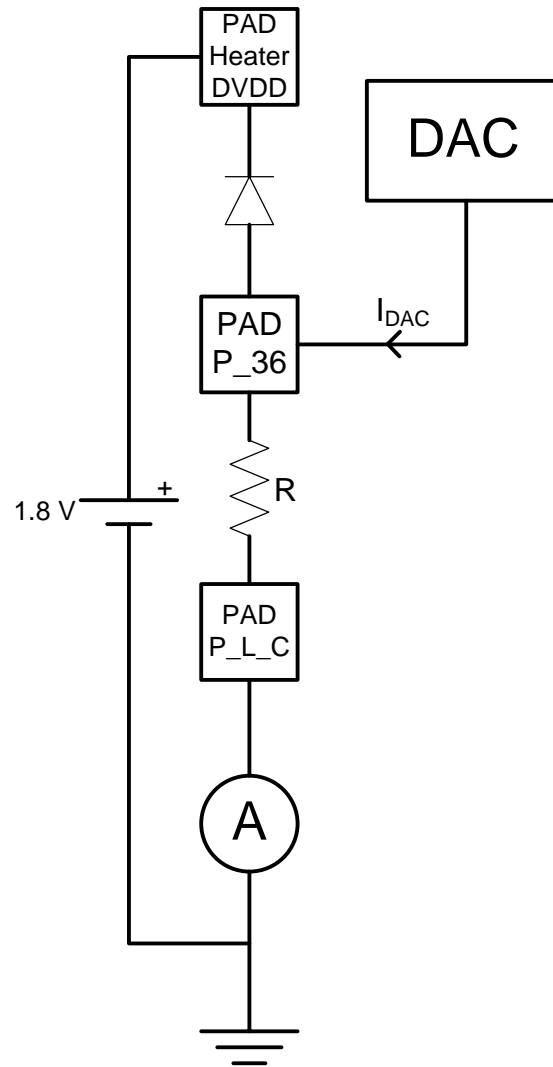
Figure B.2: Simplified circuits from Figure B.1.

B.2.2 Measurement results

In this subsection, we prove method experimentally by measuring mentioned heater R current.

Depending on the I_{DAC} values there are two cases for the diode above the PAD P_36 [follow Figure B.3]:

1) When an I_{DAC} is below 14.19 mA and therefore a voltage across the heater R is below 2.586 V (measured with KEITHLEY voltmeter), diode is OFF since voltage across it is below the diode threshold. In this case I_{DAC} and the heater current are approximately the same, measured with KEITHLEY ammeter.

2) When I_{DAC} is above 14.19 mA, the diode is ON and still the heater current is measurable.

In the second case, the I_{DAC} range of 14.10 to 20 mA still can be used for driving the ring Notch transfer function, but due to slow changes of the heater current with changes of I_{DAC}, it is concluded in consultation with my previous advisor Professor Vladimir Stojanović (while he was at MIT) that range of I_{DAC} from 0+ to 14.19 mA is sufficient for this purpose.
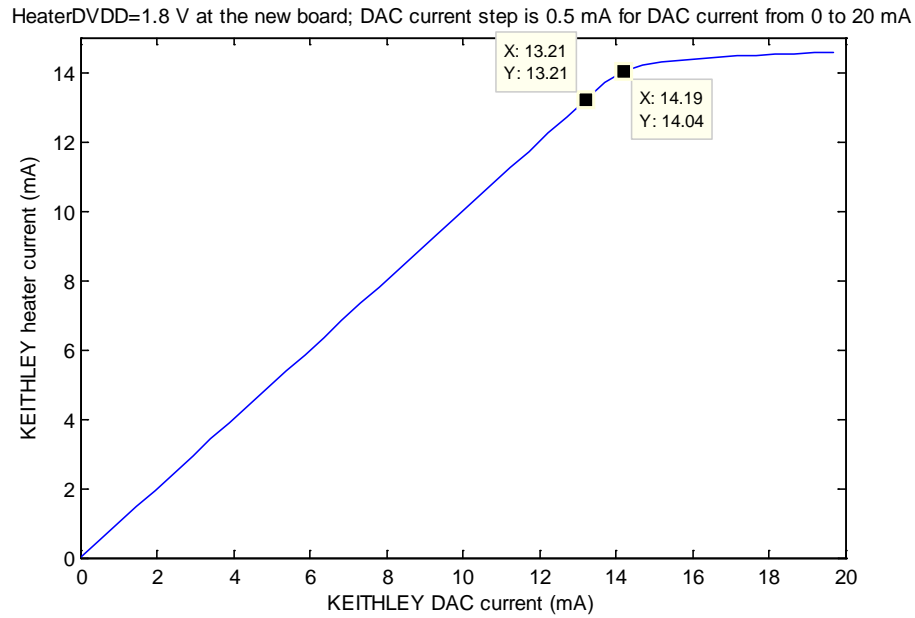
Figure B.3: Heater and DAC currents measured with KEITHLEY ammeter.

B.3 Novel symmetry method of heating chip on desired temperature

B.3.1 Description of symmetry method

By using this method, chip in a package on the chip board [see Figure 2.6(b) in section 2.1] can be heated on the desired temperature from the thermal controller by using the two external heaters placed in the two longitudinal metal parts [Benjamin Moss designed and made two the same metal parts – see Figure B.4(b) for one metal part] along two sides of the package on such a way that chip is in the middle (this is why it is symmetry method). Illustrated experimental setup is

184

(a)

(b)
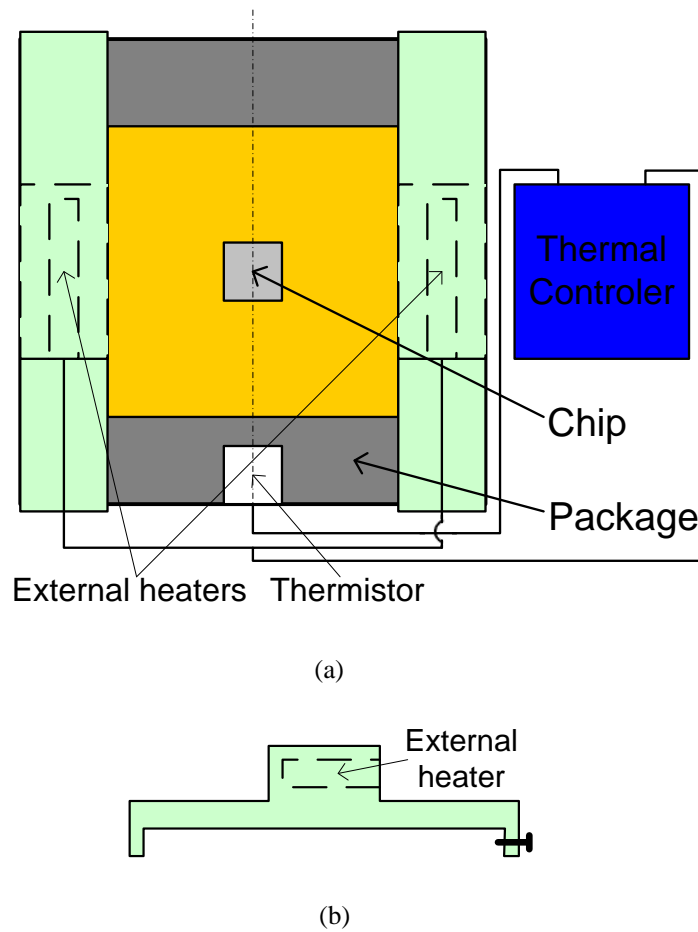
Figure B.4: (a) Top view of illustration of experimental setup; (b) Side view of external heater housing [two longitudinal metal parts (two heater housings) for external heaters are designed and made by Benjamin Moss].

shown in Figure B.4(a) [follow this Figure for further explanations]. Consequently, every line (in parallel with the dot-dashed line in the middle) along the package has approximately uniform temperature. Thus, the chip will have approximately uniform temperature. The previous is a good approximation since the chip has the small surface of 3 x 3 mm^2. The thermistor is placed on the

package (close to the package edge) in the dot-dashed line with the chip. This thermistor from the thermal controller is used to measure the temperature of the chip. But due to different materials on the chip and the package, calibration is performed, so the temperature of the chip can be measured well.

For the external heaters and the thermistors, we used the thermal paste to increase thermal conductivity and to make measurements more reliable.

For the calibration purpose, the second thermistor is placed on the chip itself. For this calibration, we used broken chip in the package, which is all made from the same materials as the operational chip in the package for thermal measurements. Figure B.5 depicts measured calibration curve between the chip temperature T_c and the temperature of the package (close to edge) T_p, for the thermal controller temperature range of 26.3 (room temperature) to 86.8 ^{o}C with the around 5 ^{o}C step. The linear fit for this graph is:

$$T_c = T_p - 3.1. \hspace{2cm} (B.1)$$

This equation is used for the calibration of measurements of the heater resistance vs. temperature of the chip by measuring a temperature of the package (close to the edge) from illustrated experimental setup from Figure B.4(a).
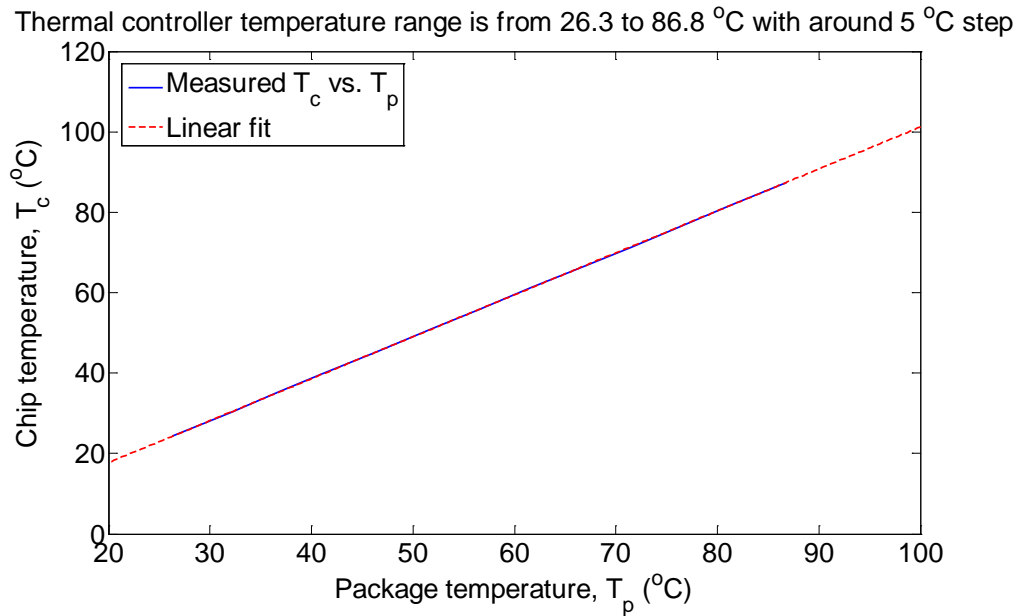
Figure B.5: Measured package edge and chip temperatures for calibration due to different materials.

B.3.2 Measurements of temperature by using symmetry method

The part of the chip circuit for obtaining the heater resistance R is depicted in the section B.2 in Figure B.1. The I_{DAC} current is adjusted to be 10.3 µA and it is measured by method in section B.2 as approximately constant heater current of the approximately the same value as adjusted I_{DAC}. For this measurement, the HeaterDVDD is adjusted to be 1.8 V. For thermal measurements by using the symmetry method, in order to obtain the heater resistance the voltage drop is measured across the heater for each temperature change and this voltage is divided with the approximately constant mentioned heater current.

By these thermal measurements, Figure B.6 is obtained after the calibration. In this Figure, it can be seen that the heater resistance has a linear dependence with the chip temperature, from which equation (B.2) is obtained by a linear fit.

$$R = 0.66\, T_c + 170. \tag{B.2}$$

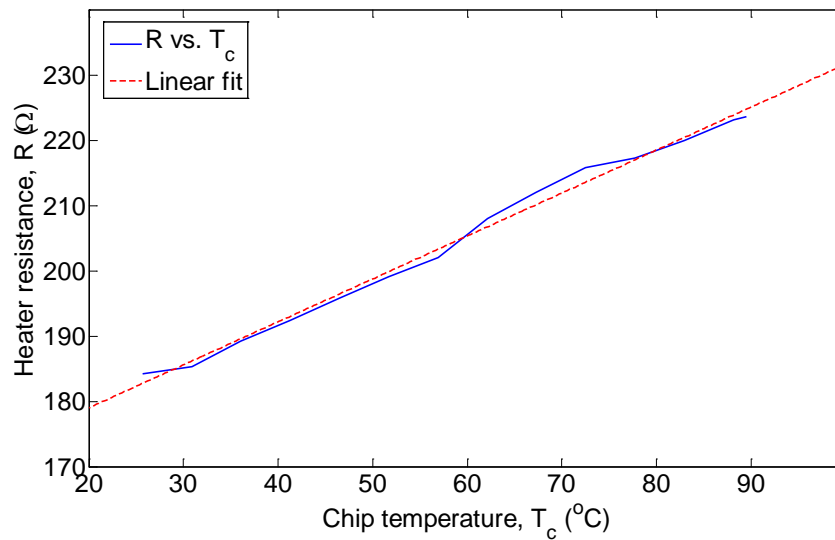**Figure B.6:** Calculated heater resistance R from measured heater current and voltage vs. chip temperatures in a range of thermal controller from 25.66 to 89.51 ^{o}C with around 5 ^{o}C step.

This method can be used to check devices features on desired temperatures, when the chip with these devices is exposed on them, because chip in the computer is exposed to the large temperatures.

B.4 Algorithm for measuring angles of optical fibers

The problem has been how to measure the input and the output fiber angles θ_1 and θ_2, respectively. These two angles are off-normal, which means that they are relative on the normal on the chip surface. When the devices on the chip are tested it is very important to know optical fiber angles in order to couple efficiently fiber with the grating coupler on the chip which is designed for a certain radiation angle. The image of both, the input and the output fiber [follow Figure B.7] is shown on the laptop screen in the lab through the side visible camera. We wrote a program (algorithm) which with the image processing extracts angle of optical fibers, from both fibers on the screen, the input fiber in the chip from the external laser and the output fiber from the chip to the external photodetector. Figure B.8 shows this algorithm in steps.
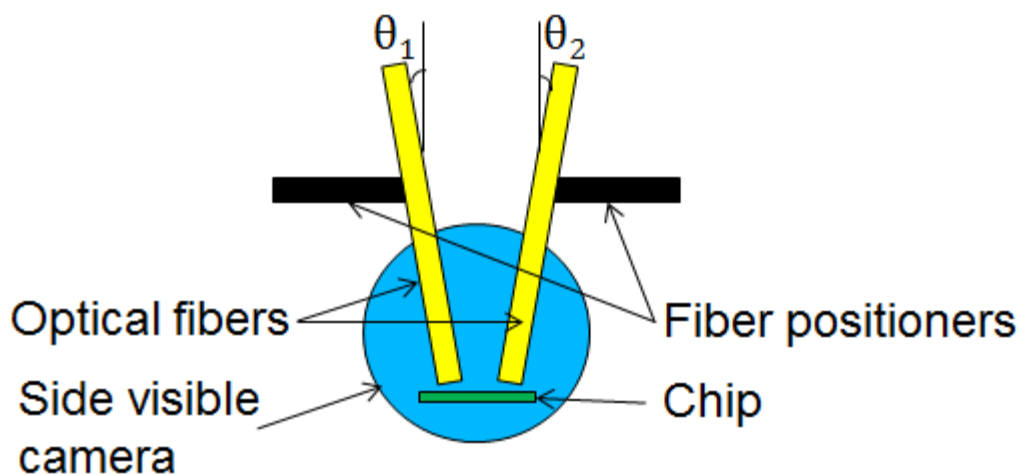
Figure B.7: Illustration of front view of experimental setup for measuring angles θ_1 and θ_2.

The obtained values of θ_1 and θ_2 by using the written program with this algorithm are compared with the manually measured θ_1 and θ_2 on the laptop screen (picture from the side visible camera) with the protractor. As a result, both gave approximately the same result, which is proven that algorithm works well.

From video input
take the snapshot
(image)

↓

Convert image in
binary image
based on level of
luminance

↓

For a fixed range of two
vertical coordinates find for
each, horizontal
coordinate, and all this for
left and right fiber

↓

Based on coordinates
calculate two normal-off
angles of two fibers

Figure B.8: Algorithm in steps.

B.5 Conclusions

A novel measurement method of current through heater on the electro-optical chip is proven theoretically and experimentally. It can be used in the simplification of described circuits topology of forward and reverse bias diodes on the electro-optical chip (and measurement of current). This topology can be either complete circuits or part of larger circuits.

A novel symmetry method of heating the chip on a desired temperature is proven experimentally to be useful for testing the performance of elect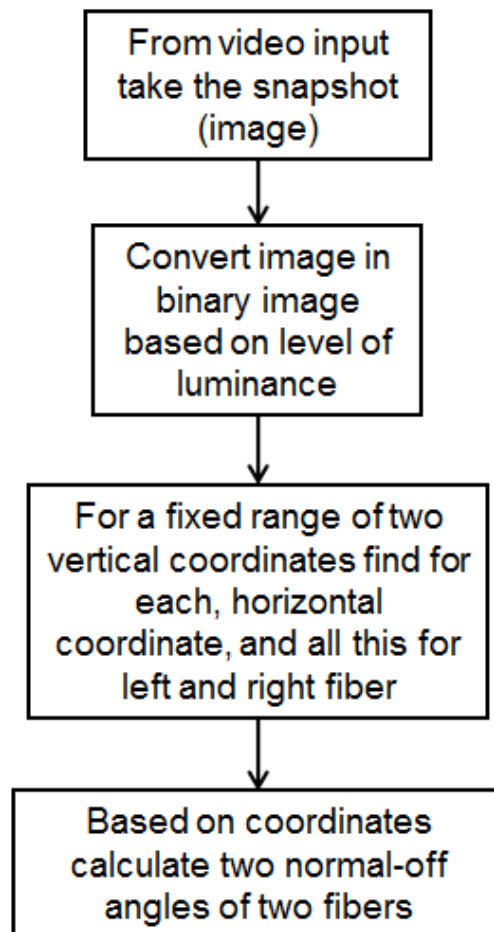rical, electro-optical and optical devices on the chip; while chip is in the package and the package is connected to the chip board. Operational temperature range of these devices is still not determined since this project is still in developing. This method can be used for any thermal testing of anything that is symmetrical.

Algorithm for measuring angles of optical fibers is programmed and proven experimentally to work well. This algorithm can also measure angles in the real time. In addition, fibers can be adjusted using positioners through the other software which controls these positioners. Therefore, this algorithm can be applied as angles feedback, thus desired angles can be given as input and automatically adjusted by positioners.

Also, these three methods can be used in other applications besides presented in this appendix.

Bibliography

[1] S. Beamer, C. Sun, Y.-J. Kwon, A. Joshi, C. Batten,V. Stojanović, K. Asanović, "Re-Architecting DRAM Memory Systems with Monolithically Integrated Silicon Photonics," ISCA '10, 129-140 (2010).

[2] C. Batten, A. Joshi, J. Orcutt, A. Khilo, B. Moss, C. Holzwarth, M. Popovic, Hanqing Li, H. Smith, J. Hoyt, F. Kartner, R. Ram, V. Stojanovic, and K. Asanovic, "Building manycore processor-to-dram networks with monolithic silicon photonics," 16th IEEE Symposium on High Performance Interconnects, 21-30 (2008).

[3] J. S. Orcutt, A. Khilo, M.A. Popovic, C.W. Holzwarth, B. Moss, Hanqing Li, M.S. Dahlem, T.D. Bonield, F.X. Kartner, E.P. Ippen, J.L. Hoyt, R.J. Ram, and V. Stojanovic, "Demonstration of an electronic photonic integrated circuit in a commercial scaled bulk CMOS process," Conference CLEO/QELS 2008, paper CTuBB3 (2008).

[4] C. W. Holzwarth, J. S. Orcutt, Hanqing Li, M. A. Popovic, V. Stojanovic, J. L. Hoyt, R. J. Ram, and H. I. Smith, "Localized substrate removal technique enabling strong-confinement microphotonics in bulk Si CMOS processes," Conference CLEO/QELS 2008, paper CThKK5 (2008).

[5] J. S. Orcutt, B. Moss, C. Sun, J. Leu, M. Georgas, J. Shainline, E. Zgraggen, H. Li, J. Sun, M. Weaver, S. Urošević, M. Popović, R. J. Ram and V. Stojanović, "Open Foundry Platform for High-Performance Electronic-Photonic Integration", Opt. Express **20**, 12222-12232 (2012).

[6] B. R. Moss, "High-Speed Modulation of Resonant CMOS Photonic Modulators in Deep-Submicron Bulk-CMOS," Master Thesis, MIT (2009).

[7] B. R. Moss, C. Sun, M. Georgas, J. Shainline, J. S. Orcutt, J. C. Leu, M. Wade, Y.-H. Chen, K. Nammari, X. Wang, H. Li, R. Ram, M. A. Popovic, V. Stojanovic, "A 1.23pJ/b 2.5Gb/s Monolithically Integrated Optical Carrier-Injection Ring Modulator and All-Digital Driver Circuit in Commercial 45nm SOI," Conference ISSCC 2013 / Session 7 / Optical Transceivers and Silicon Photonics / 7.6, 18-20 (2013).

[8] M. Georgas, J. Orcutt, R. J. Ram, and V. Stojanović, "A Monolithically-Integrated Optical Receiver in Standard 45-nm SOI," IEEE Journal of Solid-State Circuits **47**, 1693-1702 (2012).

[9] D. Taillaert, "Grating couplers as Interface between Optical Fibres and Nanophotonic Waveguides," PhD thesis, Universiteit Gent, Faculteit Toegepaste Wetenschappen, Vakgroep Informatietechnologie (2004).

[10] J. Orcutt, "Monolithic Electronic-Photonic Integration in State-of-the-Art CMOS Processes", PhD Thesis, Massachusetts Institute of Technology (2012).

[11] F. Laere, G. Roelkens, M. Ayre, J. Schrauwen, D. Taillaert, D. Van Thourhout, T. Krauss, R. Baets, "Compact and Highly Efficient Grating Couplers

Between Optical Fiber and Nanophotonic Waveguides," Journal of lightwave technology **25**, 151-156, (2007).

[12] S. Scheerlinck, J. Schrauwen, F. Van Laere, D. Taillaert, D. Van Thourhout, R. Baets, "Efficient, broadband and compact metal grating couplers for silicon-on-insulator waveguides," Opt. Express **15**, 9625-9630 (2007).

[13] C. R. Doerr, L. Chen, Y.-K. Chen, L. L. Buhl, "Wide Bandwidth Silicon Nitride Grating Coupler," IEEE Photonics Technology Letters **22**, 1461-1463 (2010).

[14] D. Taillaert, P. Bienstman, R. Baets, "Compact efficient broadband grating coupler for silicon-on-insulator waveguides," Optics Letters **29**, 2749-2751 (2004).

[15] G. Roelkens, D. Vermeulen, D. Van Thourhout, R. Baets, S. Brision, P. Lyan, P. Gautier, J.-M. Fédéli, "High efficiency diffractive grating couplers for interfacing a single mode optical fiber with a nanophotonic silicon-on-insulator waveguide circuit," Applied Physics Letters **92**, 131101 (2008).

[16] R. Waldhausl, B. Schnabel, P. Dannberg, E. Kley, A. Brauer, and W. Karthe, "Efficient coupling into polymer waveguides by gratings," Appl. Opt. **36,** 9383 (1997).

[17] D. Taillaert, F. Laere, M. Ayre, W. Bogaerts, D. Thourhout, P. Bienstman, R. Baets, "Grating Couplers for Coupling between Optical Fibers and Nanophotonic Waveguides," Japanese Journal of Applied Physics **45**, 6071–6077 (2006).

[18] X. Chen, C. Li, and H. K. Tsang, "Fabrication-tolerant waveguide chirped grating coupler for coupling to a perfectly vertical optical fiber," IEEE Photon. Technol. Lett. **20**, 1914-1916 (2008).

[19] Y. Tang, Z. Wang, L. Wosinski, U. Westergren, S. He, "Highly efficient nonuniform grating coupler for silicon-on-insulator nanophotonic circuits," Optics Letters **35**, 1290-1292 (2010).

[20] B. Schmid, A. Petrov, M. Eich, "Optimized grating coupler with fully etched slots," Opt. Express **17**, 11066-11076, (2009).

[21] C. A. Flory, "Analysis of Directional Grating-Coupled Radiation in Waveguide Structures," IEEE Journal of Quantum Electronics **40**, 949-957, (2004).

[22] M. Fan, "Efficient Out-of-Plane Microphotonic Fiber-to-Chip Coupler Designs," MEng thesis, Massachusetts Institute of Technology (2006).

[23] M. Fan, M. A. Popović and F. X. Kartner, "High Directivity, Vertical Fiber-to-Chip Coupler with Anisotropically Radiating Grating Teeth," in Conference on Lasers and Electro-Optics (CLEO), OSA Technical Digest, Optical Society of America, Washington DC (2007).

[24] I.A. Avrutsky, A.S. Svakhin and V.A. Sychugov, "Interference Phenomena in Waveguides with Two Corrugated Boundaries" Journal of modern optics **36**, 1303-1320 (1989).

[25] A. B. Greenwell, S. Boonruang, and M. G. Moharam, "All-dielectric unidirectional dual-grating output coupler," Opt. Express **15**, 266-277 (2007).

[26] W. D. Sacher, Y. Huang, L. Ding, B. J. F. Taylor, H. Jayatilleka, G.-Q. Lo, and J. K. S. Poon, "Wide bandwidth and high coupling efficiency Si3N4-on-SOI dual-level grating coupler," Optics Express **22**, 10938-10947 (2014).

[27] B. Wang, J. Jiang, G. P. Nordin, "Compact slanted grating couplers," Optics Express **12**, 3313-3326 (2004).

[28] S. Choi, A. Higo, M. Zaitsu, M.-J. Kwack, M. Sugiyama, H. Toshiyoshi, Y. Nakano, "Development of a vertical optical coupler using a slanted etching of InP/InGaAsP waveguide," IEICE Electronics Express **10**, 1-8 (2013).

[29] F. Van Laere, M. V. Kotlyar, D. Taillaert, D. Van Thourhout, T. F. Krauss, and R. Baets, "Compact Slanted Grating Couplers Between Optical Fiber and InP–InGaAsP Waveguides," IEEE Photonics Technology Letters **19**, 396-398 (2007).

[30] J. Schrauwen, F. Van Laere, D. Van Thourhout, and R. Baets, "Focused-Ion-Beam Fabrication of Slanted Grating Couplers in Silicon-on-Insulator Waveguides," IEEE Photonics Technology Letters **19**, 816-818 (2007).

[31] B. Wang, J. Jiang, and G. P. Nordin, "Embedded Slanted Grating for Vertical Coupling Between Fibers and Silicon-on-Insulator Planar Waveguides," IEEE Photonics Technology Letters **17**, 1884-1886 (2005).

[32] H. J. Gerritsen, D. K. Thornton, and S. R. Bolton, "Application of Kogelnik's two-wave theory to deep, slanted, highly efficient, relief transmission gratings," Applied Optics **30**, 807-814 (1991).

[33] M. G. Moharam and T. K. Gaylord, "Rigorous coupled-wave analysis of planar-grating diffraction," J. Opt. Soc. Am. **71**, 811-818 (1981).

[34] M. G. Moharam and T. K. Gaylord, "Rigorous coupled-wave analysis of grating diffraction-E-mode polarization and losses," J. Opt. Soc. Am. **73**, 451-455 (1983).

[35] T. Levola, and P. Laakkonen, "Replicated slanted gratings with a high refractive index material for in and outcoupling of light," Optics Express **15**, 2067-2074 (2007).

[36] T. Aoyagi, Y. Aoyagi, and S. Namba, "High efficiency blazed grating couplers," Applied Physics Letters **29**, 303-304 (1976).

[37] J. Dutta, S. A. Ramakrishna, and A. Lakhtakia, "Periodically patterned columnar thin films as blazed diffraction gratings," Applied Physics Letters **102**, 161116 (2013).

[38] M. Oliva, D. Michaelis, F. Fuchs, A. Tünnermann, and U. D. Zeitner, "Highly efficient broadband blazed grating in resonance domain," Applied Physics Letters **102**, 203114 (2013).

[39] L. Quan, W. Jianhong, C. Minghui, C. Yu, "The fabrication of the holographic dual-blazed grating," 2013 International Conference on Optical

Instruments and Technology: Micro/Nano Photonics and Fabrication, Proc. of SPIE **9047**, 90470F-1 (2013).

[40] J. Ling, D. Zhang, Y. Huang, Q. Wang and S. Zhuang, "Fabrication of holographic blazed grating with Fourier synthesis exposure," Journal of Modern Optics (2014).

[41] M. Ekberg, F. Nikolajeff, M. Larsson, and S. Hard, "Proximity-compensated blazed transmission grating manufacture with direct-writing, electron-beam lithography," Applied Optics **33**, 103-107 (1994).

[42] Q. Liu, J. Wu, M. Chen, "Fabrication of blazed grating by native substrate grating mask," Optical Engineering **52(9)**, 091706 (2013).

[43] J. Feng and Z. Zhou, "Polarization beam splitter using a binary blazed grating coupler," Optics Letters **32**, 1662-1664 (2007).

[44] Y. Xia, E. Kim, X.-M. Zhao, J. A. Rogers, M. Prentiss, G. M. Whitesides, "Complex Optical Surfaces Formed by Replica Molding Against Elastomeric Masters," Science **273**, 347-349 (1996).

[45] C. Manolatou, "Passive Components for Dense Optical Integration Based on High Index-Contrast", PhD Thesis, Massachusetts Institute of Technology (2001).

[46] J. A. Kong, "Electromagnetic Wave Theory", EMW Publishing (2008).

[47] G. Roelkens, D. Van Thourhout, R. Baets, "High efficiency grating coupler between silicon-on-insulator waveguides and perfectly vertical optical fibers," Optics Letters **32**, (2007).

[48] B. Luyssaert, P. Vandersteegen, D. Taillaert, P. Dumon, W. Bogaerts, P. Bienstman, D. Van Thourhout, V. Wiaux, S. Beckx, R. Baets, "A Compact Photonic Horizontal Spot-Size Converter Realized in Silicon-on-Insulator," IEEE Photonics Technology Letters **17**, 73-75 (2005).

[49] X. Chen, C. Li, C. Fung, S. Lo, H. Tsang, "Apodized Waveguide Grating Couplers for Efficient Coupling to Optical Fibers," IEEE Photonics Technology Letters **22** (2010).

[50] G. Roelkens, D. Van Thourhout, R. Baets, "High efficiency Silicon-on-Insulator grating coupler based on a poly-Silicon overlay," Opt. Express **14**, 11622-11630 (2006).

[51] K. Bates, L. Li, R. Roncone, and J. Burke, "Gaussian beams from variable groove depth grating couplers in planar waveguides," Appl. Opt. **32**, 2112 (1993).

[52] D. Vermeulen, S. Selvaraja, P. Verheyen, G. Lepage, W. Bogaerts, P. Absil, D. Van Thourhout, G. Roelkens, "High-efficiency fiber-to-chip grating couplers realized using an advanced CMOS-compatible Silicon-On-Insulator platform," Opt. Express **18**, 18278-18283 (2010).

[53] Y. Tang, Z. Wang, U. Westergren and L. Wosinski, "High Efficiency Nonuniform Grating Coupler by Utilizing the Lag Effect in the Dry Etching Process," Optical Fiber Communication (OFC), collocated National Fiber Optic Engineers Conference (2010).

[54] D. Vermeulen, S. Selvaraja, P. Verheyen, G. Lepage, W. Bogaerts, G. Roelkens, "High-efficiency Silicon-On-Insulator Fiber-to-Chip Grating Couplers Using a Silicon Overlay," Group IV photonics, United States, p.FPd1 (2009).

[55] H.-Y. Chen and K.-C. Yang, "Design of a high-efficiency grating coupler based on a silicon nitride overlay for silicon-on-insulator waveguides," Applied Optics **49**, 6455-6462 (2010).

[56] X. Chen, C. Li, S. M. G. Lo, K. Fung, and H. K. Tsang, "Silicon Waveguide Grating Couplers with Engineered Coupling Strength for Optimized Coupling," European Conference on Integrated Optics (2010).

[57] D. Taillaert, W. Bogaerts, P. Bienstman, T. F. Krauss, P. Van Dale, I. Moerman, S. Verstuyft, K. De Mesel, and R. Baets, "An out-of-plane grating coupler for efficient butt-coupling between compact planar waveguides and single-mode fibers," IEEE J. Quantum Electron. **14**, 949–955 (2002).

[58] C. Li, H. Zhang, M. Yu, and G. Q. Lo, "CMOS-compatible high efficiency double-etched apodized waveguide grating coupler," Opt. Express **21**, 7868-7874 (2013).

[59] J. S. Yang, B.-H. O, S. H. Hong, S. G. Lee, S.-G. Park, J.-H. Kim, D.-J. Chung, S.-P. Chang, and E.-H. Lee, "Novel Grating Design for Out-of-Plane Coupling with Nonuniform Duty Cycle," IEEE Photonics Technology Letters **20**, 730-732 (2008).

[60] M. Antelius, K. B. Gylfason, and H. Sohlström, "An apodized SOI waveguide-to-fiber surface grating coupler for single lithography silicon photonics," Optics Express **19**, 3592-3598 (2011).

[61] X. Chen, Z. Cheng, C. K. Y. Fung, and H. K. Tsang, "Design and Applications of Silicon Waveguide Grating Couplers," Silicon Photonics VII, Proc. of SPIE 8266, 82660I-1 (2012).

[62] H. A. Haus, "Waves and fields in optoelectronics", Prentice-Hall, Englewood Cliffs, New Jersey (1984).

[63] A. Katzir, A. C. Livanos, J. B. Shellan, and A. Yariv, "Chirped gratings in Integrated Optics," IEEE Journal of Quantum Electronics **QE-13**, 296-304 (1977).

[64] J. S. Orcutt, B. Moss, C. Sun, J. Leu, M. Georgas, S. Urosevic, H. Li, J. Sun, M. Weaver, E. Zgraggen, R. J. Ram, V. Stojanovic, J. Shainline, M. Popovic, "Low Loss Waveguide Integration within a Thin-SOI CMOS Foundry", Optical Interconnects Conference, IEEE (2012).

[65] J. S. Orcutt, A. Khilo, C. W. Holzwarth, M. A. Popović, H. Li, J. Sun, T. Bonifield, R. Hollingsworth, F. X. Kärtner, H. I. Smith, V. Stojanović, and R. J. Ram, "Nanophotonic integration in state-of-the-art CMOS foundries," Opt. Express **19**, 2335-2346 (2011).

[66] D. Heitmann and R. V. Pole, "Two-dimensional focusing holographic grating coupler," Applied Physics Letters **37**, 585-587 (1980).

[67] C. Lacava, P. Minzioni, E. Baldini, L. Tartara, J. M. Fedeli, and I. Cristiani, "Nonlinear characterization of hydrogenated amorphous silicon waveguides and analysis of carrier dynamics," Applied Physics Letters **103**, 141103 (2013).

[68] F. Van Laere, T. Claes, J. Schrauwen, S. Scheerlinck, W. Bogaerts, D. Taillaert, L. O'Faolain, D. Van Thourhout, and R. Baets, "Compact Focusing Grating Couplers for Silicon-on-Insulator Integrated Circuits," IEEE Photonics Technology Letters 19, 1919-1921 (2007).

[69] S. Ura, H. Sunagawa, T. Suhara, and H. Nishihara, "Focusing Grating Couplers for Polarization Detection," Journal of Lightwave Technology **6**, 1028-1033 (1988).

[70] P-P. Borsboom and H. J. Frankena, "Field analysis of two-dimensional focusing grating couplers," J. Opt. Soc. Am. A **12**, 1142-1146 (1995).

[71] N. Ayotte, K. Bédard and S. LaRochelle, "Single-etch step grating couplers for SOI waveguides," Photonics North 2013, Proc. of SPIE **8915**, 89150X-1 - 89150X-13 (2013).

[72] Y. Wang, J. Flueckiger, C. Lin, and L. Chrostowski, "Universal Grating Coupler Design," Photonics North 2013, Proc. of SPIE **8915**, 89150Y-1 – 89150Y-7 (2013).

[73] T. Suhara, K. Okada, T. Saso, and H. Nishihara, "Focusing Grating Coupler in AlGaAs Optical Waveguide," IEEE Photonics Technology Letters **4**, 903-905 (1992).

[74] R. Waldhausl, B. Schnabel, E.-B. Kley and A. Brauer, "Efficient focusing polymer waveguide grating couplers," Electronics Letters **33**, 623-624 (1997).

[75] J. Backlund, J. Bengtsson, C.-F. Carlström, and A. Larsson, "Multifunctional Grating Couplers for Bidirectional Incoupling into Planar Waveguides," IEEE Photonics Technology Letters **12**, 314-316 (2000).

[76] D. Heitmann and C. Ortiz, "Calculation and Experimental Verification of Two-Dimensional Focusing Grating Couplers," IEEE Journal of Quantum Electronics **QE-17**, 1257-1263 (1981).

[77] M. Miler, and M. Skalsky, "Stigmatically Focusing Grating Coupler," Electronics Letters 15, 275-276 (1979).

[78] F. Van Laere, W. Bogaerts, P. Dumon, G. Roelkens, D. Van Thourhout, and R. Baets, "Focusing Polarization Diversity Grating Couplers in Silicon-on-Insulator," Journal of Lightwave Technology 27, 612-618 (2009).

[79] Y. Li, L. Li, B. Tian, G. Roelkens, and R. G. Baets, "Reflectionless Tilted Grating Couplers With Improved Coupling Efficiency Based on a Silicon Overlay," IEEE Photonics Technology Letters **25**, 1195-1198 (2013).

[80] B. Yang, Z.-Y. Li, X. Xiao, J.-Z. Yu, Y.-D. Yu, "High-efficiency Focusing Grating Coupler for Large-Scale Silicon Photonic Integration," IEEE, 160-162 (2013).

[81] Z. Cheng and H. K. Tsang, "Focusing Subwavelength Grating Couplers," ACP/IPOC 2013, AW4B.3.pdf (2013).

[82] S. Ura, T. Suhara, and H. Nishihara, "Aberration characterizations of a focusing grating coupler in an integrated-optic disk pickup device," Applied Optics **26**, 4777-4782 (1987).

[83] L. U. Kempen, R. E. Kunz, "Replicated Mach-Zehnder interferometers with focusing grating couplers for sensing applications," Sensors and Actuators B **38-39**, 295-299 (1997).

[84] G. N. Lawrence and P. J. Cronkite, "Physical optics analysis of the focusing grating coupler," Applied Optics **27**, 672-678 (1988).

[85] P. J. Cronkite and G. N. Lawrence, "Focusing grating coupler design method using holographic optical elements," Applied Optics **27**, 679-683 (1988).

[86] J. Seligson, "Modeling of a focusing grating coupler using vector scattering theory," Applied Optics **27**, 684-692 (1988).

[87] G. N. Lawrence, K. E. Moore, and P. J. Cronkite, "Rotationally symmetric construction optics for a waveguide focusing grating," Applied Optics **29**, 2315-2319 (1990).

[88] F. Sogawa, Y. Hori, and M. Kato, "Fabrication of aberration-free focusing grating couplers, Applied Optics **29**, 5103-5105 (1990)."

[89] Y. Amitai, I. A. Erteza, and J. W. Goodman, "Recursive design of a holographic focusing grating coupler," Applied Optics **30**, 3886-3890 (1991).

[90] S. Nishiwaki, J.-i. Asada, and S. Uchida, "Optical head employing a concentric-circular focusing grating coupler," Applied Optics **33**, 1819-1827 (1994).

[91] A.R. Zakharian, S.A. Kuchinsky, X. Liu, and A. Kobyakov, "Grating-based Fiber-to-chip Coupling Efficiency for Small Mode Field Diameter Fibers," Advanced Photonics Congress, JT3A.9.pdf (2013).

[92] Z. Cheng, X. Chen, C. Y. Wong, K. Xu, and H. K. Tsang, "Broadband focusing grating couplers for suspended-membrane waveguides," Optics Letters **37**, 5181-5183 (2012).

[93] S. Romero-García, F. Merget, F. Zhong, H. Finkelstein, and J. Witzens, "Visible wavelength silicon nitride focusing grating coupler with AlCu/TiN reflector," Optics Letters **38**, 2521-2523 (2013).

[94] F. Van Laere, W. Bogaerts, P. Dumon, G. Roelkens, D. Van Thourhout, and R. Baets, "Focusing polarization diversity gratings for Silicon-on-Insulator integrated circuits," ThB3, IEEE, 203-205 (2008).

[95] G. Roelkens, D. Vermeulen, F. Van Laere, S. Selvaraja, S. Scheerlinck, D. Taillaert, W. Bogaerts, P. Dumon, D. Van Thourhout, and R. Baets, "Bridging the Gap Between Nanophotonic Waveguide Circuits and Single Mode Optical Fibers Using Diffractive Grating Structures," Journal of Nanoscience and Nanotechnology **10**, 1551-1562 (2010).

[96] J. S. Orcutt, S. D. Tang, S. Kramer, K. Mehta, H. Li, V. Stojanović, and R. J. Ram, "Low-loss polysilicon waveguides fabricated in an emulated high-volume electronics process," Optics Express **20**, 7243-7254 (2012).

[97] W. Yu, "Electromagnetic simulation techniques based on the FDTD method," Wiley & Sons, Inc. Hoboken, New Jersey (2009).

[98] N. Yamamoto, Y. Watanabe and K. Komori, "Design of photonic crystal directional coupler with high extinction ratio and small coupling length," Jpn. J. Appl. Phys. **44,** 2575-2578 (2005).

[99] E. A. J. Marcatili, "Dielectric Rectangular Waveguide and Directional Coupler for Integrated Optics," The Bell System Technical Journal, 2071-2102 (September 1969).

[100] H. Kogelnik, R. Schmidt, "Switched Directional Couplers with Alternating $\Delta\beta$," IEEE Journal of Quantum Electronics **QE-12**, 396-401 (1976).

[101] R. V. Schmidt and H. Kogelnik, "Electro-optically Switched Coupler with Stepped $\Delta\beta$ Reversal Using Ti-diffused LiNbO$_3$ Waveguides," Appl. Phys. Lett. **28**, 503-506 (1976).

[102] H. A. Haus and C. G. Fonstad, "Three-Waveguides Coupler for Improved Sampling and Filtering," IEEE Journal of Quantum Electronics **QE-17**, 2321-2325 (1981).

[103] J. C. Campbell, F. A. Blum, D. W. Shaw, and K. L. Lawley, "GaAs electro-optic directional-coupler switch," Applied Physics Letters **27**, 202-205 (1975).

[104] M. Papuchon, Y. Combemale, X. Mathieu, D. B. Ostrowsky, L. Reiber, A. M. Roy, B. Sejourne, and M. Werner , "Electrically switched optical directional coupler: Cobra, " Applied Physics Letters **27**, 289-291 (1975).

[105] E. Van Tomme, P. Van Daele, R. Baets, G. R. Möhlmann, and M. B. J. Diemeer, "Guided wave modulators and switches fabricated in electro-optic polymers," J. Appl. Phys. **69 (9)**, 6273-6276 (1991).

[106] F. T. Stone, J. E. Watson, D. T. Moser, and W. J. Minford, "Performance and yield of pilot-line quantities of lithium niobate switches," SPIE **1177**, Integrated Optics and Optoelectronics, 322-326 (1989).

[107] H. Takeuchi, Y. Hasumi, S. Kondo and Y. Noguchi "4 x 4 Directional Coupler Switch Matrix with an InGaAIAs/lnAIAs Multiquantum Well Structure," Electronics Letters **29**, 523-524 (1993).

[108] N. Ked, H.H. Yao, C. Zawadzki and B. Strebel, "4x4 polymer thermo-optic directional coupler switch at 1.55bm," Electronics Letters **30**, 639-640 (1994).

[109] K. Kawano, S. Sekine,, H. Takeuchi, M. Wada, M. Kohtoku, N. Yoshimoto, T. Ito, M. Yanagibashi, S. Kondo and Y. Noguchi, "4x4 InGaAIAs/lnAIAs MQW directional coupler waveguide switch modules integrated with spot-size converters and their 10Gbit/s operation,**"** Electronics Letters **31**, 96-97 (1995).

[110] N. Keil, H.H. Yao, C. Zawadzki and B. Strebel, "Rearrangeable nonblocking polymer waveguide thsrmo-optic 4x4 switching matrix with low power consumption at 1.55pm," Electronics Letters **31**, 403-404 (1995).

[111] A. Shakouri, B. Liu, B.-G. Kim, P. Abraham, A. W. Jackson, A. C. Gossard, J. E. Bowers, "Wafer-Fused Optoelectronics for Switching," Journal of Lightwave Technology **16**, 2236-2242 (1998).

[112] S.-C. Cho, B.-G. Kim, Y. Moon, A. Shakouri, "Ultra Short Two-Section Vertical Directional Coupler Switches with High Extinction Ratios,"Jpn. J. Appl. Phys. **40**, 4045-4050 (2001).

[113] K. Nashimoto, "PLZT Waveguide Devices for High Speed Switching and Filtering," OThE4, OFC/NFOEC Conference (2008).

[114] S. L. Chuang, "Physics of Photonic Devices," A John Wiley & Sons, Inc. Publication (2009).

[115] H.-C. Huang, "Coupled Mode Theory: As Applied to Microwave and Optical Transmission," VNU Science Press, UTRECHT, Netherlands (1984).

[116] A. Sharkawy, S. Shi, D. W. Prather, R. A. Soref, "Electro-optical switching using coupled photonic crystal waveguides," Optics Express **10**, 1048-1059 (2002).

[117] N. Yamamoto, T. Ogawa, and K. Komori, "Photonic crystal directional coupler switch with small switching length and wide bandwidth," Optics Express **14**, 1223-1229 (2006).

[118] Y. Enami, D. Mathine, C. T. DeRose, R. A. Norwood, J. Luo, A. K-Y. Jen, and N. Peyghambarian, "Hybrid electro-optic polymer/sol-gel waveguide directional coupler switches," Appl. Phys. Lett. **94**, 213513 (2009).

[119] N. Yamamoto, Y. Watanabe and Kazuhiro Komori, "Design of Photonic Crystal Directional Coupler with High Extinction Ratio and Small Coupling Length," Japanese Journal of Applied Physics **44**, 2575–2578 (2005).

[120] B. Deka, A. Dutta, G. Hegde and P. P. Sahu, "Fabrication and comprehensive study of silicon oxynitride based compact directional coupler and multimode interference coupler," Proc. of SPIE **8760**, 876024 (2013).

[121] A. S. M. Supa'at, A. B. Mohammad, N. M. Kassim, and S. M. Idrus, "Low Power Consumption Thermooptic Switch Using Polymers," Asia-Pacific Conference on Applied Electromagnetics Proceedings (2005).

[122] T. Ushio, K. Tsukamoto, and K. Utaka, "Proposal of Polarization-Independent Silicon Wire-Waveguide Directional Coupler Optical Switch," 17th Microoptics Conference (MOC' 11) (2011).

[123] X. Lin, D. Liu and J.-J. He, "Design and Optimization of a 2x2 Half-Wave Optical Coupler," SaM6, OSA/AOE (2008).

[124] B. Deka, P. P. Sahu, "Transformation relationship of directional coupler with multimode interference coupler and two mode interference coupler," J. Opt **38 (2)**, 75–87 (2009).

[125] A. W. L. Junior and A. S. B. Sombra, "Switching Cell of Directional Coupler Embedded in Photonic Crystal Driven by an External Command (for the C, L, and U bands of ITU)," Journal of Communication and Information Systems **24**, 40-45 (2009).

[126] A. Zakery and M. Hatami, "Nonlinear optical properties of pulsed-laserdeposited GeAsSe films and simulation of a nonlinear directional coupler switch," J. Opt. Soc. Am. B **22**, 591-597 (2005).

[127] D. C. Zografopoulos and R. Beccherelli, " Long-range plasmonic directional coupler switches controlled by nematic liquid crystals," Optics Express **21**, 8240-8250 (2013).

[128] A. S. M. Supa'at, A. B. Mohammad and N. M. Kassim, "Design of Polymer Based Directional Coupler Thermooptic Optical Switch," Conference ICECE 2004, 135-138 (2004) .

[129] C.-H. Bae and Y.-H. Son, "Design and Fabrication of Directional Coupler Type Hollow Waveguide Optical Switch with Variable Air Core," Conference ITC-CSCC 2008, 1409-1412 (2008).

[130] G.-R. Zhou, M. W. Geis, S. J. Spector, F. Gan, M. E. Grein, R. T. Schulein, J. S. Orcutt, J. U. Yoon, D. M. Lennon, T. M. Lyszczarz, E. P. Ippen, and F. X. Kärtner, "Effect of carrier lifetime on forward-biased silicon Mach-Zehnder modulators," Optics Express **16**, 5218-5226 (2008).

[131] G. Singh, R. P. Yadav, and V. Janyani, "Multimode Interference (MMI) coupler based All Optical Switch: Design, Applications & Performance Analysis," International Journal of Recent Trends in Engineering **1**, 115-119 (2009).

[132] L. B. Soldano and E. C. M. Pennings, "Optical Multi-Mode Interference Devices Based on Self-Imaging: Principles and Applications,"Journal of Lightwave Technology **13**, 615-627 (1995).

[133] F. Wang, J. Yang, L. Chen, X. Jiang, and M. Wang, "Optical Switch Based on Multimode Interference Coupler," IEEE Photonics Technology Letters **18**, 421-423 (2006).

[134] R. Ulrich and G. Ankele, "Self-imaging in homogeneous planar optical waveguides,"Appl. Phys. Lett **27**, 337–339 (1975).

[135] L. Soldano and E. Pennings, "Optical multi-mode interference devices based on self-imaging: Principles and applications," J. Lightw. Technol. **13**, 615–627 (1995).

[136] R. Yin, X. Jiang, J. Yang, and M. Wang, "Structure with improved selfimaging in its graded-index multimode interference region,"J. Opt. Soc. Amer. B **19**, 1301–1303 (2002).

[137] D. Khalil and A. Yehia, "Two dimensional multimode interference in integrated optical structures," J. Opt. A **6**, 137–145 (2004).

[138] K. Hassan, J.-C. Weeber, L. Markey, A. Dereux, A. Pitilakis, O. Tsilipakos, and E. E. Kriezis, "Thermo-optic plasmo-photonic mode interference switches based on dielectric loaded waveguides," Applied Physics Letters **99**, 241110 (2011).

[139] B. G. Lee, A. V. Rylyakov, W. M. J. Green, S. Assefa, C. W. Baks, R. Rimolo-Donadio, D. M. Kuchta, M. H. Khater, T. Barwicz, C. Reinholm, E. Kiewra, S. M. Shank, C. L. Schow, and Y. A. Vlasov, "Monolithic Silicon Integration of Scaled Photonic Switch Fabrics, CMOS Logic, and Device Driver Circuits," Journal of Lightwave Technology **32**, 743-751 (2014).

[140] R. F. Pierret, "Semiconductor Device Fundamentals," Addison-Wesley (1996).

[141] R. A. Soref, and B. R. Bennett, "Electrooptical Effects in Silicon," IEEE Journal of Quantum Electronics **QE-23**, 123-129 (1987).

[142] E. D. Palik, "Handbook of Optical Constants of Solids," Elsevier Science & Tech (1985).

[143] I. H. Malitson, "Interspecimen Comparison of the Refractive Index of Fused Silica," J. Opt. Soc. Am. **55**, 1205-1208 (1965).

[144] C. M. Sorace, "Advanced Silicon Photonic Modulators," Master Thesis, MIT (2010).